

**Properties of the Back Contact Interface for
Non-Vacuum Deposited Precursor-Based
Cu(In,Ga)Se₂ Solar Cells**

**zur Erlangung des akademischen Grades
eines DOKTORS DER NATURWISSENSCHAFTEN (Dr. rer. nat.)
von der KIT-Fakultät für Physik des
KARLSRUHER INSTITUTES FÜR TECHNOLOGIE
angenommene
DISSERTATION**

von

Dipl.-Phys. MSc. ANNEGRET VERONIKA HAUG

geboren am 29.05.1981 in Stuttgart, Deutschland

| | |
|------------------------------------|---------------------------------|
| Referent: | Prof. Dr. H. KALT |
| Korreferent: | Prof. Dr.-Ing M. POWALLA |
| Tag der mündlichen Prüfung: | 28.04.2017 |

**ZENTRUM FÜR SONNENENERGIE- UND WASSERSTOFF-FORSCHUNG
BADEN-WÜRTTEMBERG (ZSW)
STUTTGART, 2017**

“The chasm is far too wide, I never thought I’d reach the other side, but your love never fails.”

Chris McClarney

Contents

| | | |
|----------|---|-----------|
| 1 | Introduction | 7 |
| 2 | Fundamentals of CIGS Solar Cells | 11 |
| 2.1 | Basic Principles of Solar Cells | 11 |
| 2.1.1 | Photovoltaic Effect | 11 |
| 2.1.2 | p-n Junction | 12 |
| 2.1.3 | Diode Characteristics | 13 |
| 2.2 | Loss Mechanisms | 17 |
| 2.2.1 | Optical Losses | 17 |
| 2.2.2 | Recombination | 18 |
| 2.2.3 | Electrical Losses | 19 |
| 2.3 | Chalcopyrite Material System | 19 |
| 2.3.1 | Crystal Structure | 19 |
| 2.3.2 | Grain Boundaries | 21 |
| 2.4 | CIGS Solar Cell Structure | 23 |
| 2.4.1 | Basic Configuration | 23 |
| 2.4.2 | Interfaces | 25 |
| 2.5 | Preparation of CIGS absorber layers | 26 |
| 2.5.1 | Conventional Deposition | 26 |
| 2.5.2 | Non-Vacuum Processing | 29 |
| 3 | Experimental Details: Analysis & Preparation | 35 |
| 3.1 | Methods of Analysis | 35 |
| 3.1.1 | Chemical Composition | 36 |
| 3.1.2 | Layer Texture | 37 |
| 3.1.3 | Crystal Parameters | 38 |
| 3.1.4 | Optoelectronic Characterisation | 39 |
| 3.2 | Precursor Preparation | 40 |
| 3.2.1 | Metal Salts with Binder Material | 40 |

| | | |
|----------|---|-----------|
| 3.2.2 | Nanoparticles | 45 |
| 3.2.3 | Sputtered Alloy | 48 |
| 4 | Selenisation of Precursors | 53 |
| 4.1 | Overview | 53 |
| 4.1.1 | Specific Selenisation Tasks | 55 |
| 4.2 | Selenisation Details | 55 |
| 4.2.1 | Selenisation Set-Up | 55 |
| 4.2.2 | Influencing Factors | 58 |
| 4.2.3 | Standard Parameters for Influencing Factors | 59 |
| 4.2.4 | Reference Selenisation (HV) | 59 |
| 4.3 | Metal Salts with Binder Material — Doctor Bladed | 60 |
| 4.3.1 | Gallium-free Precursor Layers | 62 |
| 4.3.2 | Composition Change During Selenisation | 62 |
| 4.3.3 | Selenium Partial Pressure at Start of Crystallisation | 62 |
| 4.3.4 | Efficiencies | 64 |
| 4.4 | Nanoparticles — Doctor Bladed | 64 |
| 4.4.1 | Selenium Partial Pressure at Start of Crystallisation | 64 |
| 4.4.2 | Reduction Prior to Selenisation | 66 |
| 4.5 | Vacuum-Based Reference Process — Sputtered | 68 |
| 4.5.1 | Selenium Partial Pressure at Start of Crystallisation | 68 |
| 4.5.2 | Influence of Selenisation Duration | 68 |
| 4.5.3 | Efficiencies | 70 |
| 4.6 | Conclusion | 73 |
| 5 | Molybdenum Diselenide Formation | 77 |
| 5.1 | Overview | 77 |
| 5.1.1 | Studied Parameters for Molybdenum Selenide Formation | 78 |
| 5.1.2 | General Remarks about Formation Experiment | 79 |
| 5.2 | Impact of Molybdenum Characteristics | 79 |
| 5.2.1 | Morphology | 81 |
| 5.2.2 | Chemical Composition | 81 |
| 5.3 | Impact of Selenisation | 83 |
| 5.3.1 | Selenium Partial Pressure | 83 |
| 5.3.2 | Substrate Temperature | 84 |
| 5.4 | Summary | 86 |

| | | |
|----------|---|------------|
| 6 | Back Contact Interface — Mo/CIGS | 87 |
| 6.1 | Overview | 87 |
| 6.1.1 | Studied Parameters for Molybdenum Selenide Formation | 87 |
| 6.2 | Influence of Precursor | 88 |
| 6.2.1 | Sputtered Precursors | 88 |
| 6.2.2 | Metal Salt Precursors | 90 |
| 6.3 | Influence Selenisation Parameters | 90 |
| 6.3.1 | Selenisation Pressure | 90 |
| 6.3.2 | Selenisation Temperature | 93 |
| 6.4 | Summary | 95 |
| 7 | Interface with Additional Carbon Layer | 97 |
| 7.1 | Introduction | 97 |
| 7.1.1 | Motivation | 97 |
| 7.1.2 | Reference Samples | 98 |
| 7.1.3 | Analysis of Carbon Layer | 102 |
| 7.2 | Series Resistances – Carbon Layer Thickness Variation | 104 |
| 7.3 | CIGS Layer Thickness Variation | 108 |
| 7.4 | Discussion | 113 |
| 7.5 | Simulations | 114 |
| 8 | Summary and Outlook | 117 |
| 8.1 | Summary | 117 |
| 8.2 | Outlook | 119 |
| A | SCAPS Input Parameter | 121 |
| | Symbols and Abbreviations | 127 |
| | Bibliography | 133 |
| | Publications | 165 |
| | Acknowledgements | 169 |
| | Curriculum Vitae | 171 |

Chapter 1

Introduction

Since fossil energy resources on earth are highly limited they will not meet energy demands in the future. Therefore mankind is in urgent need of a sustainable energy supply. The solar power irradiated onto the earth's surface in one hour is more than enough to provide for the present total energy consumption on earth in one year [1]. So it is obvious that this overabundant energy resource should be used. As the direct conversion from solar energy to electricity photovoltaics is a method of choice avoiding unnecessary energy transformation with its inherent energy loss.

For a long time photovoltaics has had the image of an overpriced technology which would not be able to provide a reasonable share of the total energy demand on earth. By now substantial cost reductions for module fabrication could be achieved. As a result already a reasonable share of the German electricity is provided by photovoltaics. Further cost reductions are expected with thin film photovoltaics.

These thin film solar cells are a good candidate for cost efficient modules as less material is required and its quality can be much lower compared to silicon solar cells which have dominated the market for the last decades. Due to the low thickness of the absorber layers thin film solar cells can easily be used with flexible substrates to form flexible solar modules or they can even be produced with a roll-to-roll process.

Chalcopyrite absorber layers show the highest efficiencies of all thin film technologies [2–4] and have already been employed in commercially available photovoltaic modules [5–10]. All of the commercially available modules rely on vacuum-based technology. However vacuum-free methods require less expensive equipment and material leading to a great cost reduction for the production process and therefore have aroused interest and still do so [11–13]. They are usually two-stage processes consisting of a precursor step and an annealing step at an elevated temperature during which the crystal formation takes place.

Non-vacuum techniques with printed precursors are particularly suitable for mass production. They offer several advantages: As nearly all material used during the film formation is built into the layer the *material costs* are in general *lower* than for most vacuum based processes where a lot of material is lost on the endwalls of the deposition equipment. Also the *energy consumption* is *lower* during the production because high-vacuum pumps are not required and the selenisation step can be performed in much shorter time with less energy [14]. No vacuum chambers, pumps and other high vacuum equipment are needed. Thus *lower capital cost of the equipment* is expected which is an advantage especially for entering the business [15, 16]. A much *higher* possible *throughput* is expected. For roll-to-roll configurations deposition rates of several hundred meters per minute can be reached (reviewed for example for polymer based solar cells by Krebs [17]). Generally speaking printing processes are *simple processes* with which industry has a lot of experience and thus the process development is expected to be less challenging.

Even though a lot of work has been done to develop such vacuum-free processes the scientific foundation for these methods is rather thin. Most research within the CIGS community is done with absorbers and solar cells fabricated by vacuum based processes. Yet depending on the chosen fabrication method different peculiarities occur in absorbers fabricated in non-vacuum processes and also in the corresponding interfaces. Sometimes for example the fabrication process requires additional components for the film formation. These additives can have different influences on the solar cell properties.

In this work a simple printing technique (doctor blading) is used for the precursor preparation. Different inks are employed for printing: An ink system based on metal salts, originally developed at the ETH in Zürich [18] is applied. For a nanoparticle based precursor a completely new ink system is developed [19]. Beside the printing technique, a non-vacuum selenisation step had to be developed for the fabrication of solar cells. The focus in this work is on the interface between the back contact and the chalcopyrite absorber fabricated with non-vacuum methods. To investigate the difference also vacuum based processes have been developed and used as a comparison.

The thesis is subdivided into the following chapters:

In chapter 2 the fundamentals of $\text{Cu}(\text{In,Ga})\text{Se}_2$ (CIGS) solar cells are described. First the basic principles of solar cells are illustrated (2.1) and typical loss mechanisms in a solar cell are explained (2.2). Then chalcopyrite solar cells are described in detail: After an introduction of the material (2.3) the structure of a typical solar cell is presented (2.4) and the most common fabrication techniques are described (2.5).

Chapter 3 shows the employed characterisation techniques (3.1) and the deployed precursor deposition methods (3.2).

The main part of the experimental work and its results is organised by topic and divided into the following chapters: In chapter 4 the non-vacuum selenisation and its most important results are shown for all deployed precursor deposition methods. The MoSe_2 formation during this selenisation is studied in chapter 5, the properties of this interface layer in a realistic configuration in chapter 6, and finally in chapter 7 the influence of an additional carbon layer between back contact and absorber layer on the solar cell properties is investigated and discussed. In the last chapter of this thesis the results are summarised and an outlook is given.

Chapter 2

Fundamentals of CIGS Solar Cells

In the following chapter the basic principles of solar cells are described briefly (section 2.1) and various loss mechanisms are discussed (section 2.2). Subsequently the chalcopyrite material system is introduced (section 2.3) and the typical structure for chalcopyrite solar cells used in this thesis is presented (section 2.4). Finally different production methods are outlined (section 2.5).

2.1 Basic Principles of Solar Cells

A solar cell is an opto-electronic device which directly converts solar energy into electric energy via the photovoltaic effect (2.1.1). In an absorber layer the incident photon is absorbed and an electron–hole pair is generated. This pair is usually separated at a p-n junction (2.1.2). Via contacts the resulting current can be drained off the cell and used in an external load. To characterise solar cells in general and describe their performance, opto-electronic parameters are measured. These parameters are introduced in the last part of this section (2.1.3).

2.1.1 Photovoltaic Effect

As outlined above, in a solar cell the incident solar energy is converted into electric power. The first step of this conversion is the absorption of a photon and the generation of an electron–hole pair. The effect behind it is the photoelectric effect, which was first discovered by Henry Becquerel in 1839 [20].

In general the light absorbing layer is a semiconducting material. In semiconductors electrons fill the valence band up to its edge at the energy E_V . The valence band is separated from the next higher band, the conduction band starting at energy E_C , by a band gap with energy E_g . Hence charge transfer can only happen if electrons from the valence band are excited to the conduction band, for example by the absorption of a photon with an energy E_{ph} greater than or

equal to E_g :

$$E_{\text{ph}} = h\nu \geq E_g \quad (2.1)$$

where h is Planck's constant and ν the photon's frequency. Via relaxation possible excessive energy is released into the material as heat. After the excitation of an electron to the conduction band a hole remains in the valence band, an electron–hole pair is created.

In order to use the energy of an excited electron, the so generated electron–hole pair has to be separated. In most solar cell types this takes place at a p-n junction.

2.1.2 p-n Junction

A p-n junction is built by the combination of a p-type and an n-type semiconductor material and is the core of diodes like solar cells. It was first described by Shockley [21], Bardeen, and Brattain [22] who received the Nobel price for their research on semiconductors in 1956. A p-type semiconductor has a Fermi level (E_F) close to the valence band, holes are majority and electrons minority charge carriers (see fig. 2.1a). In contrast the Fermi level in an n-type material is close to the conduction band and electrons are the majority and holes the minority charge carriers (see fig. 2.1b).

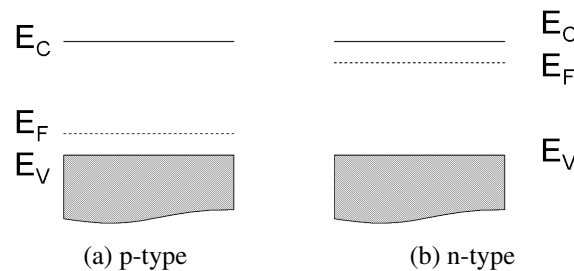


Figure 2.1: Band Diagrams of p- and n-type Semiconductors.

The Fermi levels with respect to the valence and conduction bands are shown both for a p-type (a) and for an n-type (b) semiconductor material.

When connecting the materials the concentration difference causes diffusion of the charge carriers. Holes from the p-type material diffuse to the n-type and electrons from the n-type diffuse to the p-type material. This diffusion current leads to the formation of a space charge region and a potential difference between the p and n side which gives rise to an electric field \vec{E} (see fig. 2.2). This resulting field causes a drift current in the opposite direction as the diffusion current (see fig. 2.3). Once the magnitude of these currents is the same, the p-n junction is in equilibrium and can be characterised by its built-in voltage V_{bi} .

Electron–hole pairs generated by the incident light are separated by the built-in electric field, with the electrons drifting to the n-type material and the holes to the p-type material. This leads

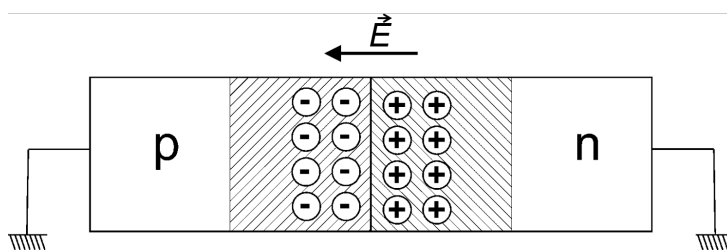


Figure 2.2: Electric Field at the p-n Junction.

The diffusion current causes the formation of the space charge region. The difference in potential leads to an electric field.

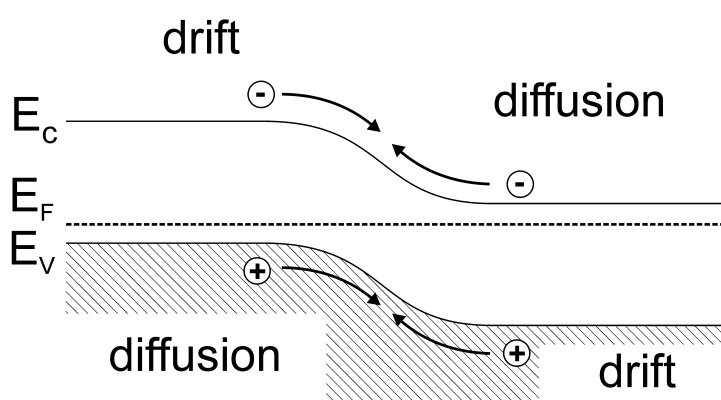


Figure 2.3: p-n Junction in General.

After bringing p- and n-type semiconductor material into contact the p-n junction is formed. Once the diffusion and the drift current are equally strong the junction is in equilibrium. A band diagram for CIGS with a heterojunction can be seen in fig. 2.9.

to a light induced direct current, the so-called photo current J_{ph} as soon as the circuit is closed (see section 2.1.3).

2.1.3 Diode Characteristics

Solar cells are a special diode configuration. Hence, to understand the electric behaviour we have to look at the diode characteristics. First the $I-V$ characteristics are deduced and later fundamental parameters for solar cells are introduced.

I-V Characteristics

For the calculation of *I-V* characteristics the so called Shockley equations are relevant: Poisson's equation (eq. 2.2), current density equations (eq. 2.3 and 2.4) and continuity equations (eq. 2.5 and 2.6). These are the basic equations for all kinds of diodes.

Poisson's equation (2.2) is derived from Gauss' law, the first of Maxwell's equations ([23, 24]. Here the relation between the spatial variation of the electric field \vec{E} and the charge carrier density, which consists both of hole (*p*) and electron (*n*) density and of the ionised donor (N_D^+) and acceptor (N_A^-) atoms, is shown:

$$\frac{\partial}{\partial x} (\epsilon_0 \epsilon_r \vec{E}) = -q (p - n + N_D^+ - N_A^-) \quad (2.2)$$

where ϵ_0 is the vacuum permittivity, ϵ_r the relative permittivity and *q* the elementary charge. Secondly the electron and hole current densities (j_n and j_p) are defined. In a 1D model with *x* the direction perpendicular to the absorber plane they consist of a drift (with mobilities μ_n and μ_p) and a diffusion term (with diffusion constants D_n and D_p).

$$j_n = q \left(\mu_n n E + D_n \frac{\partial n}{\partial x} \right) \quad (2.3)$$

$$j_p = q \left(\mu_p p E - D_p \frac{\partial p}{\partial x} \right) \quad (2.4)$$

Furthermore the continuity equations are needed. They relate the spatial variation of the current densities to the difference of generation and recombination rate (*G* and *R*).

$$\frac{\partial j_n}{\partial x} = q (R - G) \quad (2.5)$$

$$\frac{\partial j_p}{\partial x} = -q (R - G) \quad (2.6)$$

Inserting equations 2.3 and 2.4 into 2.5 and 2.6 leads to a coupled set of differential equations, the so-called transport equations:

$$D_n \frac{\partial^2 n}{\partial x^2} + \mu_n E \frac{\partial n}{\partial x} + n \mu_n \frac{\partial E}{\partial x} - R + G = 0 \quad (2.7)$$

$$D_p \frac{\partial^2 p}{\partial x^2} - \mu_p E \frac{\partial p}{\partial x} - p \mu_p \frac{\partial E}{\partial x} - R + G = 0 \quad (2.8)$$

These equations can not be solved analytically in general. Yet with some simplifying assumptions an ideal diode equation can be derived:

$$J(V) = J_s \left(e^{qV/k_B T} - 1 \right) \quad (2.9)$$

J_s is the saturation current, k_B Boltzmann's constant and T the temperature. The equation itself describes the ideal diode. For a real solar cell other parameters have to be taken into account. In the single diode model (see fig. 2.4) a parallel and a series resistance (R_p and R_s) are included. Various electric losses inherent in real devices are represented by these resistances: shunts and defects in the material causing leakage currents are represented by R_p and contact resistances by R_s . Thus R_p should be as high and R_s as low as possible. The current generation is mapped by a current source parallel to the diode. With this the diode equation becomes:

$$J(V) = J_s \left(e^{q(V - JR_s)/Ak_B T} - 1 \right) + \frac{V - JR_s}{R_p} - J_{ph} \quad (2.10)$$

where J_{ph} is the photo current and A is the ideality factor. This is a material specific correction factor which is 1 for the ideal diode. For $I-V$ characteristics dominated by trap-assisted recombination (see chapter 2.2.2) it is equal to 2. In general it is between 1 and 2 for real devices [25]. Yet ideality factors higher than 2 can indicate for example tunneling enhanced recombination [26], surface defect states or other parasitic effects [27].

In fig. 2.5 the resulting $I-V$ characteristics with the fundamental parameters can be seen. These parameters are explained in the following section.

As one can see, the curve in the illuminated case is roughly the same as in the dark case, just shifted by the photo current. This fact is called the principle of superposition. However, in most chalcopyrite solar cells this principle does not hold rigorously in general. Voltage-dependent photo currents or resistances can cause a cross-over [28]. A conduction band off-set between absorber and buffer layer acting as a secondary barrier can cause failing of the superposition [29] as well.

Fundamental Parameters of Solar Cells

To describe the opto-electronic properties of solar cells mainly four fundamental parameters are used: the short circuit current J_{sc} , the open circuit voltage V_{oc} , the power conversion efficiency η , and the fill factor FF . These parameters are introduced in the following paragraphs.

The *short circuit current* J_{sc} is the current that flows when the contacts of the solar cell are connected with a perfect conductor. In most cases it is equal to J_{ph} . It is determined mainly by optical properties. For example incomplete absorption causes losses for the short circuit current (see chapter 2.2.1). Most often the current density is used for the description of solar cells (j_{sc}) to allow comparisons regardless of the active area of the solar cell.

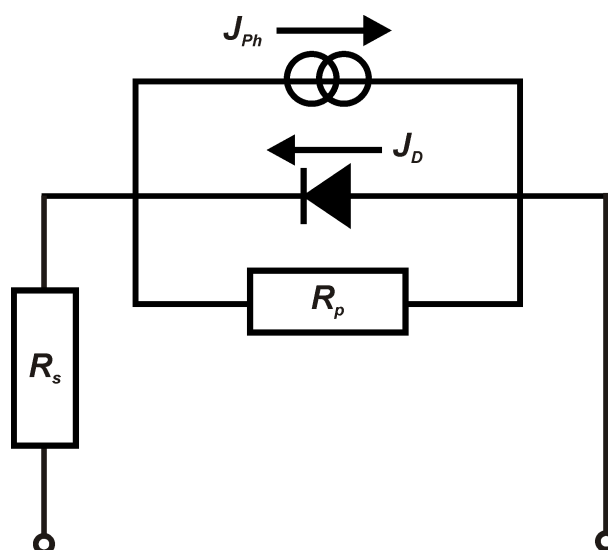


Figure 2.4: Single Diode Model.

Solar cells can be described by the single diode model incorporating parallel and series resistances, a current source with photo current J_{ph} and the diode itself with diode current J_D .

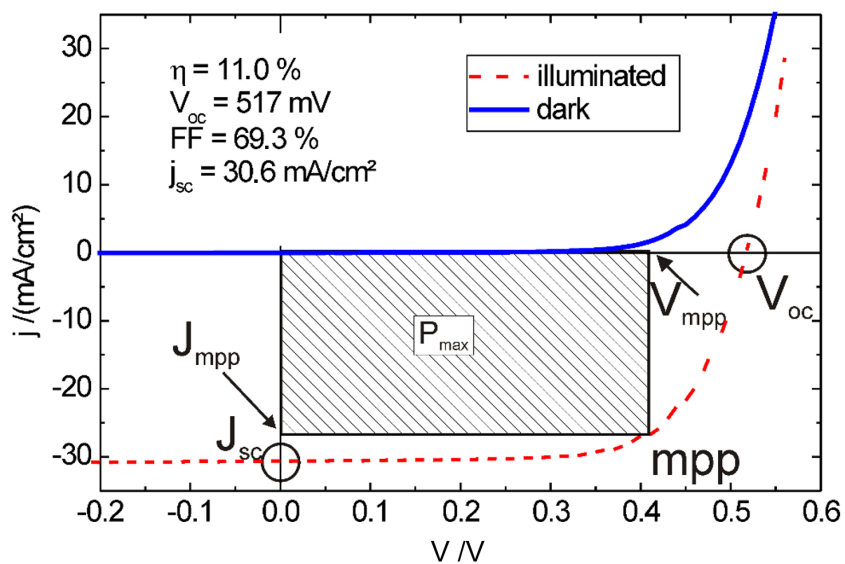


Figure 2.5: I - V Characteristics of a Typical Solar Cell.

The straight blue line shows the behaviour in the dark whereas the red dashed line gives it under illumination. Characteristic parameters like V_{oc} , J_{sc} , and P_{max} can be seen. The maximum power point is denoted by mpp.

The *open circuit voltage* V_{oc} is the voltage across an unloaded (open) solar cell. It is equal to the separation between the Fermi levels of the back and the front contact. The theoretical limit for the separation of the Fermi levels is the band gap of the material. Yet various recombination processes will lower V_{oc} (see chapter 2.2.2).

The *power conversion efficiency* η is one of the most important parameters when rating solar cells. It is defined as the ratio of the maximum electric output energy P_{max} and incident light energy P_{in} :

$$\eta := \frac{P_{max}}{P_{in}} = \frac{V_{mpp} \cdot J_{mpp}}{P_{in}} \quad (2.11)$$

The power of a generator is the product of its voltage and its current. So the power is zero if either the voltage or the current is zero. The optimal working point is somewhere in between. It is called maximum power point (mpp). Thus P_{max} can be written as a product of the voltage V_{mpp} and the current density J_{mpp} at this maximum power point.

The *fill factor* FF is given by

$$FF := \frac{V_{mpp} \cdot J_{mpp}}{V_{oc} \cdot J_{sc}} \quad (2.12)$$

and is a measure for the squareness of the I - V characteristics. High series resistances and low parallel resistances reduce the fill factor and thus the efficiency of a solar cell.

With all this the power conversion efficiency can be calculated by

$$\eta = \frac{V_{oc} \cdot J_{sc} \cdot FF}{P_{in}} \quad (2.13)$$

Each of the parameters can decrease due to losses and thus lower the overall efficiency.

2.2 Loss Mechanisms

In the next section possible loss mechanisms are discussed, which can lower one or more of the factors determining the efficiency of a solar cell. Loss mechanisms can be roughly divided into optical, recombinatorial, and electrical losses.

2.2.1 Optical Losses

Optical losses mainly reduce the photo current generated by the solar cell. Depending on the design of the solar cell different effects are dominant, but they exist in all solar cell types.

Before entering the solar cell light can be blocked or reflected (*shading and reflexion*). Possible grid fingers block some of the sun light and at the front contact some of the light is reflected (the layer composition is described in chapter 2.4). Within the front window short-wave

light can already be absorbed before entering the absorber itself (*absorption within the window layer*).

Even if a photon enters the absorber it is not ensured that it is absorbed. As already mentioned (see eq. 2.1), a photon with an energy less than the band gap cannot be absorbed, it traverses the absorber and cannot contribute to the photo current (*absorption and transmission*). If the energy is higher than the band gap the excessive energy is thermalised and thus lost. Moreover material properties determine the absorption characteristics of an absorber. Hence different thicknesses are needed for different materials.

2.2.2 Recombination

Once an electron–hole pair is generated recombination can take place. Instead of being separated and adding to the generated current the pair recombines — the electron from the valence band fills the hole in the conduction band. There are different ways for this to happen. The most fundamental one is *radiative recombination* with a direct transition of the electron from the conduction to the valence band with the emission of a photon — the inverse process to absorption. Even in an ideal semiconductor this can not be prevented.

In addition, there are non-radiative recombination paths. One of them is *Auger recombination* [30]. Again, the electron transitions directly from the conduction to the valence band. Though for Auger recombination the energy of the electron is transferred to another carrier and subsequently lost through thermal relaxation. Thus the generated electron–hole pair only produces heat and no current.

In real semiconductors, especially in those with indirect band gaps, recombination via traps is the predominant recombination process. It is called *Shockley-Read-Hall (SRH) recombination* [31, 32]. Here the capture of an electron from the conduction and a hole from the valence band is facilitated by the trap. Traps with energies roughly in the middle of the band gap are most important for this process, where the recombination energy is released in small portions as phonons into the lattice. If the trap energy is close to the valence band the trap states are occupied by electrons. Captured holes are released back to the valence band before an electron from the conduction band can be captured and recombine with the trapped hole. For trap energies close to the conduction band the situation is reversed. The states are empty and trapped electrons are re-emitted to the conduction band before a hole can be captured.

As real semiconductors do not extend infinitely, surfaces and interfaces occur. They typically contain a large number of electrically active states because abrupt termination of the crystal leads to a large number of recombination centers [33]. The recombination mechanism is comparable to the trap-assisted recombination. However, traps at the surfaces are not discrete single states but rather a whole set of nearly continuously distributed states. Furthermore impurities accumulate at surfaces and interfaces, which causes additional trap-assisted SRH re-

combination. For this *surface or interface recombination* the surface recombination velocity is the crucial parameter. It is characteristic for the surface or interface quality and can usually be approximated by infinity for semiconductor-metal interfaces.

All recombinatorial losses mainly reduce the open circuit voltage V_{oc} . Thus for achieving high voltages the recombination centers have to be minimised. Often these losses are incorporated into the circuit model by a second diode parallel to the first. The resulting model is therefore called the 2-diode-model and is often used for silicon based thin film solar cells and sometimes also for chalcopyrite solar cells (for example [34–36]).

2.2.3 Electrical Losses

When the contacts are not perfectly ohmic or the feed lines are non-ideal conductors, in general when there is an additional resistance, electrical losses are the consequence. They can be summarised with the already introduced *series resistance* R_s (see 2.1.3).

In case the absorber is not perfectly dense or has other defects, shunts and parasitic current paths can pervade the absorber layer. The resulting electrical losses are subsumed under a *parallel resistance* R_p (see 2.1.3).

Series resistances can be roughly deduced from the slope of the I – V characteristics crossing the ordinate. Parallel resistances can be derived from the slope of the I – V characteristics crossing the x-axis. With this it becomes clear that all these ohmic losses reduce the fill factor FF significantly.

These losses occur in all types of solar cells, not only in chalcopyrite types, and have to be reduced for high efficiencies. In the following sections the focus will be on the chalcopyrite material and its properties to see how this can be achieved for this particular material system.

2.3 Chalcopyrite Material System

$\text{Cu}(\text{In,Ga})\text{Se}_2$ (CIGS) is a compound semiconductor with a direct band gap and a high absorption. Hence it is particularly suitable for the absorber layer of a solar cell. The crystal structure of CIGS is introduced in section 2.3.1. As the CIGS layer in a solar cell is in general polycrystalline, grain boundaries are an important issue. They are shortly discussed in section 2.3.2.

2.3.1 Crystal Structure

The chalcopyrite structure is very similar to the diamond structure. It can be derived from the diamond cubic crystal structure as shown in fig. 2.6. This configuration can be found in many group IV solids and is described in most solid state textbooks (e.g. [37] and [38]). Diamond, and

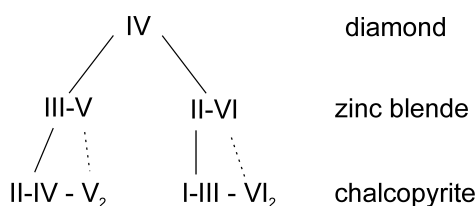


Figure 2.6: Derivation of Crystal Structure.

The principal configurations for the various compounds derived from the group IV configuration and the corresponding names are shown, sorted by element groups.

accordingly carbon, was merely the first solid (or atom type) where this structure was observed. It can be described as two face centered cubic (fcc) lattices, where one is shifted by a quarter of a body diagonal. Keeping the structure of the atoms, while alternating types of atoms, one gets the so called zinc blende structure. It is named after the mineral ZnS with this crystal configuration and alternating zinc (Zn) and sulfur (S) atoms.

For the chalcopyrite structure one type of atoms has to be replaced by two others [39]. This leads to a tetragonal unit cell which can be seen in fig. 2.7. For the original chalcopyrite, yellow copper ore (CuFeS_2), the zinc layers are replaced by copper (Cu) and iron (Fe) in turns. In CIGS these iron sites are taken by indium (In) and gallium (Ga) and the sulfur sites by selenium (Se).

For chalcopyrite solar cells the I-III- VI_2 configuration (right side in fig. 2.6) is most commonly used. Different alternatives of this compound are utilised. The group III atoms can be In, Ga, or Al (aluminum) or a combination thereof. The group VI atoms can be Se and S or both together. By varying the composition of the material the band gap of the material can be easily shifted from 1.04 eV for CuInSe_2 up to 2.7 eV for CuAlS_2 [40]. So the whole visible spectrum can be covered. In this work the compound composed of Cu, In, Ga, and Se is mostly employed. For some experiments only Cu, In, and Se are used.

The most important phase diagrams for this compound were published by Goedecke et al.[41–43]. It can be clearly seen that the compound has to be designed slightly copper poor in order to reach the desired stable alpha phase of CIGS. With a stoichiometric composition a conductive copper selenide phase will occur and lead to shunted cells. In general a copper content has to be slightly below 25 % While the stable phase is broader at higher temperatures it is quite narrow at room temperature. Thus it is assumed that the compound segregates into an alpha and beta phase where the beta phase (CuIn_3Se_5) is also known as ordered defect compound (ODC) [44]. By adding sodium or replacing a part of indium by gallium this existence window can also be broadened towards indium and gallium rich compositions [45]. The optimum content of gal-

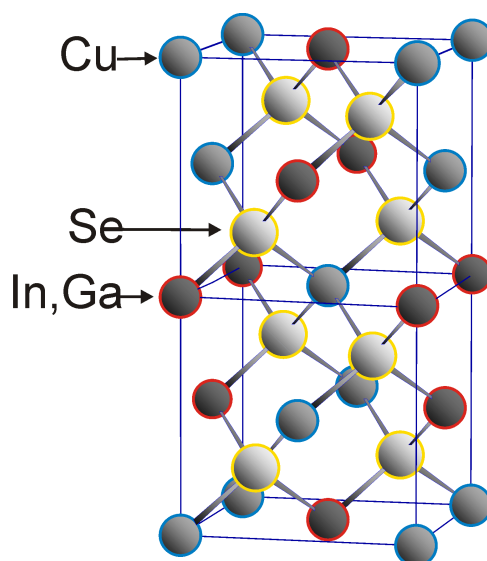


Figure 2.7: Chalcopyrite Structure.

A tetragonal unit cell of the chalcopyrite structure is shown with copper (blue), indium and gallium (red) and selenium (yellow) atoms.

lium differs along the depth of the absorber and also depends on the gradient within the layer. In general the overall content of gallium in the resulting layer is in the range of 5–10 %.

2.3.2 Grain Boundaries

Chalcopyrite absorber layers have typically a thickness of 1–2 μm consisting of small grains that often do not exceed 0.5–1 μm [46]. Hence grain boundaries play an important role in chalcopyrite solar cells and are assumed to have a much stronger effect than in multicrystalline silicon solar cells. Yet the maximum efficiencies of multicrystalline silicon and polycrystalline chalcopyrites are comparable and chalcopyrites even outperform multicrystalline silicon solar cells [47]. Thus the grain boundaries have to be quite inactive electronically. Indeed many polycrystalline chalcopyrites cells ([3, 48–50]) outperform even the best single crystal cells [51]. Hence sometimes even a positive effect of the grain boundaries is presumed. Understanding the physics behind grain boundaries in chalcopyrite materials is important for high efficiency solar cells. Up to now non-vacuum methods yield significantly lower efficiencies than cells fabricated with vacuum-based methods. Although the physics of grain boundaries is not the main topic of this work, it is important to have some basic knowledge on grain boundaries to understand some of the crucial issues related to chalcopyrites.

Both the electrical and the chemical structure of grain boundaries are not fully understood and still highly disputed ([46, 52, 53]). A lot of research is devoted to analyse and understand

it ([54–57]). Depending on the assumed structure different explanatory approaches for the behaviour of grain boundaries have been developed. Rau et al. identify four of them [58]: crystallography, intrinsic and extrinsic passivation, and band structure.

Crystallography An influential parameter for the number of electronic states at a grain boundary is the crystallographic orientation of the two involved grains relative to each other. If these two grains are mirror-inverted to each other the boundary between them is called a twin boundary [59, 60]. They do not have strained or dangling bonds and are the dominating type in chalcopyrite thin films [61, 62]. Indeed no charged defects can be seen for twin boundaries [63].

Intrinsic passivation Calculations of Yan et al. [64, 65] suggest an intrinsic passivation of grain boundaries. Due to extensive atomic relaxation, boundaries do not cause deep level defects, which usually form recombination centers in chalcopyrite structures, and are charge neutral. Therefore they exhibit no electrical potentials and are electrically benign [64].

Extrinsic passivation If grain boundaries initially have a high electronic activity, extrinsic passivation is necessary. Oxygenation of the boundaries might serve as a passivation: Assuming the boundaries are positively charged due to Se vacancies, they can be passivated by oxygen [66]. The effect might be increased by the presence of sodium [67, 68], although this theory is also disputed [69].

Band structure Changes in the band structure could account for the benignity of grain boundaries as well. A valence band offset acts as a barrier for the majority carrier and can be caused by a minor Cu deficiency of the contiguous region [53, 70]. Some experiments showed a Cu deficiency [71], others did not [54, 72]. The region has to have a certain thickness and homogeneity along the whole grain boundary. Yet if this is the case, grain boundaries not perpendicular to the collecting junction would block hole transport to the back contact [73]. So the valence band offset can not be the only reason for the low activity.

This short introduction already shows that this topic is a very interesting research area. It has been shown that quite high efficiencies can be achieved even without detailed understanding of the grain boundaries [58]. As soon as the non-vacuum production methods are sophisticated enough and the efficiencies rise sufficiently, research on grain boundaries becomes important for an even further increase in efficiency for CIGS solar cells fabricated with these methods.

2.4 CIGS Solar Cell Structure

For complete devices not only absorber layers are needed. The typical configuration of all layers in a solar cell is explained in chapter 2.4.1. The resulting interfaces are shortly described in chapter 2.4.2

2.4.1 Basic Configuration

Thin film solar cells can be grown in substrate and superstrate configuration [74]. For the substrate setup the back contact is deposited on to the glass substrate while for the superstrate design the front contact is on the glass and the light enters the cell from the glass side. For low-cost encapsulation the superstrate setup is more suitable [75] as one part of the encapsulation can be any low-cost material and does not need to be transparent. Yet for process-related reasons the substrate configuration is more commonly used: In general the transparent contact is temperature sensitive, thus it is easier to deposit it after the absorber formation where high temperatures are favourable. The substrate configuration is also used at ZSW and for this work.

The typical setup can be seen in figure 2.8, where materials and layer thicknesses of a standard ZSW process are indicated. CIGS solar cells in this thesis are deposited on a soda lime glass (SLG) covered with molybdenum (Mo). SLG is widely used, since its thermal expansion coefficient matches well with the coefficients for CIGS [76]. Studies with other back contact materials showed that Mo is one of the most suitable materials [77]. It is relatively stable at the temperatures used in the following production processes and has a low contact resistance to CIGS [78]. In this thesis it is sputtered in a bi-layer process and has a thickness of approximately 500 nm.

Then the absorber layer (Cu(In,Ga)Se_2 – CIGS) follows. As this layer is the most complex one, with quite some variations in its fabrication, a whole chapter (2.5) is devoted to its manufacturing.

Buffer and window layers are deposited on top of the absorber layer: In this thesis an approximately 60 nm thick cadmium sulfide (CdS) layer forms the n-type buffer. Alternative materials are for example indium sulfide and zinc sulfide (see chapter 2.4.2). There are various fabrication methods for this layer, yet here only chemical bath deposition (CBD) is used. A thin (≈ 50 nm) intrinsic zinc oxide (i-ZnO) layer follows and finally the front contact consisting of 1 μm aluminum doped zinc oxide (ZAO) is sputtered. Except for the absorber layer (see chapter 2.5) all layers are fabricated by the conventional methods according to ZSW standard processes. Therefore the thicknesses are usually the same for all tested cells.

The complete band structure of a typical solar cell can be seen in figure 2.9. In general the p-n junction separating the electron-hole pairs is close to the surface facing the light as the light intensity decreases exponentially. If the space charge region is equally expanded into

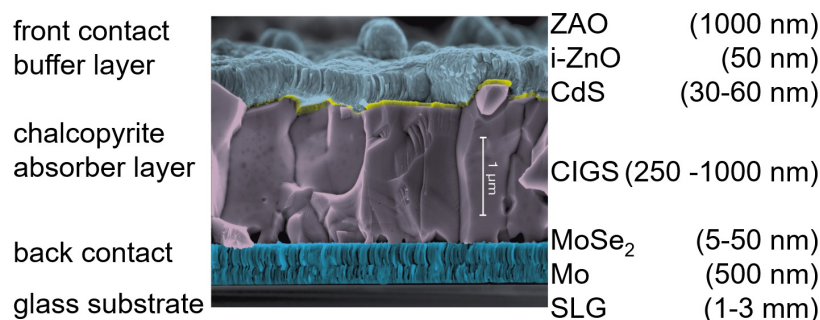


Figure 2.8: Typical Cell Configuration.

The typical CIGS solar cell is fabricated on a soda lime glass (SLG) covered with molybdenum (Mo). On top of the absorber layer (Cu(In,Ga)Se₂ – CIGS) buffer and window layers are deposited: Cadmium sulfide (CdS) forms the n-type buffer, an intrinsic zinc oxide (i-ZnO) layer follows and finally the front contact consisting of aluminum doped zinc oxide (ZAO) is sputtered.

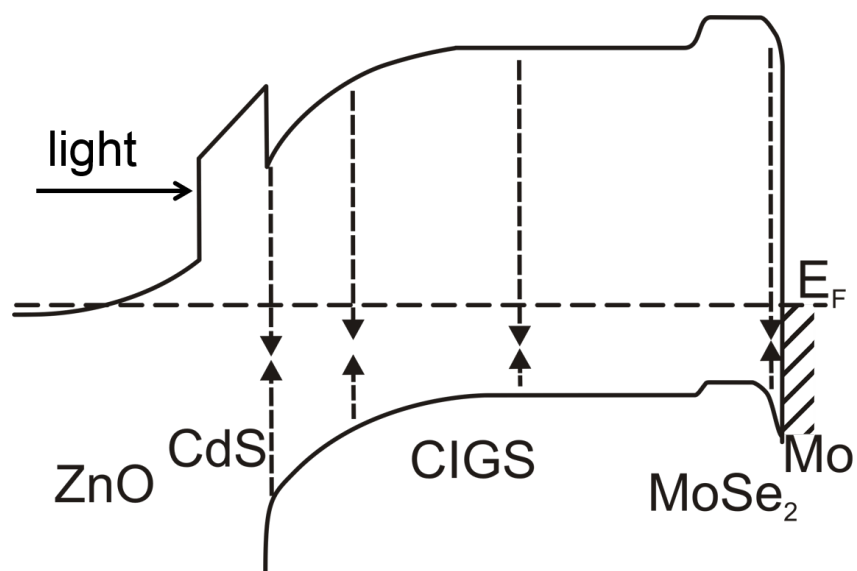


Figure 2.9: Band Diagram for Typical Cell Configuration According to [79].

The band diagram for a typical cell configuration is shown. The molybdenum selenide layer at the back contact interface is important for the ohmic contact.

absorber and buffer layer, open circuit voltage and fill factor can increase. Yet this gain can not compensate the loss in the photo current [80]. The electric field reaches far into the absorber layer so that created electron-hole pairs are separated. Close to the p-n junction the band gap is preferably higher than in the bulk of the absorber to render a possibly higher open circuit voltage. This higher band gap can be realised either with sulfur or gallium. At the back contact a back surface field is preferable to avoid recombination. Usually this is formed through a slightly higher gallium content towards the back contact. For an ohmic contact the molybdenum selenide layer is expedient. The interfaces are described in the following section.

2.4.2 Interfaces

Between all the described layers interfaces occur. The interfaces between the absorber and its adjacent layers are the most interesting ones and a lot of research is devoted to them:

The *buffer/absorber-interface*, in general CdS/CIGS, forms the p-n junction. Thus even at a very early stage it was already the subject of research and still is [68, 81–84]). In recent years much effort has been put into the development of various cadmium-free buffer layers [85–91], even organic buffers have been developed [87]. Such a buffer layer can eliminate some disadvantages related to the cadmium sulfide layer and offers additional advantages [86, and references therein]: The environmental risks related to cadmium in the production process can be reduced. In some countries the use of cadmium in electrical or electronic equipment is prohibited by legal regulations. To cadmium-free modules they are irrelevant. For the common vacuum-based methods technological problems are easily caused by a non-vacuum process in a vacuum line. For the non-vacuum processes covered here this is not relevant. Yet the chemical bath deposition which is usually used for cadmium sulfide involves high disposal costs which are preferably avoided. Additionally many cadmium-free buffer layers offer a potential increase of current generation in the blue region (350 nm to 500 nm), where CdS reduces the transmission of the window layer stack without contributing essentially to the photogeneration of carriers. Hence the cell efficiency can be increased. The resulting cadmium-free interfaces have been studied in detail [92–94]. Yet the world record efficiencies for cadmium-free solar cells are still slightly lower than for the conventional solar cell structures [95, 96].

The other absorber-related interface is the *back contact interface*, in general Mo/CIGS. Usually the molybdenum (Mo) back contact reacts with selenium (Se) to MoSe₂ either during film deposition or selenisation [97, 98]. Investigations with samples from a multi-stage process (see 2.5.1) show that MoSe₂ is primarily built at the beginning of the second stage under indium/gallium-rich conditions [99] as it does not form under copper-rich conditions. It prevents a further reaction between CIGS and molybdenum back contact [100].

MoSe₂ is a layered semiconductor with a band gap of 1.3 eV to 1.4 eV and p-type conductivity.

In early publications about this topic this additional layer was thought to deteriorate photovoltaic performance as MoSe_2 decreases the fill factor [101]. Often a Schottky-type barrier was assumed regarding the back contact between molybdenum and CIGS [102, 103]. But it was shown that a favourable ohmic contact forms at the interface with MoSe_2 instead of the Schottky-type contact formed without the selenide layer [104, 105]. Since then the electronic characteristics have often been a subject for research [105–110]. Due to its band gap, which is higher than the one of standard CIGS, it forms a back surface field for the photogenerated electrons and a low resistivity contact for the holes [111].

MoSe_2 is crystalline, thus its specific structure is relevant as well. It is layered and has a so called trigonal prism coordination geometry. It consists of triple layers (Se-Mo-Se) which are covalently bonded within and by weak van der Waals forces to each other [112, 113]. The orientation of these MoSe_2 -layers with respect to the substrate is found to be important for the adhesion of the absorber layer [98, 104]. If the layers are parallel to the substrate poor adhesion is a consequence. Perpendicular layers, in contrast, enhance the adhesion [105].

Another important characteristic of the back contact interface are the optical features. For absorber layers thinner than the typical absorption length of about $1\ \mu\text{m}$ for CIGS, light is transmitted to the back contact [114]. In order to avoid the loss of this light the back contact should be highly reflective. Light which is absorbed at the back contact is lost for energy conversion and lowers the overall efficiency. Yet the optical characteristics of a standard molybdenum back contact are deteriorated by the thin layer of MoSe_2 since the combination of molybdenum and molybdenum selenide arrange for a non-reflecting black back contact [115].

For non-vacuum fabrication methods so far only little research has been conducted into this interface and its characteristics [107]. A step to close this gap is taken in this thesis.

2.5 Preparation of CIGS absorber layers

The preparation of the CIGS absorber layer is the most sophisticated process in the manufacturing of CIGS solar cells. Thus it is most challenging to develop vacuum-free methods for it. Therefore we concentrate on the vacuum-free fabrication of CIGS and neglect all other layers. In the following chapter the various deposition methods are described – both conventional vacuum-based (2.5.1) and alternative vacuum-free (2.5.2). An overview can be seen in figure 2.10. The methods used in this thesis and the corresponding typical parameters are dealt with in detail in chapter 3.2.

2.5.1 Conventional Deposition

Customary fabrication of CIGS is vacuum-based. It can be divided into two main methods: co-evaporation and sequential processing. While the former builds the absorber in one deposition

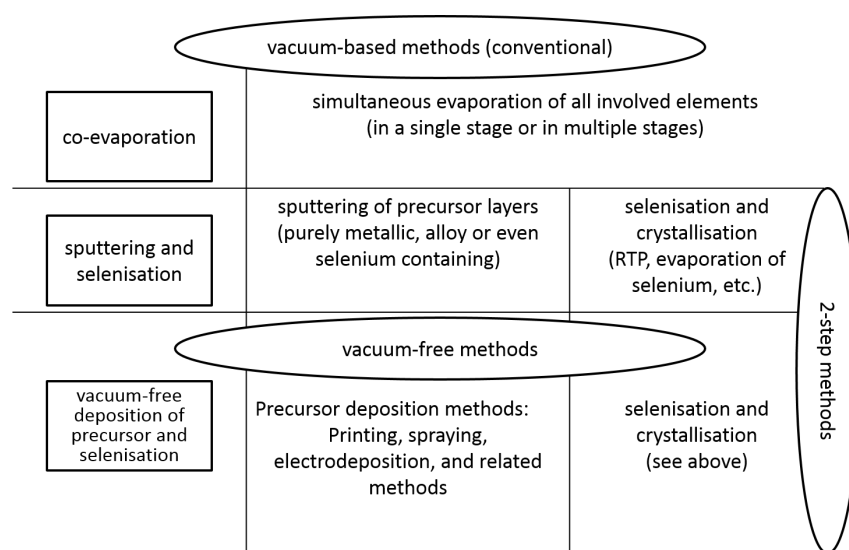


Figure 2.10: Overview of Fabrication Methods.

In this figure the various fabrication methods are displayed — both conventional and vacuum-free methods. While conventional processes can build the absorber in one single step (co-evaporation) or in a two-step process, all non-vacuum methods use two steps to form the chalcopyrite material.

step, the later uses precursor layers which are converted into the chalcopyrite material in a second step.

Co-Evaporation

For co-evaporation all elements are evaporated from elemental sources. In general there is an excess of selenium vapour present during the whole process. Highly efficient CIGS-solar cells are deposited in various stages with different temperatures and metal flux ratios, each with the mentioned Se excess. The ratio between Se and the other elements has an effect on morphology, orientation, and grain size [116].

Co-evaporation is the most successful method for the deposition of a CIGS-absorber layer. For small areas it offers the best control of composition and compositional grading [12]. Thus world record efficiencies in recent years were mostly fabricated with it [2, 3, 48–50, 117–119]. These and most other high-efficiency solar cells on laboratory scale ([120, 121]) have been fabricated by a so called multi-stage process, which was first presented by Gabor et al. [122] as a three-stage process: In the first step indium and gallium are deposited in a selenium atmosphere at a lower temperature (depending on the specific process between 250 °C and 450 °C). During the second step mainly copper is evaporated in an selenium atmosphere, usually at an elevated temperature of approximately 550 °C to 600 °C and more. For low temperature processes it is

beneficial to offer gallium additionally during this second phase [49]. In the last step once again indium and gallium are evaporated in a selenium atmosphere. The temperature remains high for this step. During cool-down of the substrates a selenium atmosphere is still present in the chamber to avoid selenium depletion of the surface.

Co-evaporation was developed from a two stage process where a copper rich CIGS layer was fabricated at a lower substrate temperature (450 °C) and then an indium rich layer was deposited on top at a higher substrate temperature (550 °C) [123–125].

In industrial implementations of co-evaporation it is highly challenging to retain uniform chemical composition during the up-scaling of the co-evaporation method. At ZSW a lot of research and development has been conducted on this topic and several years ago the method could be transferred to industrial production [126]. Nowadays it is used for example by MANZ AG (former Würth Solar, ZSW technology) [121, 127] and Global Solar [9].

Sequential Process

Whereas the co-evaporation process involves challenges for scaling-up production processes most sequential processes avoid a lot of these problems. There are two well established methods which generally consist of two steps:

In the first step a precursor layer (either chalcogen-containing or not) is deposited at lower temperatures usually by sputtering [128–132] or thermal evaporation [133–135]. Simple techniques use only one or two different layers but more complicated approaches build up a multi-layer system which leads to smoother surfaces and better crystallinity [134].

The second step involves a thermal treatment either in chalcogen-containing atmosphere or — if the precursor already contains an excess of chalcogen — sometimes even without. If a selenisation during the second step is needed, there are different possibilities. The most efficient way is to use H₂Se which is often diluted in argon gas [128, 135]. However H₂Se is highly toxic and a lot of research is focused on avoiding its use for the selenisation of precursor layers. Elemental selenium vapour for example is quite common [129, 131, 134, 136–139] even though various studies showed that under comparable conditions (time, temperature etc.) H₂Se is more efficient and leads to a higher quality of the CIGS film [135, 140]. Furthermore a few studies showed the suitability of diethylselenide as a selenisation agent [141]. More details on the selenisation process will be presented in chapter 4.

If the precursor layers contain an excess of selenium a simple thermal treatment is sufficient for the chalcopyrite formation. Rapid thermal annealing (RTA) is a fast technique for the crystallisation of precursor layers [142–145]. An important characteristic of this annealing step is its high heating rate. It is necessary to avoid dewetting of the selenium layer on top of the precursor stack. This happens for low heating rates and is known to be detrimental for the formation of the chalcopyrite [143].

In contrast to the co-evaporation process it is quite challenging to get the desired band gap grading by a gallium content variation with sequential processes. As long as the selenium is incorporated into the absorber from the top it is impossible [146, 147]. For most sequential processes this is the case, though a post sulfurisation step can help to establish a desired band gap grading [148, 149]. As it passivates the CIGS surface it additionally serves to improve device efficiencies conveniently [150].

A big advantage of sequential processes is the fact that it is easier to achieve a uniform composition over a large area by means of established processes like sputtering used in glass industry. This is one of the reasons that for a long time most of the highest module efficiencies have been achieved with this technique [14, 151–153]. Even the current listed world record of 17.8 % is made with sequential processes [154]. Because it is easier to scale up this method, it is particularly suitable for mass production. It is used for example by AVANCIS, formerly Shell Solar [153], and Solar Frontier [154], previously Showa Shell [151]. However, the second step, the selenisation seems to be the challenging part for fast large area processing.

2.5.2 Non-Vacuum Processing

In the following section a short introduction to various non-vacuum methods is given. It comprises both a description of the techniques and an overview which groups or companies work with these methods and what has been achieved. A focus is set on particle- and solution-based techniques whereas electrochemical ones are only referred to briefly as they are not used in this thesis.

Electrochemical Techniques

Since 1983 electrodeposition is used for CIGS absorber layer fabrication [155]. Since then a huge progress has been achieved. Electrochemical techniques can be divided in three different approaches [16]: All involved elements can be co-deposited from a single electrolyte, or metals, alloys or binary selenides can be electrodeposited in stacked layers. Electroless and chemical bath deposition are the third alternative. All of these methods require an annealing step after the electrochemical precursor deposition. Efficiencies of up to 13.8 % on a flexible substrate (stainless steel foil) [156] and 15.4 % on glass [157] could be obtained with electrochemical methods. This deposition technique is not dealt with in this thesis. More information can be found in various reviews covering this subject [16, 158, 159].

Particle-based Techniques

An especially promising non-vacuum technique for CIGS solar cells is the particle-based approach which yields the highest accomplished efficiencies so far. As early as 1982 first results for this approach have been published [160]. All particulate processes can be distinguished by the kind of nanoparticles used for the ink. The first discrimination is between elemental and compound particles. Compounds again can be divided into complete CIGS-particles, metal alloys, oxides, and binary selenides.

The simplest particles to use are *elemental particles*, they often are commercially available. The first attempts especially struggled with a large particle size [161]. In the course of further development finer particles were available and better results could be achieved [162]. Yet the finer indium particles tend to oxidise during handling. The occurring indium oxide shell of the particle hinders complete selenisation with elemental selenium vapour [163, 164]. Thus the precursor film has to be reduced prior to or during selenisation. This can be done with a reduction agent in the ink itself or with heating in a hydrogen atmosphere. At ZSW this approach is pursued (see chapter 3.2 and [19]). During the selenisation only the use of H_2Se can overcome the issue of oxidised particles. Some groups even add selenium as nanoparticles [165] and thereby do not need the subsequent selenisation.

Already at an early stage of nanoparticle-based CIGS-research *complete CIGS-particles* have been used for absorber deposition [166]. Up to now complete CIGS-particles without an additional annealing step only yield poor efficiencies [167, 168]. Often no efficiencies are published at all [169–173]. The annealing step is preferably carried out in selenium atmosphere.

Even with an annealing step the efficiencies stay low [174, 175] — the highest reported efficiencies are only 5.4 % for CuInSe_2 [176] (with Se-deficient particles, which improves efficiency significantly [177]), 5.6 % for Cu(In,Ga)(S,Se)_2 [178], and 6.5 % for CuIn(S,Se)_2 [179]. This is most probably related to the high melting point of CIGS [166].

Much easier than this and only slightly more complicated than the one with elemental particles is the approach which uses *metallic alloy nanoparticles*. In general it is much more successful than the attempts using complete CIGS -particles, as the high melting point is irrelevant for this approach. Most publications deal with Ga-free Cu-In-particles [180–182]. In comparison to elemental particles alloy particles are more resistant to oxidation [183] which is an advantage.

Basol et al. reached conversion efficiencies up to 9.4 % [183] and with the use of finer particles even 13 % could be achieved [182]. This is the highest efficiency for particle-based Ga-free absorber layers [16]. Regardless of the fact that the selenisation is more efficient with H_2Se (as already mentioned in section 2.5.1) even layers selenised with this method often show a quasi-bilayer structure [181]. Moreover, this can be found for other particulate approaches [184] but is not necessarily detrimental for the absorber layers.

A quite successful particle-based route employs *oxide nanoparticles*. In general oxides are quite stable and thus selenisation of oxidised precursor layers is challenging. Hence most processes include a reduction step prior to selenisation. Unisun and International Solar Electric Technology (ISET) are responsible for essential research on this topic. Unisun for example reached 11.7 % as reported by Eberspacher et al. [185]. They used solid, multinary, compound particles [186] having the advantage that the chemical composition is the same for all particles. It is not clear how they eliminate the oxygen in the precursor layer. Possibly it happens during the selenisation at atmospheric pressure [185]. Presumably this is facilitated by the use of H_2Se . ISET uses oxide nanoparticles as well. To deplete the oxygen in the precursor layer an aggressive conversion process is used. It includes a reduction in hydrogen atmosphere and a selenisation with the highly toxic H_2Se [187]. With this technique ISET reached 13.6 % [188]. They tried to pursue a commercialisation strategy and set up a pilot production [189].

So far the most successful route for particle-based chalcopyrite absorber layers include *binary selenides*. While for this type of particles there are concepts which yield relatively low efficiencies up to now, like various core-shell concepts (InSe–CuSe 1.1 % [190] or Se–CuSe 3 % [191]), nevertheless the highest reported efficiency of over 17 % could be achieved with binary selenides [192]. The company Nanosolar pushed development with a lot of resources both financially and personnel-wise. All investigated processes are proprietary and one can only assume that they found a way to fabricate various binary selenides with different sizes such that they melt instantaneously during the rapid thermal treatment. When results of over 15 % on aluminum foil were published in a white paper by Nanosolar in 2009 they presented their techniques for the other layers and the interconnection of cells to modules, too [193]. However, in 2013 it became obvious that Nanosolar was not commercially successful either.

All nanoparticle-based approaches have some challenges in common. Due to attractive van der Waals forces particles generally tend to agglomerate [194]. In dispersions used to deposit precursor layers this agglomeration has to be avoided. In addition, there are repulsive electrostatic forces due to an electrical double layer at the surface of the particles. The interaction of these forces between particles is summarised in the DLVO theory which is named after Derjaguin and Landau, Verwey and Overbeek [195, 196].

Depending on pH-value, ionic concentration, solvent and type of nanoparticle, the original electrostatic forces can be strong enough to give a stable suspension and avoid agglomeration. If this is not the case another stabilisation has to be used. This is often done with organic stabilisation agents [168, 197]. Even though they help avoid agglomeration and sedimentation of particles they have to be eliminated later in the process. This is often impossible which leads to the absorber layers having organic residues [198].

Another challenge arises when different particles are used. In general different types of nanopar-

ticles have different settling rates. Thus some sediment faster than others, which leads to an undesired stoichiometric deviation [163].

Fortunately nanoparticle-based methods also offer a lot of advantages and the highest efficiencies for vacuum-free fabricated absorbers are reached with these methods. Consequently experiments with particle-based methods have been conducted for this thesis and some of the results can be found in section 3.2.2 and 4.4.

Solution-Based Techniques

Mixing different elements on a molecular level can be done using solution-based techniques. While particle-based approaches with different types of particles can achieve an intermixture only on the particle-level, solved components in a solution intermix down to the molecular level. For this group of techniques one can distinguish different approaches as well: One for example uses *organometallic precursors*. A possibility for these precursors are copper and indium naphthenates which are used by Merdes et al. [199]. With this approach CIGS-layers have been fabricated, but so far no efficiencies have been published.

A more complicated approach with single-source precursors has been developed by Hirpo et al. [200]. These precursors can be used for chemical vapour deposition (CVD) [201]. Even though it has been pursued much longer than the other technique the achieved maximum efficiencies of 1.0 % are still quite low [16].

Solution-based approaches utilising *selenides* yield the highest efficiencies. To dissolve selenides mostly hydrazine (N_2H_4), a highly toxic and explosive solvent, is used. A lot of research on this topic has been done at IBM by Mitzi et al. [202–204]. The advantages of hydrazine as a solvent are manifold: It acts as a reducing agent, it is small and decomposes cleanly during the process. The additional nitrogen and hydrogen decompose to N_2 , H_2 , and NH_3 [13]. Furthermore it contains no unfavoured atoms like oxygen, carbon or chlorine. So only the desired species are present in the solution and even the required chalcogen can be added to it.

Up to now cells were only fabricated on laboratory scale, by spin coating the precursor solution is deposited on a molybdenum covered substrate and the resulting film is dried and partially decomposed at an elevated temperature of 250 °C to 300 °C. As this film is much too thin, several layers are deposited on top of each other and heated after each deposition step [204]. This is a drawback for the industrial implementation but facilitates the generation of a gallium gradient by using solutions with different gallium content for different layers [16].

Even though this approach has only been pursued for quite a short period the resulting efficiencies are remarkably high. A power conversion efficiency of 15.2 % has been published by Todorov et al. [205].

As hydrazine is highly toxic and explosive, for industrial use a lot of security measures have to be taken into account. To avoid this huge effort alternative solvents are searched for. So far there are only few publications on this topic and they contain no results on solar cells [206].

Other solution-based methods use normal *metal salts* like nitrates and chlorides. Fortunately the undesired elements like N and Cl are volatile during processing or less detrimental than might be expected at first glance. In general the metal salt solution itself is not suitable for printing processes. For the paste to meet printing requirements the viscosity has to be modified. This modification can be done by adding a binder material, which additionally helps prevent both dewetting of the substrate and local cationic segregation due to different solubility and recrystallisation [18, 162].

At the Swiss Federal Institute of Technology in Zurich (ETHZ) a printing process was developed with ethylcellulose as a binder material [12]. The metal salts used are copper and gallium nitrate and indium chloride. This method is used and furthered extensively in this thesis. The deposition methods and parameters are explained in section 3.2.1.

As the binder material is not eliminated completely during the selenisation process a residual carbon layer remains between molybdenum back contact and CIGS absorber layer. Fortunately, this carbon layer is not detrimental to the operation of the solar cells and a maximum efficiency of 6.7 % could be achieved [12]. A detailed characterisation of the carbon layer and its influence on the performance of solar cells is subject of chapter 7.

The same method is used by other groups as well [207] but to date they have not published any efficiencies. Another approach using nitrates for copper, indium and gallium even adds selenium in the form of selenium chloride [208]. However, ethylcellulose is still needed as binder material. This group has published no efficiencies so far, either.

Recently another method using metal salts has been developed by Berner et al. [209]. With this method no binder residues remain in the layer stack and remarkably high efficiencies of up to 11 % were reached.

For the deposition of the metal salt solution spray pyrolysis is another possibility [210–212]. So far not many solar cells have been processed. In publications mainly absorber layer fabrication and characterisation are described. The record for spray pyrolysis is 5 % [213].

An approach for solution deposition developed at the HZB in Berlin (former HMI) is spray-ion layer gas reaction "spray-ILGAR". It is a patented process which was originally developed for buffer layers and oxides. Later the process has also been adopted to chalcopyrites [214, 215]. So far efficiencies of up to 5 % [216] have been achieved for sulfur-containing layers.

Up to now all non-vacuum methods lack the efficiencies comparable to conventional vacuum based techniques. Yet for economic reasons the achieved efficiencies have to be quite close to

the results from other deposition routes. One step towards this goal is to understand the specific characteristics of absorbers fabricated with non-vacuum methods. In the following chapters the attempt is made to understand the specific back contact interface properties. While the previous chapter outlined the general basics of non-vacuum chalcopyrite solar cells the following chapter will present the experimental details for both the characterisation and the precursor deposition methods.

Chapter 3

Experimental Details for Sample Analysis and Preparation of Precursor Based CIGS

All physical investigations and experimental research require a certain amount of experimental equipment and knowledge. In the following chapter all the experimental details used for the characterisation of materials, films and solar cells and the fabrication of precursors are provided. The chapter is divided into two sections.

The first section explains all characterisation techniques used for this work (see section 3.1). For the precursor deposition several methods are employed. They are presented in the second section (see section 3.2).

3.1 Methods of Analysis

To evaluate different processes and study their various effects on physical properties and investigate the physical behaviour of layers and complete solar cells a wide variety of characterisation methods can be used. The following section describes the methods employed for results presented here in this work and is subdivided according to the measured properties:

For this work the chemical composition especially of the absorber layer is quite important. The related measurement methods are introduced in section 3.1.1. Physical properties like thickness and morphology are relevant for the performance of solar cells as well. Methods to determine these are explained in section 3.1.2. Crystal parameters, crucial to polycrystalline semiconductors, are measured with the techniques presented in section 3.1.3. For complete solar cells optoelectronic characterisation is needed to determine the performance. The methods utilised for this are described in section 3.1.4.

3.1.1 Chemical Composition

For the semiconductor $\text{Cu}(\text{In,Ga})\text{Se}_2$ — a quaternary compound — the chemical composition is crucial. It determines the band gap: While CuGaSe_2 has a band gap of 1.68 eV [217], CuInSe_2 has one of 1.04 eV [40]. Thus the alloy $\text{Cu}(\text{In,Ga})\text{Se}_2$ has a band gap in between which is defined by the ratio of gallium concentration to the sum of gallium and indium concentrations (GGI). Another important ratio for CIGS solar cells is the ratio of copper concentration to the concentration of group III metals. It is called CGI. These ratios are also important for the phase formation (see chapter 2.3.1). Various methods can be used for the identification of this composition. The key methods for this work are explained in the following sections.

X-Ray Fluorescence Analysis (XRF)

X-Ray fluorescence analysis (XRF) is a widely used method for the determination of chemical composition (both qualitative and quantitative) and layer thicknesses. It is fast and non-destructive. By the incident X-rays electrons are knocked from the inner shells of the atoms. Electronic transitions from higher levels back to the empty lower levels give rise to a characteristic X-ray radiation which helps identify the constituents of the analysed layer. To be detectable the elements need an atomic number larger than eight (fluorine and heavier elements). Thus for example carbon, which is important for the studied samples and has an atomic number of six, can not be measured.

The XRF system at ZSW is an EAGLE XXL system, equipped with an energy-dispersive Si(Li) detector and a 50 kV rhodium X-ray source. It is designed especially for systems of up to four layers [218]. Both the chemical composition and the layer thicknesses (see section 3.1.2) of the involved layers can be determined with the system. For the examination the system is at 1×10^{-1} mbar. The detection limit is 1×10^{-3} at %.

Energy-Dispersive X-ray Spectroscopy (EDX)

To analyse the chemical composition with a high spatial resolution energy-dispersive X-ray spectroscopy (EDX) has been used. At ZSW a scanning electron microscopy setup is used for this method (for system details see 3.1.2). Similarly to the XRF the X-rays emitted by the sample are analysed with respect to their energy. For EDX the excitation is caused by the scanning electron beam. Each element emits a characteristic spectrum, of which the peaks correlate with the transition between two electron shells of the atoms. Thus the composition can be identified by looking at the complete spectrum emitted by the sample. Considering the quantity of the X-rays — the height of the peaks — even a quantitative chemical analysis is possible. However, for this purpose the incident beam energy and the resulting excitation bulb has to be taken into account. An incident electron beam excites a volume starting at the point

where the beam strikes the sample. The penetration depth is correlated with the beam energy. Thus the higher the beam energy is the more information is gained from the bulk. Since this analysis is laborious, EDX has been used to determine the chemical composition only in cases where a high spatial resolution was needed. For all other purposes XRF has been used.

Secondary Particle Mass Spectrometry (SIMS/SNMS)

Secondary particle (ion and neutral) mass spectrometry is a destructive method which helps to determine the depth-resolved chemical composition of layers. For a compound semiconductor like CIGS the chemical composition is essential. Furthermore the element distribution within the layers is very important for the properties of the solar cell. To control potential grading and monitor variations within thin layers of a layer stack this method is perfectly suited. It also has a high detection sensitivity which makes it an ideal method for the detection of very low concentrations and contaminations or other impurities within a certain layer.

The samples are sputtered with an ion beam and the particles ejected of the top layer are identified by their mass. As layer by layer is removed a depth profile is generated. SNMS and SIMS measurements were made with a SSM 200 from Leybold.

X-Ray Diffraction (XRD)

Since X-ray diffraction is usually used for crystal properties, it is explained in detail in section 3.1.3, but it can additionally be used to give hints towards the chemical composition which is why it is mentioned here. The peak position of the main CIGS-peak shifts with changing gallium content for example.

3.1.2 Layer Texture

For thin film solar cells both the thickness of a layer and its morphology and surface properties are important. For the determination of these parameters various methods are used and described in the following section.

X-Ray Fluorescence Analysis (XRF)

As already mentioned in section 3.1.1 where the method is introduced, the XRF can be used to determine the layer thickness, too. With the help of a stored table the intensity of the measured peaks can be converted into a corresponding layer thickness for a known sample configuration. As it is a fast and non-destructive method which was used as a standard for the chemical composition it is also used to monitor the thickness of all produced absorber layers.

Scanning Electron Microscopy (SEM)

Scanning electron microscopy is a common method for the imaging of surfaces and their morphology. A focused electron beam is scanned over the sample and the secondary electrons are collected with a detector and multiplied. The resulting image of secondary electron intensity is displayed on a monitor. Differences in topology, material and chemical composition can be detected. The microscope used for this work is a FEI XL30 SFEG Sirion scanning secondary-electron microscope (SEM) using a 5 keV acceleration voltage. It has a Schottky field emission gun. The electron beam is generated with an acceleration voltage in the order of several kilovolts. It then gets focused on the sample surface by electric and magnetic lenses. There it produces secondary electrons, back-scattered electrons, X-ray radiation, and other radiation. The depth where this interaction takes place depends on the acceleration voltage and ranges from less than 1 μm up to several μm below the surface. When looking at the cross section one can determine the thickness of the various layers. This method is especially helpful when dealing with new types of layers where the XRF method can not be used.

Confocal Laser Scanning Microscopy

For images with a high in-depth resolution confocal laser scanning microscopy is a method of choice [219]. For the image acquisition a laser is focused on a certain depth of the specimen. All light that stems from points above or below the focus is excluded by an aperture plate. After sequentially scanning the sample at different depths an image containing three-dimensional information is compiled.

This image can be combined with a conventionally obtained optical microscope image to have colour information simultaneously. With an appropriate software one can determine amongst other parameters the layer thickness and roughness of a sample. At ZSW a 3D laser scanning microscope from Keyence (VK9700) is used.

3.1.3 Crystal Parameters

Since CIGS is a polycrystalline semiconductor, crystallinity, grain size and grain orientation are relevant quality measures. At ZSW different techniques are used to determine these parameters.

Scanning Electron Microscopy (SEM)

The scanning electron microscope can be used to acquire images of the cross section through a layer system. These images can help to determine the grain size in a polycrystalline film and give hints on the grain size distribution. The working principle is explained in detail in section 3.1.2.

X-Ray Diffraction (XRD)

To obtain information about various phases and orientation of grains X-ray diffraction is an important tool. It employs the elastic scattering of an X-ray beam from the electrons in the examined thin film and gives information about the atomic structure and the crystallographic properties in general.

The scattered radiation is detected angle-resolved. Each phase and crystal orientation gives a specific set of peaks in the gathered spectrum according to the lattice spacing. By comparing the gathered spectrum with data from the JCPDS (Joint Committee on Powder Diffraction Standards) database one can identify the different phases and orientation of phases present in the thin film. All the measurements are performed with a Siemens D5000 (copper tube) at 40 kV tube voltage and 40 mA tube current.

3.1.4 Optoelectronic Characterisation

For solar cells the optoelectronic characterisation is a central tool. It shows if the solar cell performs the task it is fabricated for, how efficient it converts light into electricity and how possible losses are caused. Therefore the current-voltage characteristics of all completed cells are determined. For certain cells — especially for all cells with record efficiency — quantum efficiency measurements are carried out.

Current-Voltage-Measurement (I - V)

Since the efficiency is one of the key parameter of solar cells and determines various other things, for example the costs per Watt, it is essential to measure the solar cell characteristics. Current-voltage curves are measured using a Keithley 238 source-measure unit under simulated AM 1.5 global solar irradiation with an ORIEL 81192 sun simulator at 100 mW cm^{-2} to extract the basic solar cell characteristics.

Quantum Efficiency (QE)

For wavelength dependent effects and to verify the short circuit current measured with the sun simulator the external quantum efficiency is determined. With this method the probability is measured with which an incident photon of a certain wavelength will add to the photo current. It is called external as the transmitted and reflected photons are taken into account even though they generally can not add to the photo current.

We use OptoSolar SR 300 set-up with a xenon lamp as a white light source and a monochromator to extract the desired wavelength. With a chopper and a lock-in amplifier the signal to noise ratio is improved. Before each measurement a calibration measurement with a silicon and

a germanium solar cell are made. With these the response of the measured cell can be evaluated quantitatively and by integrating over all wavelengths the exact short circuit current can be determined.

With all the methods described above a wide range of analytical techniques is available for the sample analysis and used in this work for the characterisation of single layers and complete cells.

3.2 Precursor Preparation

As already mentioned in chapter 2.5.2 non-vacuum methods are in general two step methods. For safety reasons both on laboratory scale now and in a potential future industrial fabrication we concentrated on selenium-free precursors which are selenised during the second step. Different material classes were used for these precursors: One category uses metal salts with a binder material (see chapter 3.2.1), another one uses nanoparticles (see chapter 3.2.2). Additionally, as a vacuum-based reference process, precursors sputtered from an alloy target were used (see chapter 3.2.3).

3.2.1 Metal Salts with Binder Material

For the metal salt precursors a method developed at ETH Zürich was adopted [18]. The procedure of sample preparation can be seen in fig. 3.1.

Ink Preparation

Due to their good availability and low price nitrates and chlorides were used as metal salts: Copper and gallium nitrate and indium chloride are dissolved in methanol. For some samples only copper nitrate and indium chloride are used to obtain gallium-free layers. The binder material — ethylcellulose — is dissolved in 1-pentanol. The binder material is necessary to avoid dewetting of the substrate and cationic segregation due to different solubility. A few hours before the deposition the two solutions are mixed together. The complete ink can not be stored for a long period because a precipitation of white powder occurs after a few days [162]. So as soon as the two solution are mixed entirely the deposition process should be started.

Doctor Blading

Doctor blading is a fairly simple method for paste coating. The results obtained with this method can easily be transferred to more sophisticated printing techniques. First, the printing paste is placed on the substrate onto which the material is to be deposited. Then the doctor blade is

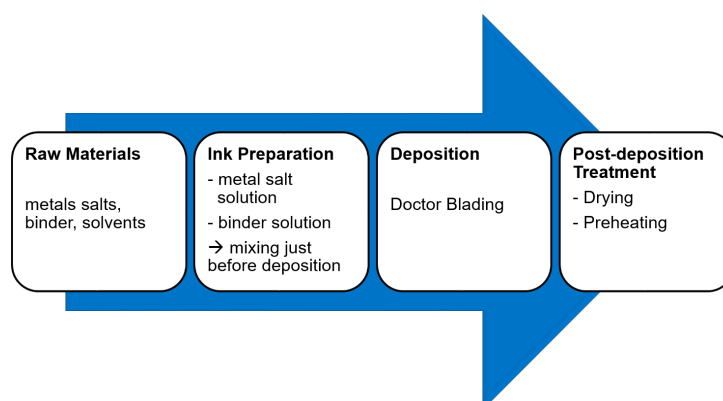


Figure 3.1: Procedure for Preparation of Metal Salt Precursors.

Beginning with the raw materials the inks for doctor blading are prepared. After the deposition the films are heated up - first to dry them and then to higher temperatures to decompose the binder.

moved with a well-defined velocity slightly above the substrate. In this way the material can flow out through the accurately adjusted gap between the blade bottom and the substrate (see figure 3.2). In our case a tool by the Swiss company *Zehntner GmbH Testing Instruments* has been used which allows to adjust the gap steplessly. The resulting film has a uniform thickness, which is influenced among other parameters by the blade distance and velocity. It has to be dried to eliminate the solvent.

Preheating

After depositing the ink onto the substrate it is dried at an elevated temperature for some minutes. Thereafter the layers are sintered in air at 250 °C to 350 °C. During this the ethylcellulose is burned, which produces a change of the colour of the film, indicating the end of the sintering process [162]. This step is decisive for the later adhesion of the selenised layer.

Resulting Layers

The result is an amorphous, homogeneous layer with a thickness of approximately 1 µm, which can be seen in figure 3.3. With the XRF thickness routine (see section 3.1.2) one can determine an equivalent thickness of the precursor. This thickness is not a true absolute value but can be used to find relative deviations within the film. In figure 3.4 one can see that the edges are in general thicker than the central part. At the position where the blading process starts the precursor layer is usually thinner and towards the end of the process the depleted solution leads to slightly thinner layers and uncoated areas.

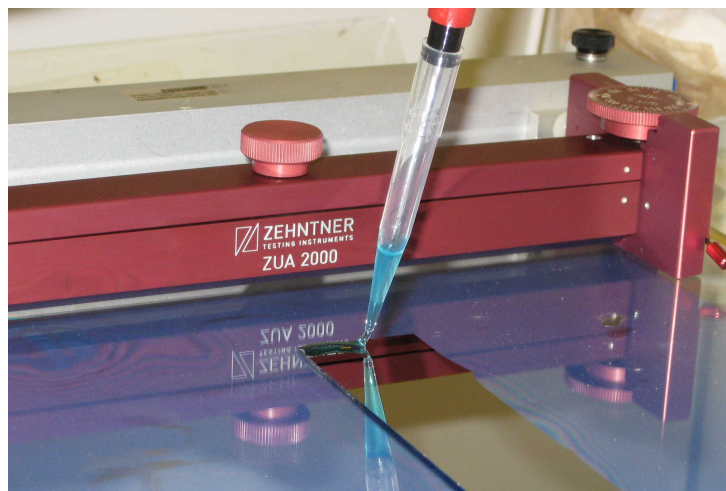


Figure 3.2: Doctor Blading of Metal Salt Solution.

After placing the printing paste on the substrate it is distributed evenly with the doctor blade using a well-defined gap and coating velocity.

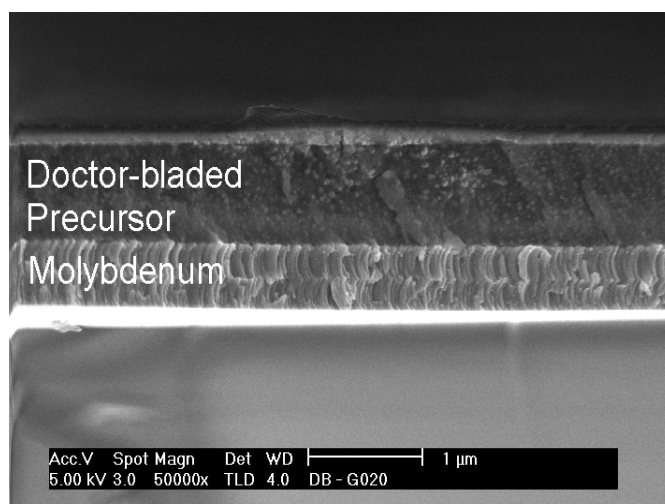


Figure 3.3: SEM Image of Doctor Bladed Metal Salt Precursor.

In the SEM image of the doctor bladed precursor one can see an amorphous, homogeneous layer with a thickness of approximately 1 μm .

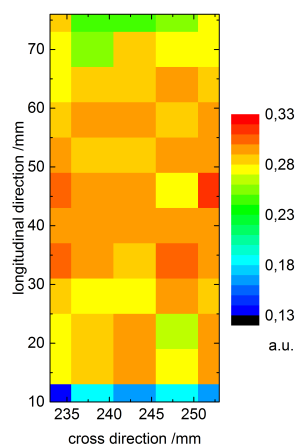


Figure 3.4: Mapped Thickness of Doctor Bladed Metal Salt Precursor Measured by XRF.

While the edges, the beginning, and the end of the deposited layer show inhomogeneities the central part of the precursor is smooth.

To estimate the quality of a precursor layer the spatial deviations of the chemical composition are an important criterion. The XRF measurements can be used to determine CGI and GGI (see section 3.1.1). In figure 3.5 one can see that the deviations are independent of the blading direction. They are in the range of $\pm 10\%$ which of course is improvable but does not deteriorate the absorber layer.

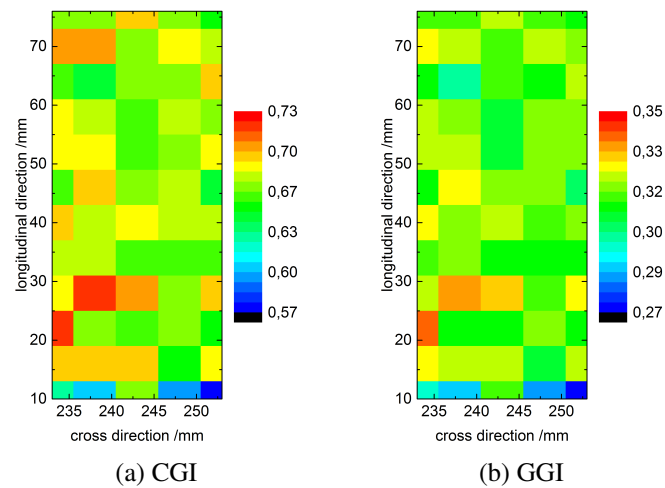


Figure 3.5: Composition of Doctor Bladed Metal Salt Precursor Measured by XRF.

The chemical composition of doctor bladed precursors is fairly uniform. Both CGI (a) and GGI (b) show only small variations. These variations are independent of the blading direction.

3.2.2 Nanoparticles

For the nanoparticles approach elemental copper and indium particles were used. They are commercially available and even though the quality is not high grade, solar cells can be fabricated with them. Details of the analysis, the fabrication of precursors, and the selenisation can be found in [19, 220].

Material Characterisation

For the copper particles the manufacturer of the nanoparticles (CANANO TECHNOLOGIES) states that they are pure copper particles with either a shell of copper oxide or of a copper cobalt alloy. Since no cobalt could be detected during all our analysis it is assumed it is a copper oxide. The indium particles have an oxide shell as well. With SIMS/SNMS measurements the oxide content in the fabricated layers could be determined around 20 mol%. It cannot be distinguished between oxygen originally present in the particles and oxygen from the preparation process. Quite surprisingly significant gallium contaminations can be found in the copper particles (over 6 mol%). As it is not typical contamination for copper it is assumed that it is caused by the special fabrication process of CANANO TECHNOLOGIES. The second batch which was purchased did not contain any gallium anymore.

The size of the primary particles is 10 nm to 100 nm. However, they form agglomerates of about 20 μm and larger. These agglomerates have to be taken into account when preparing the ink and the films, as they will otherwise be detrimental to the fabrication of thin films.

Ink Preparation

Particle-based inks are fabricated in two ways: With and without a stabilising agent.

Inks without a stabilising agent are fabricated by dispersing the nanoparticles in ethanol. The resulting slurry is homogenised with an ultrasonic generator (SONOPLUS HD 3100 by Bandelin). During the application of the ultrasonic sound the slurry is cooled by a simple water cooling system.

The preparation of inks with stabilising agent involves more steps the details of which are described in [220]. The resulting inks can be used for doctor blading of precursor films.

Spin-Coating

For this method the substrate is flooded with the ink, the excess is spun off, and a uniform layer of precursor remains. The method itself is not suitable for industrial production, but for research purposes it is particularly suitable as a wide range of viscosities can be covered and small substrate areas can be used. Thus it presents an opportunity to test a variety of ink formulations. It was used mainly for inks without stabilising agent.

Doctor Blading

A thicker paste with stabilising agent was used for this technique. It facilitates the coating enormously and furthermore it provides the possibility to compare the gained results more easily to the ones with metal salts. Unfortunately it yields a gradient along the blading direction, both in composition and in thickness. It is important to keep this in mind when choosing sample parts for the detailed examination.

Reduction

As described in chapter 2.5.2 most metallic nanoparticles are covered with an oxidised shell. For a selenisation in H_2Se the oxides would not cause any problems. Nonetheless one requirement for the selenisation was to avoid the highly toxic H_2Se . Thus the removal of oxygen and the introduction of selenium into the film is separated. To get rid of the oxygen a reduction step is introduced in the precursor preparation. The reduction could not be carried out in a plasma chamber (with forming gas) nor with any other conventional equipment available at ZSW. Therefore a new set-up has been built for the reduction on a lab scale. This set-up is designed on the basis of standard equipment used for redox experiments and can be seen in figure 3.6. The main apparatus consists of a quartz glass tube closed with two plugs, which has a carbon carrier inside to secure homogeneous distribution of the introduced heat (A). The gas flows through two washing bottles, one containing acid sulphur to dehumidise the gas and one empty bottle serving as splash guard. After purging the tube with nitrogen the hydrogen can be introduced (B and C). At the end of the reaction area the gas leaves the glass tube via a second, bent glass tube where a copper net avoids oxygen introduction. The remaining hydrogen is burnt off (E) mainly for security reasons. Additionally the colour of the flame can act as an indicator whether any other species leave the precursor film. The heat needed for the reaction is introduced via a Bunsen burner. The reaction temperature is always kept well below $500\text{ }^\circ\text{C}$ and the time used for reduction is typically less than 5 min. The colour of the films changes dramatically indicating a change in the composition. Consequently, SIMS measurements show a significantly lower oxygen content of the reduced samples (see figure 3.7). The resulting layers can be used for the selenisation step. To avoid re-oxidation the samples have to be transferred to the furnace as quickly as possible.

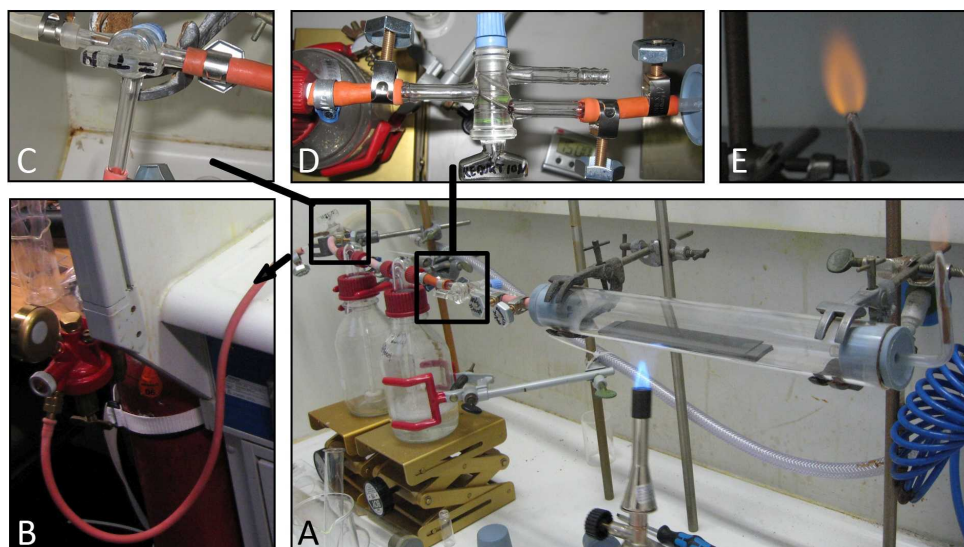


Figure 3.6: Reduction Equipment.

For the reduction of oxygen-containing nanoparticle-based films a lab scale apparatus was set up. The samples are heated in a quartz tube with hydrogen atmosphere. The rest of the set-up is due to safety reasons with regard to the usage of hydrogen and to avoid undesired introduction of oxygen after the reduction. A detailed description is given in the main text, figure taken from [220]

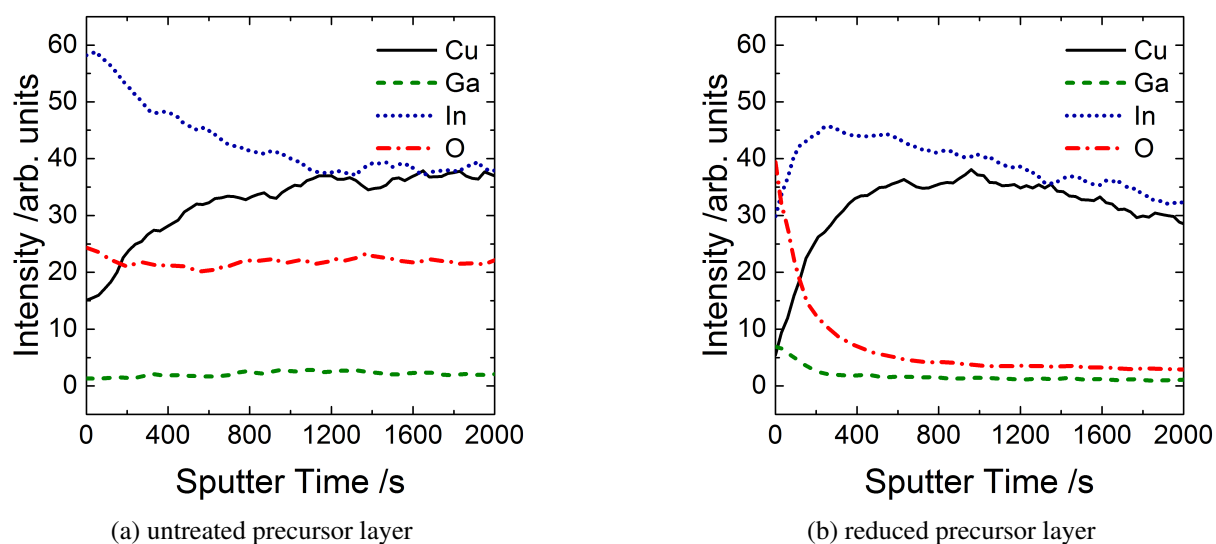


Figure 3.7: SIMS and SNMS Measurements of Nanoparticle Precursor Layers.

While untreated precursor layers show a significant oxygen content throughout the layer, after reduction a significant amount of oxygen can be found only at the surface. Within the layer the oxygen content is substantially lowered.

3.2.3 Sputtered Alloy

As our fabrication process for CIGS layers comprises two steps it is important to be able to distinguish the influence of the different steps. Thus a conventional vacuum-based deposition method for precursor layers is needed as a reference process. In order to stay with simple one-step deposition methods an alloy target consisting of copper, indium, and gallium is used. This single deposition step is simpler than, for example, the conventional SEL process described in section 2.5.1. It still is a relatively cheap process so that the results should be comparable in quality to those of the vacuum-free processes.

Sputtering Details

The target used for the precursor preparation is by Heraeus and is fabricated from micro-alloyed powder with 48.5 at% copper, 38.5 at% indium, and 13.0 at% gallium [221]. Standard parameters for the sputtering process are a DC power of 0.5 W cm^{-2} , an argon flow of 30 sccm, and no additional heating of the substrates [222]. In general a precursor layer with $1 \mu\text{m}$ thickness is needed in order to obtain a absorber layer of $2 \mu\text{m}$. This thickness corresponds to a sputtering time of 1000 s. For a better understanding of the sputtering process this time is varied from 100 s to 2000 s in certain experiments. The process gas pressure usually is $10 \mu\text{bar}$ and is varied in some experiments from $1 \mu\text{bar}$ to $15 \mu\text{bar}$.

Layer Characteristics

Obviously with increasing sputtering time the thickness of the precursor layers increases. However, the morphology and particularly the surface character change as well with increasing sputter time. The sputter rate is roughly one nanometer per second. Precursor layers are two-tier — they consist of a rather homogeneous part adjacent to the molybdenum and a more corrugated irregular top layer.

At the beginning of the sputter process the bottom layer is formed with a morphology comparable to that of the molybdenum layer. After 100 s of sputtering only scattered island-like beads can be seen on top of the bottom layer (see figure 3.8). With increasing time more and more area is covered by the irregular top layer. After 2000 s the bottom layer can hardly be seen any more. EDX allows a space resolved measurement of the chemical composition which is quite different for bottom and top layer (see table 3.1). The composition of the complete layer is copper-poor which is important for the subsequent selenisation, since copper-rich conditions usually lead to shunted solar cells.

Another important parameter to influence the characteristics of the precursors prepared with the sputter process is the pressure in the chamber during this process. Its influence on layer

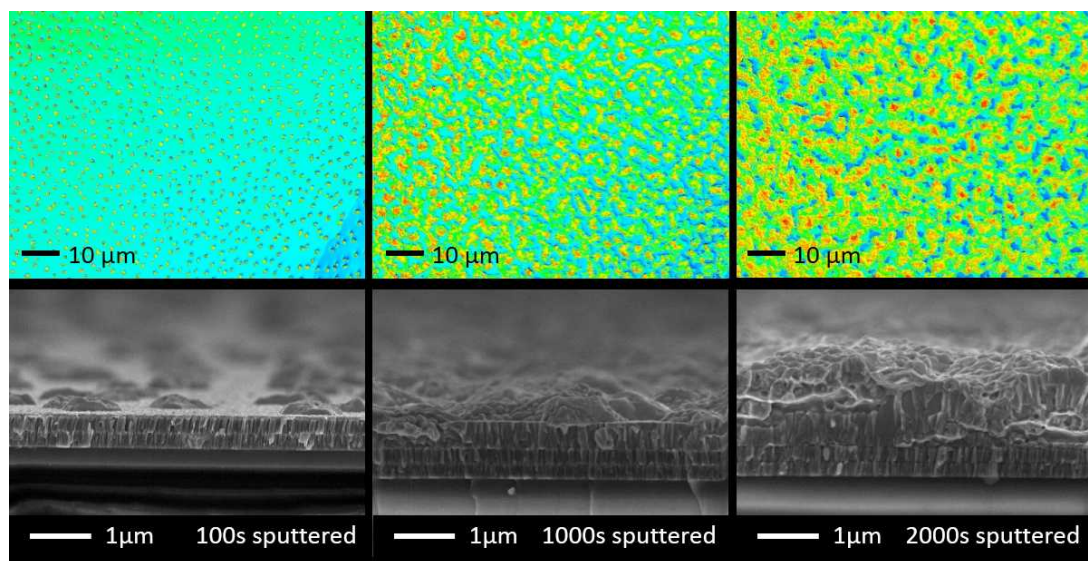


Figure 3.8: 3D-Microscope and SEM Pictures of Sputtered Precursors with Different Sputter Times.

For short sputter times only scattered island-like beads have formed on a rather homogeneous bottom layer. With increasing sputter time more and more area is covered by the irregular top layer.

| Layer | Cu/at% | In/at% | Ga/at% | CGI |
|----------------|--------|--------|--------|------|
| bottom layer | 64 | 21 | 15 | 1.78 |
| top layer | 44 | 48 | 8 | 0.79 |
| complete layer | 46 | 43 | 11 | 0.87 |

Table 3.1: Chemical Composition of Sputtered Layer Measured by EDX.

While the bottom layer of the sputtered precursor is copper-rich, the top layer is copper-poor and indium-rich. The complete layer has a copper to indium and gallium ratio (GGI) of 0.87 for 1000 s sputter time.

properties like morphology and composition is studied in detail in [222]. The morphology can be changed only slightly whereas the composition can be adjusted more easily with this process parameter.

For all experiments shown in the following chapters the standard parameters of 1000 s and 10 μ bar are used. The roughness of these precursors is tested with the help of the confocal 3D-microscope (see figure 3.9). This rough surface facilitates the subsequent selenisation where the actual absorber is formed. For its resulting thickness to be homogeneous the precursor layers as well have to be homogeneous in thickness and composition. With the same colour code for relative deviations from the absolute thickness as in figure 3.4 the differences in thickness can hardly be seen. Only when two samples from the same sputtering process are measured and displayed next to each other small thickness variations due to the sputter chamber configuration can be seen (see figure 3.10). Like mention in the section about metal salt based precursors (3.2.1) one has to keep in mind that the precursor thickness measured by XRF is an equivalent thickness as the evaluation routine is optimised for complete absorber layers, yet a relative comparison is possible and even the absolute values are in relative good agreement to SEM measurements of the average thickness. Furthermore the homogeneity in the composition of the precursor layers is very high and only small deviations can be found (see figure 3.11). Once again to facilitate comparability the same colour code (for relative deviations) as for the doctor bladed metal salt based precursors in figure 3.5 is used.

All in all these sputtered precursors serve as a good reference for the non-vacuum precursors as they are fabricated reproducibly and homogeneously.

In this chapter the fabrication of three groups of precursors has been described — two of these with non-vacuum methods and one with the conventional sputter method which acts as a reference process. All three groups of precursor layers are selenised in the subsequent step which is described in detail in the following chapter.

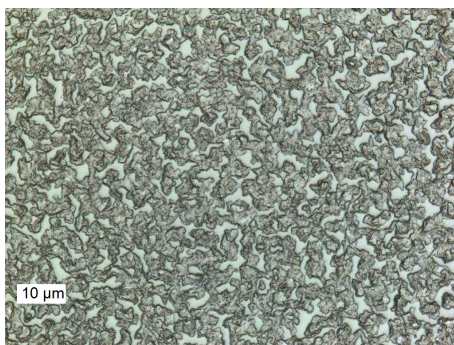


Figure 3.9: Roughness of Sputtered Precursors.

In general the sputtered precursors have a rough surface which can be seen clearly in this figure. The length of the white bar shows 10 μm .

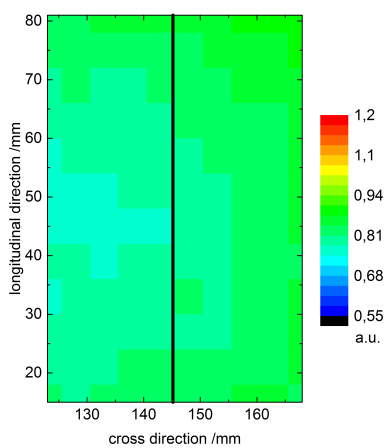


Figure 3.10: Mapped Thickness of Sputtered Precursor (Two Samples) Measured by XRF.

When measuring the thickness of two samples next to each other the small thickness variations due to the sputter chamber configuration can be seen.

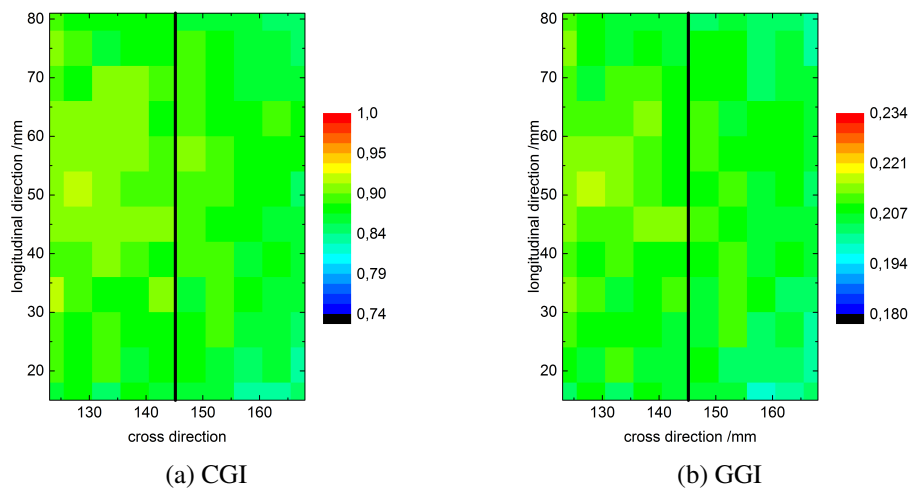


Figure 3.11: Composition of Sputtered Precursor Measured by XRF.

The chemical composition of sputtered precursors is very uniform. Both CGI (a) and GGI (b) show only small variations. These variations are caused by the sputter chamber configuration.

Chapter 4

Selenisation of Precursors

Non-vacuum preparation methods for CIGS solar cells are all based on a sequential process. As the conventional preparation method at ZSW is co-evaporation, no established selenisation method was available. However, this is a crucial part of the preparation, since formation and crystallisation of the CIGS compound take place in it (see figure 2.10). Thus a very important task within this work was to establish a selenisation method and come to terms with the peculiarities of sequential processes. The following chapter gives an overview over the developed selenisation method and the most important results obtained with it. After an introduction into the topic of selenisation in general (4.1), the details of the developed selenisation method are explained (4.2) and then the results achieved with various precursors are presented. This starts with the non-vacuum based precursors, first the ones made from metal salts (4.3) and after that the ones based on nanoparticle inks (4.4), and then as a reference the sputtered precursors (4.5) are discussed.

4.1 Overview

In this section an overview of the selenisation step both in general and specific for this work is given. First the common research in this field conducted prior to this work is reviewed and later the standards for our specific selenisation method are shortly discussed.

Both for conventional and for non-vacuum preparation selenisation of precursor layers is an important step. During this step the selenium is incorporated into the chalcopyrite structure. The energy needed for it usually is provided through high temperatures during the process. The reaction path of the selenisation process is topic of various publications [135, 136, 223–226]. In general one can say that in the first phase of a selenisation — either at lower temperatures or just at the beginning of the process — binary selenides are formed. At higher temperatures or later in the process these binary selenides react to form the complete chalcopyrite. First the indium-

containing species and at higher temperatures the gallium-containing species are formed. The precise reaction path depends on the selenisation conditions.

Several research groups work in the field of selenisation, thus many different ways of selenising various precursor layers have been investigated. One way to differentiate all these approaches is the chemical form of the selenium. Elemental selenium (whether cracked or not) and in a compound with hydrogen (H_2Se) are the most common possibilities, but other selenium-containing molecules have been used for selenisation as well.

Elemental Selenium — The most simple approach uses elemental selenium. Its reactivity is relatively low as selenium usually consists of clusters (mainly rings) of more than 4 atoms — usually 8, [227–229]. Hence this method is not applicable to oxides in general. For such precursors a preceding reduction step is required. However, it works for most other precursors and is therefore widely used for the selenisation step [129, 136, 138, 139, 230, 231]. The challenge for this method is to achieve a high partial pressure in the selenisation chamber early enough during the selenisation. Thus some groups for example use a closed graphite box with a selenium excess to ensure a high enough partial pressure of selenium [129, 232]. Another commonly used method is to evaporate amorphous selenium on top of the metal layer stack (SEL — stacked elemental layers) [233, 234]. With this method the presence of enough selenium at the beginning of the process is ensured without having an external selenium source.

Cracked Selenium — To avert the rings that are common for elemental selenium [228] and still avoid the toxicity typical for H_2Se selenium is activated ("cracked") [235, 236]. There are different methods for the cracking itself. Ishizuka et al. use RF-cracked selenium [237, 238], although plasma-assisted cracking is possible, too [239].

Hydrogen and Selenium / H_2Se — The most effective method so far uses H_2Se . Alberts et al. compared elemental selenium and H_2Se and found that H_2Se is much more effective [140, 240]. It is applicable to all precursors. Important drawbacks are its high toxicity which requires sophisticated safety measures [241] and the high material and process costs.

Other Selenium Supplies — Other selenium containing compounds are used for the selenisation as well. Diethylselenide which is used by Sugiyama et al. is an example [242] as well as dimethyl selenide complexes [243, 244] and ditert-butylselenide [245] or selenoamide which decomposes to H_2Se at relatively low temperature [246]. They are not commonly used yet, but nonetheless basic research is done [141, 242–245, 247–249].

4.1.1 Specific Selenisation Tasks

In this work there is no selenium in the precursor layers, the selenisation is done completely during the second step of the sample preparation. The incorporation of selenium and the formation and crystallisation of CIGS have to take place in this step. The selenium is provided in elemental form to avoid safety issues inherent to other methods. For the metal salt based precursor the binder material was supposed to vanish. As it does not vanish completely a residual carbon layer between evolving absorber and molybdenum back contact is formed during the selenisation.

4.2 Selenisation Details

After explaining the selenisation in general the ZSW specific method is described in detail in the following section. First the typical selenisation set-up is exemplified and then the critical parameters are specified. With these parameters a standard selenisation is described. In the end of this section a reference for a vacuum-based selenisation is presented.

4.2.1 Selenisation Set-Up

The selenisation set-up was designed to use low-cost equipment and process steps to demonstrate the potential of a real low-cost preparation approach. As oven a tube furnace by Carbolite as shown in fig. 4.1 is used. While the furnace itself is a commercially available set-up, the tube, the slide carriers, the housing, in brief all the surroundings are specifically designed and / or assembled for this particular set-up.

As selenisation tube a stainless steel tube is used. It is robust, durable and relatively cheap. All these properties together with its low reactivity to selenium make it a suitable material for a selenisation tube. It has a diameter of 10 cm and is more than twice as long as the furnace. Its length allows for the oven to be slid completely away the sample holder within the tube without opening the tube or moving the samples.

The oven itself can reach a maximum temperature of 1200 °C at its middle position and has a temperature profile which is influenced by the thermoconductivity of the stainless steel tube. This profile can be used to define a lower temperature for the selenium source by positioning it away from the centre position towards the cooler furnace edge.

Configuration

In figure 4.2 a schematic representation of the selenisation set-up is shown. It consists essentially of the furnace, the steel tube and a slide carrier where both the samples and the selenium source are placed on (see figure 4.3). On the rightmost end of the tube there is a needle valve which

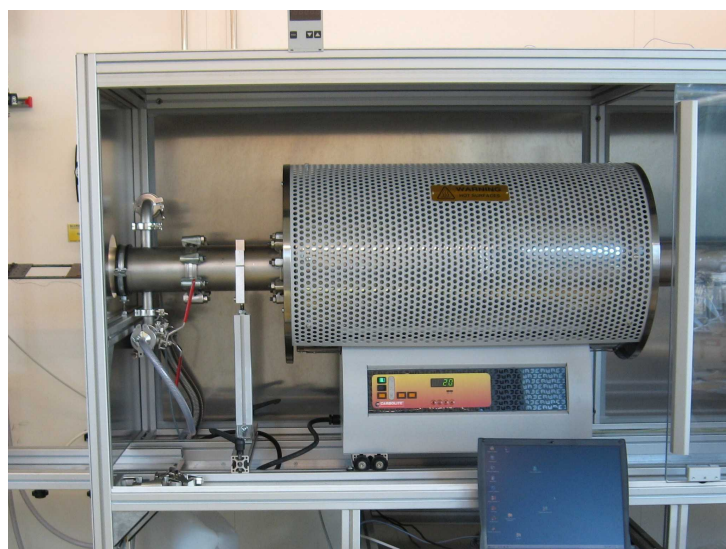


Figure 4.1: Tube Furnace by Carbolite.

For the selenisation step a commercially available tube furnace by Carbolite is used. A maximum temperature of 1200 °C can be reached with the oven itself, but the stainless steel tube used in this set-up sets a limit for the temperature which is lower — roughly 750 °C.

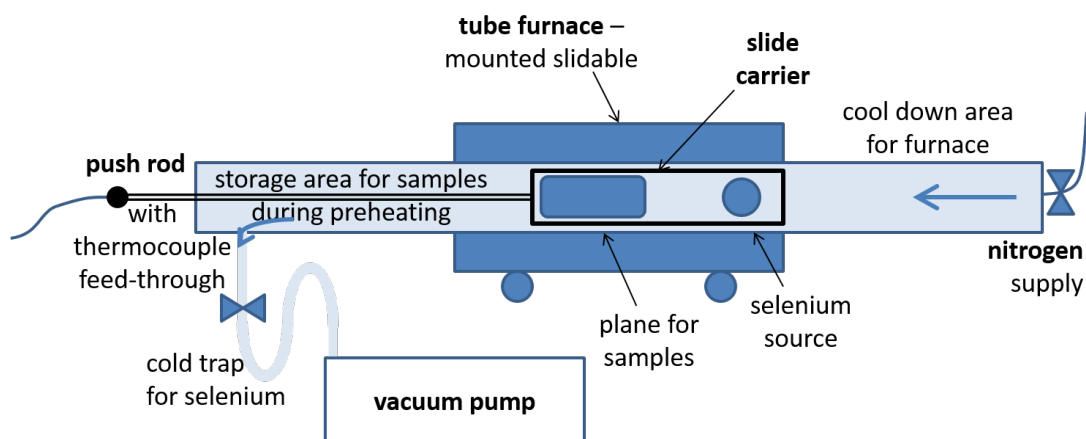
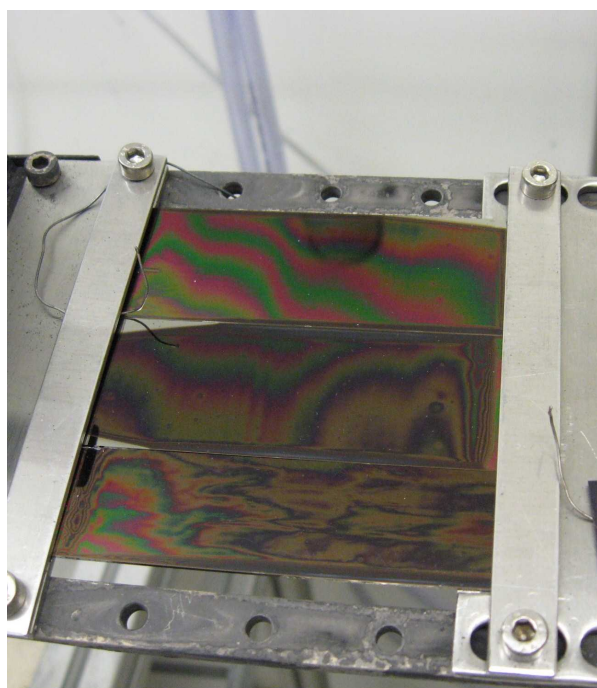
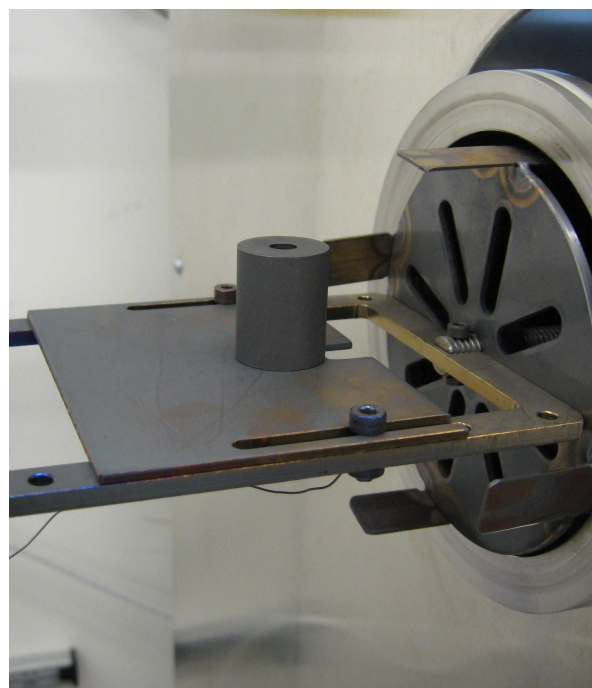


Figure 4.2: Schematic Selenisation Set-Up.

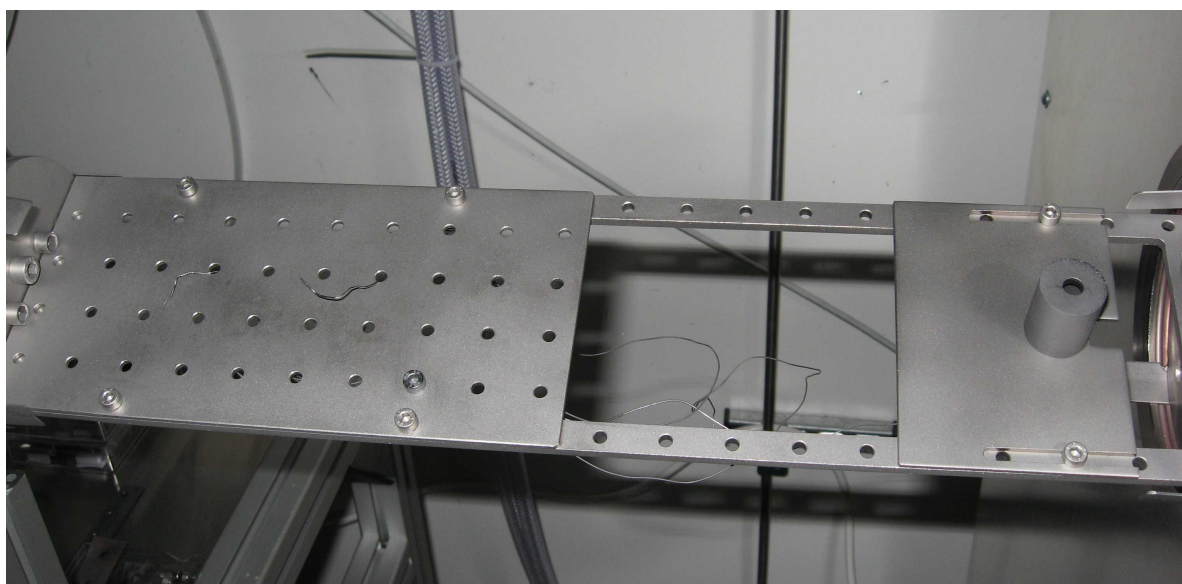
Both the tube furnace and the sample carrier are slidably mounted to allow for different settings: In the beginning of the selenisation the slide carrier is inserted into the tube furnace, at the end of the process the furnace is moved away to accelerate cooling-down. Auxiliary equipment ensures a controlled atmosphere within the tube during the whole selenisation step and avoids undesirable leakage of selenium.



(a) mounted samples



(b) selenium source



(c) slide carrier

Figure 4.3: Slide Carrier with Samples and Selenium Source.

The slide carrier offers a large area for samples on the left and a flexible position for the selenium source on the right.

helps control the nitrogen gas flow. On the left side a tube branches off to the rotary vacuum pump. A cold trap where the selenium is precipitated is located before the pump. Likewise on the left side, a gauge head is placed with which the process pressure is measured. To have a flexible set-up not only the furnace but also the carriers are slidable. While the selenium source is placed closer to the nitrogen purge the samples are mounted on the plane on the left side where the nitrogen and the selenium are pumped out. The complete carrier is a modular system so that it offers various possibilities to place and fix samples with respect to the selenium source. Even though there is a possibility to place samples at a different angle to the tube axis all experiments shown here are made on the carrier with an angle of 0° as it is the one which offers the largest area.

During the preheating of the furnace the carrier is placed in the leftmost position to ensure that the samples remain at a lower temperature while the furnace is heated to the preset temperature. When the furnace and the tube have reached this temperature the selenium source is preheated for a short time and then the samples are slid into the heated region of the furnace. To avoid unacceptable leakage of selenium a special lead-through at the left end of the tube where the sample holder is inserted and a speedy handling during the selenisation are necessary.

4.2.2 Influencing Factors

Each selenisation is defined by a set of parameters. The most important ones are the temperatures — both of the selenium source and of the samples. While the *maximum sample temperature* can easily be set by adjusting the furnace temperature, the controlling of the *selenium source temperature* is more difficult:

To allow for a temperature difference between samples and source the temperature gradient of the furnace can be used and the position of the source on the carrier determines its temperature during the process. This resulting temperature is influenced by various other factors and thus this position has to be determined for each selenisation variation individually.

As mentioned above the selenium source is preheated shortly before the selenisation itself. The temperature of this preheating step (determined by the position in the furnace) and its duration are other important parameters. The duration of the complete selenisation is defined as follows: It starts after the preheating of the selenium source with the insertion of the samples into the heated zone of the tube and it ends with the removal of the furnace. However, especially for very short selenisations, the process does not stop then since both samples and selenium source are still kept hot by the heated steel tube.

During the selenisation step the tube is purged with nitrogen as a carrier gas at a constant

nitrogen flow. In general the pressure is 10 mbar. To analyse the pressure dependence process pressures between 0.1 mbar and 100 mbar were used.

4.2.3 Standard Parameters for Influencing Factors

The selenisation method described here has been tested and optimised for various precursor materials. The main focus of this work are vacuum-free prepared absorber layers. Therefore two types of printed precursors have been used. One sort has been printed with an ink based on metal salts and a binder material (MS-EC) and another one with nanoparticles (NP). In addition sputtered precursors (SP) have been used as reference samples. The details of the precursor preparation are presented in chapter 3.2.

For standard selenisation processes the most important parameters are kept the same unless stated otherwise. The pressure is always kept below atmospheric pressure for safety reasons. In standard selenisations it is adjusted to 10 mbar. The temperature of the tube furnace during the selenisation step is set to 550 °C while it has higher temperatures (650 °C to 700 °C) during the preheating phase. The duration of the standard selenisation (as defined above) is 30 min. Even though for the different precursors different durations are ideal.

4.2.4 Reference Selenisation – High Vacuum Selenisation (HV)

The preparation of chalcopyrite absorber layers is a two-step process. As both steps were newly implemented at ZSW during the last years it is advisable to have a conventional reference process which is reliably reproducible. For the precursor preparation the sputter process is developed as such a reference process (see chapter 3.2.3). For the selenisation step a similar reference is needed.

To have a vacuum process a CIGS evaporation system is used where the metal sources are switched off. The system simulates an in-line process, the samples are moved circularly over a window through which the selenium vapour diffuses. A temperature profile can be seen in figure 4.4. The selenium source is kept at a fixed temperature whereas the temperature profile of the samples shows a steady rise with a distinct peak towards the end of the selenisation. The complete process takes place in a high vacuum, the pressure is as low as about 1×10^{-6} mbar. This low pressure is the reason why a lower selenium source temperature (of 350 °C) is needed for the vacuum based method. The partial pressure of the selenium is still assumed to be higher for this temperature. Many methods in literature use even lower temperatures for the selenium source [207].

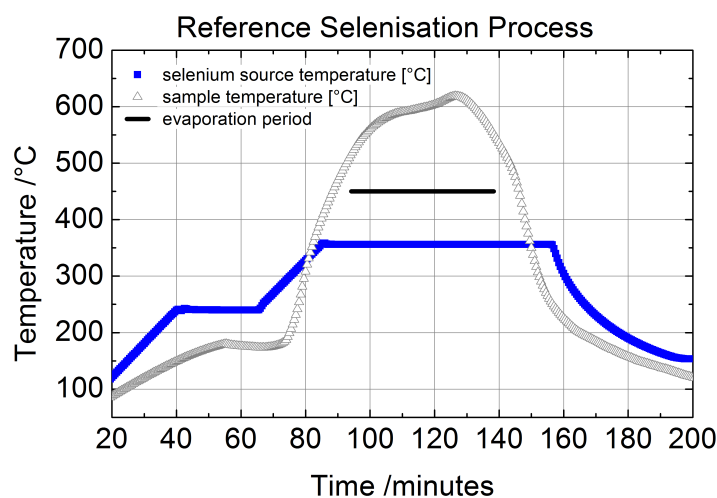


Figure 4.4: Temperature Profiles for the Reference Selenisation.

While the selenium source is kept at the set temperature the temperature profile of the samples rises steadily with a distinct peak towards the end of the selenisation.

4.3 Metal Salts with Binder Material — Doctor Bladed

With the selenisation described above various precursors are selenised. The precursor layer preparation itself is explained in chapter 3.2.1. In the following chapter the selenisation of doctor bladed precursors is discussed. During the selenisation the precursor layers are transformed into CIGS absorber layers. The binder material forms a residual carbon layer between the molybdenum back contact and the absorber layer (see fig. 4.5). Even though this carbon layer is often much thicker than the actual absorber layer it does in general not impair the cell operation. SIMS and SNMS measurements show that this carbon layer not only contains carbon but also has residues from the metal salts. Especially gallium tends to stay in the carbon layer and does not migrate to the absorber layer due to thermodynamics. Thus the resulting absorbers often contain very little to no gallium at all. As is often the case for sequential processes, the gallium concentration displays a stronger gradient than desirable.

In standard sample preparation the absorber layers are much thicker than shown here for our doctor bladed precursors. With this method we managed only quite thin layers as the adhesion of selenised layers deteriorated for thicker layers. Nonetheless we could demonstrate a power conversion efficiency of 6.4 % for these very thin absorber layers (see fig 4.6). The CIGS layer in this record cell has a thickness of slightly more than 200 nm. An SEM image (fig. 4.5) shows the thin absorber layer and the rather low film quality. While Kaelin et al. demonstrated a power conversion efficiency of 6.7 % [12], our samples had thinner absorber layers, so that, in general, we could not reach the same efficiency.

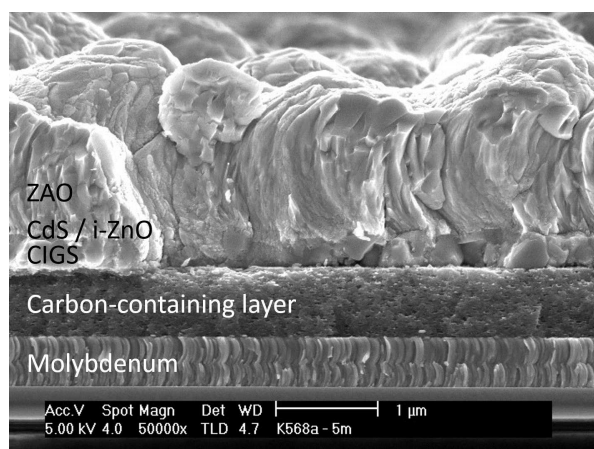
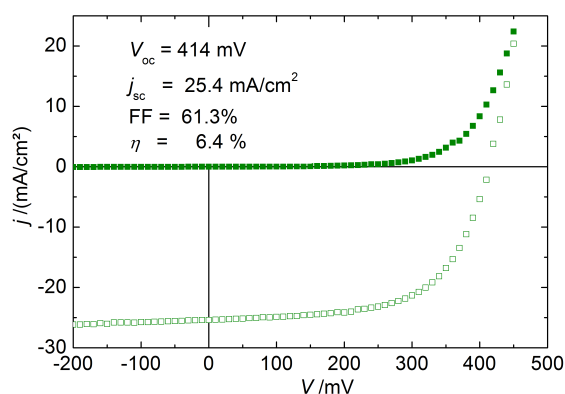


Figure 4.5: SEM Picture of a Gallium-containing Solar cell (Doctor Bladed Precursor, Tube Furnace Selenisation).

In this SEM picture the complete solar cell can be seen. The absorber is fabricated with a doctor bladed precursor by a tube furnace selenisation. Below the quite thin absorber layer a thicker residual layer consisting mainly of carbon has evolved.

| Parameter | Value |
|-----------------|-----------------------------|
| Precursor | Ga-containing doctor bladed |
| Selenisation | tube furnace |
| - temperature | 550 °C |
| - duration | 60 min |
| Selenium source | standard |
| - temperature | 490 °C |

(a) parameters



(b) I - V -characteristics

Figure 4.6: Characteristics of Tube Furnace Selenised Doctor Bladed Ga-Containing Precursor.

I - V -characteristics show quite good results with regard to the thin absorber layer. The residual carbon layer does not deteriorate the cell operation (see chapter 7).

4.3.1 Gallium-free Precursor Layers

To study the influence of the additional carbon layer (see chapter 7) gallium-free precursors were fabricated. With these precursors gallium-free carbon layers can be guaranteed. The results for gallium-free absorbers show no fundamental difference to the gallium containing layers which already contain only a small amount of gallium. Nonetheless the maximum efficiencies reached are lower as neither the precursor deposition nor the selenisation step were optimised for these precursors which are not in the focus of this work. For the sake of completeness, however, the results are shown here as well. The morphology is quite different to the standard sample. The best cell shows a conversion efficiency of 3.3 % as one can see in figure 4.7.

4.3.2 Composition Change During Selenisation

The easy adjustment of the chemical composition in the printing ink is often mentioned as one of the advantages of printing techniques for the fabrication of compound semiconductors. This point only holds if the composition of the precursor layer, i. e. the ratio of the metals to each other, is not altered during the selenisation step.

Whereas this is usually the case for sputtered precursors it is not always true for metal salt based precursors (see table 4.1). For these precursors avoiding the changes in the chemical composition during selenisation is challenging. For the originally used process options it was much too high. SIMS-measurements show that gallium is largely left behind in the carbon layer. The XRF-measurements measure the complete layer stack and show a strong indium deficiency. These two effects together result in a copper excess which is detrimental for the solar cell operational capability. Copper excess leads to a copper selenide phase which is highly conductive and shunts the resulting solar cell. It can be etched away before buffer layer deposition, but the resulting layer is still worse than a low copper grown film. Besides, with these material losses (indium during selenisation, gallium in the carbon layer and copper and selenium during etching) the resulting layer is much thinner than it can potentially be. All these factors also lower the efficiency substantially.

With an optimised selenisation the change in composition can be strongly reduced. We then see an increase in maximum efficiency for this type of precursors.

4.3.3 Selenium Partial Pressure at Start of Crystallisation

For the selenisation process the condition of the selenium right at the beginning of the process is crucial. If the complete slide carrier is inserted into the furnace at once the selenium source is cold at the beginning and heats up more slowly than the sample. The low temperature of the selenium source leads to a deficiency of selenium at the beginning of the selenisation which is disadvantageous for the crystal formation and thus for the solar cell performance. Hence for

| Parameter | Value |
|-----------------|--------------------------|
| Precursor | Ga-free doctor bladed |
| Selenisation | tube furnace |
| - temperature | 550 °C |
| - duration | 60 min |
| Selenium source | standard |
| - temperature | 490 °C |

(a) parameters

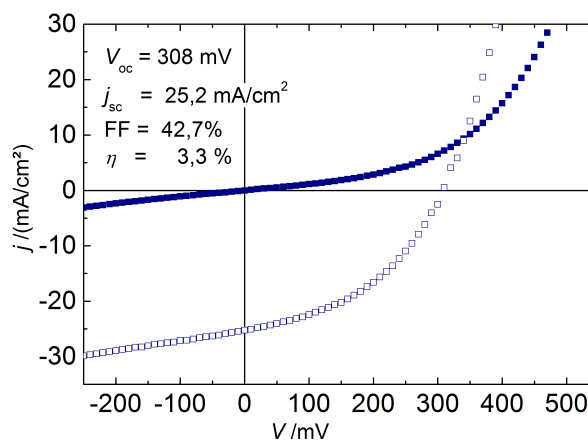
(b) I - V -characteristics

Figure 4.7: Characteristics of Tube Furnace Selenised Doctor Bladed Ga-Free Precursor.

The Ga-free precursors are selenised with the same selenisation parameters as the Ga-containing layers. As neither the deposition nor the selenisation are optimised for this type of precursor the efficiencies reached are much smaller.

| selenisation | simple | optimised |
|------------------|--------|-----------|
| copper / at.-% | 36.5 | 26.2 |
| indium / at.-% | 5.6 | 16.9 |
| gallium / at.-% | 11.6 | 10.6 |
| selenium / at.-% | 46.3 | 46.3 |

Table 4.1: Composition Change for Different Selenium Partial Pressure at the Beginning of the Selenisation With Metal Salt Based Precursors.

A simple selenisation with low selenium partial pressure at the beginning of the step the composition change for metal salt based precursors is dramatic. With an optimised selenisation where the partial pressure is already higher at the beginning of the selenisation itself the change is much smaller.

a favourable process the selenium source has to be preheated. In the case of the tube furnace the slide carrier can be inserted only partly so that the selenium source is at a place with high temperature while the samples are still in a region with low temperature.

The influence of this preheating step on the complete process is quite high. The composition of the resulting layer is closer to the desired composition (see table 4.1) and all solar cell parameters are improved significantly, as one can see in fig. 4.8.

4.3.4 Efficiencies

In fig. 4.9 I - V -characteristics for the best solar cells fabricated with metal salt based precursors are shown. The I - V -characteristics of the gallium-free sample basically show the fact that neither the precursor deposition nor the selenisation process has been optimised for this type of solar cells. The SEM pictures show that the layers are quite inhomogeneous especially in thickness. As a result these cells are dominated by a poor fill factor. Moreover the high vacuum selenisation process is not optimised for these cells. They show less current density even though the composition should be the same. The tube furnace selenisation shows the high potential of this preparation route. Even with very thin absorber layers which (due to the preparation process) have a very low gallium content efficiencies up to 6.4 % are reached.

4.4 Nanoparticles — Doctor Bladed

The preparation of the samples with nanoparticle based precursor layers is described in chapter 3.2.2. Even though highly oxidised commercially available nanoparticles are used solar cells can be produced. As we will see in the following section the selenisation details have an important influence on the success of such a preparation process.

4.4.1 Selenium Partial Pressure at Start of Crystallisation

For precursor layers based on nanoparticles the preheating of the selenium source is even more important. Without the preheating no photovoltaic effect at all can be observed for most samples. Usually the fabricated cells are completely shunted regardless of the way they have been treated prior to selenisation. With the optimised selenisation process typical diode characteristics and the photovoltaic effect can be seen. As soon as the selenisation is adjusted one can as well observe the effect of the treatment prior to the selenisation. The most important one, the effect of the reduction, is explained in the following section.

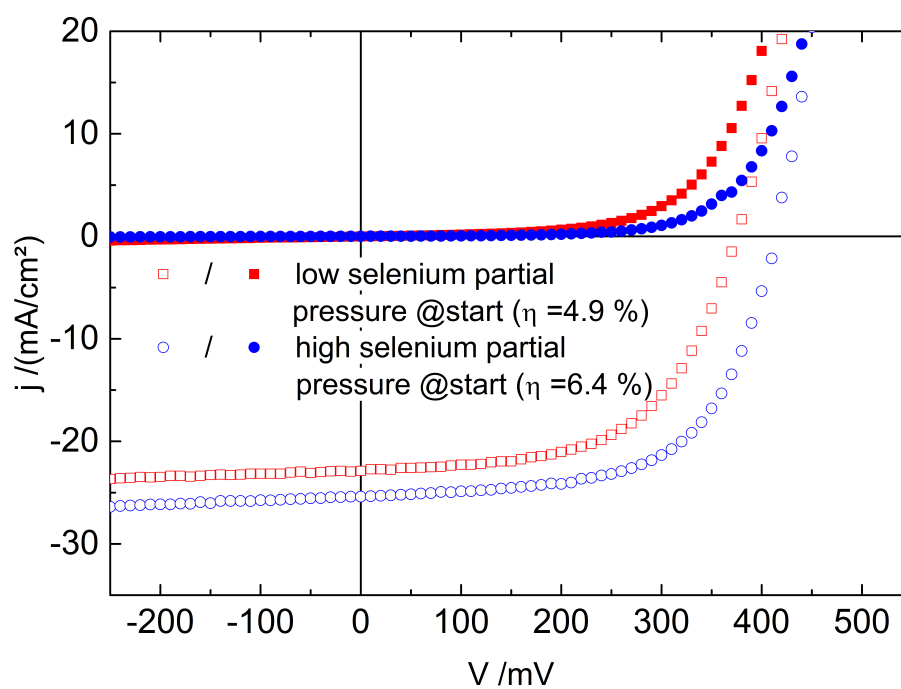


Figure 4.8: I - V - Characteristics of Different Selenisation Processes - Doctor Bladed Precursors.

The partial pressure of selenium at the beginning of the selenisation has a tremendous effect on the performance of the resulting solar cells. All important solar cell parameters are improved significantly by preheating the selenium source.

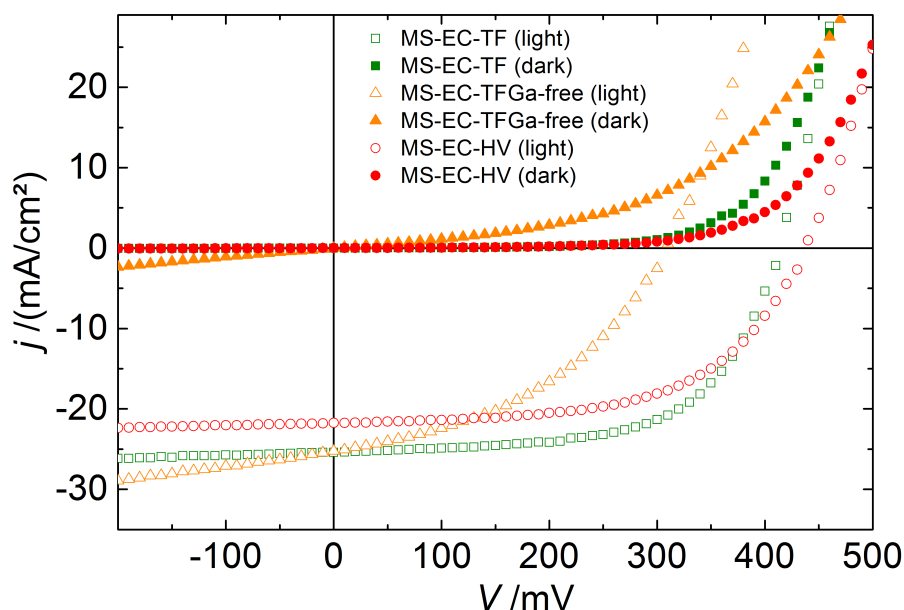


Figure 4.9: I - V - Characteristics of Metall Salt Based Solar Cells.

With all tested preparation routes solar cells could be built. While gallium-free solar cells are dominated by a poor fill factor the gallium containing samples show a high potential for this type of precursors.

4.4.2 Reduction Prior to Selenisation

Untreated precursor layers fabricated with nanoparticles contain a high amount of oxygen which prevents a complete selenisation. Thus a reduction is needed (see chapter 3.2.2). Comparing the selenised films made from reduced and from untreated precursor layers XRD measurements show that after reduction more of the desired CIS phase and less In_2O_3 can be found (see figure 4.10). Furthermore the SEM pictures show a higher degree of selenisation for the precursor layers, which were reduced prior to selenisation. The SEM picture of the untreated sample shows a thin top layer with CIS grains (size about 100 nm) with a small grained porous layer underneath. Other groups observe this double layered structure as well where the lower layer is only poorly reacted [12, 168]. The selenisation process seems to stop at this depth resulting in only a thin CIS layer on top. SIMS measurements back up this model (see publication [19]).

Without a reduction oxides prevent a complete selenisation of the precursor layers. The reduction can happen during ink preparation (accomplished by an additional ingredient) or with hydrogen in a special reduction step after film preparation, prior to selenisation. For the solar cell performance the reduction step is essential. While the untreated precursor layers reach a maximum efficiency of 0.5 % after selenisation a reduction step prior to selenisation helps to accomplish 3.5 % solar cells. More details for the nanoparticle based solar cells can be found

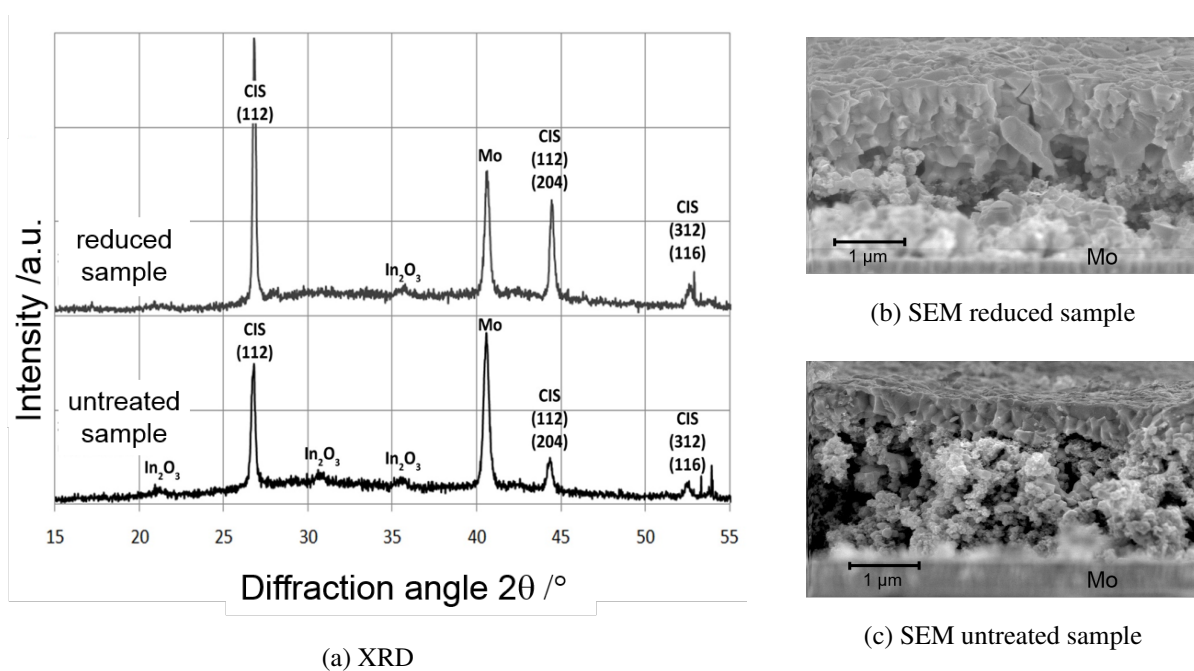


Figure 4.10: XRD and SEM of Selenised Nanoparticle Precursor Layers.

XRD measurements of samples after selenisation show that with a reduction step more of the desired CIS phase and less In₂O₃ can be found. The SEM pictures show a higher degree of selenisation for the reduced precursor layers than for the untreated ones.

in [220].

In summary we used commercially available nanoparticles in a low-cost deposition process and selenised these layers in a tube furnace. The selenisation process had to be adjusted for the nanoparticle based precursors and the layers needed an additional reduction. With these measures efficiencies up to 3.5 % could be reached.

4.5 Vacuum-Based Reference Process — Sputtered

Even though the main focus is laid on non-vacuum methods it is important to be able to compare the obtained results with conventional vacuum-based methods. Therefore a sputter process from an alloy target has been developed to provide reference precursors (see 3.2.3). These layers are selenised both with vacuum-based and non-vacuum methods. Although they are meant as a reference for the printed precursors they show some distinct properties. Thus the optimal process parameters for sputtered precursors are in general different to the ones optimally used for printed precursor layers. In the following section some of those distinct characteristics are discussed.

4.5.1 Selenium Partial Pressure at Start of Crystallisation

By comparing selenisations with a preheated selenium source to selenisations without preheating we find that for all considered precursors the selenisation with a preheated selenium source is advantageous. With sputtered precursors we obtain working cells for shorter selenisation durations with the improved selenisation. We can also see a strong increase in maximum efficiencies for these precursors. Solar cell parameters (especially the open circuit voltage) are positively influenced by a preheated selenium source (see fig. 4.11).

4.5.2 Influence of Selenisation Duration

As described in the previous section two types of selenisation processes were used — one with a simultaneous heating of both the selenium source and the samples and one where the selenium source is preheated and the heating of the samples starts with a time delay. For these two types of processes the influence of the selenisation duration on the sputtered precursors is quite different. Therefore it is discussed separately. The general definition of the selenisation duration is given in section 4.2.2.

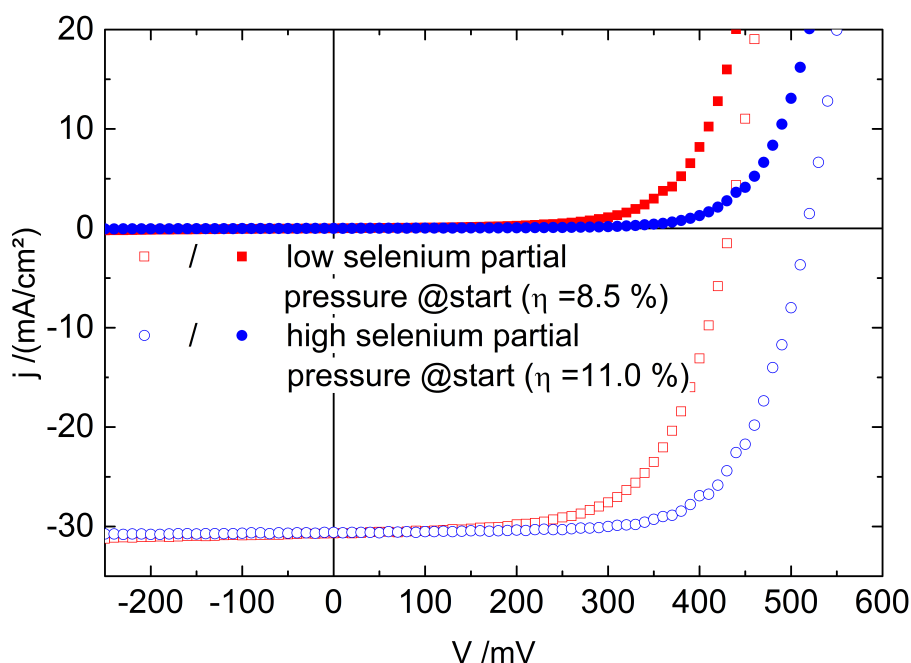


Figure 4.11: I - V - Characteristics of Different Selenisation Processes — Sputtered Precursors.

The preheating of the selenium source has a positive effect on the performance of the resulting solar cells. Especially the open circuit voltage is improved significantly.

Low Selenium Partial Pressure at the Beginning of Selenisation

Without the preheating step the selenium partial pressure is low at the beginning of the selenisation. With this low partial pressure short durations of selenisation lead to shunted cells. For longer durations a change takes place and a photovoltaic response can be observed. For durations of 60 min quite good cells are fabricated. We assume that it can be explained by a selenium deficiency during the heating phase and the beginning of the process. However, it does not affect the crystallinity (as seen in XRD-measurements) nor the chemical composition of the cells after the selenisation.

In general we can say that the selenisation duration has a strong effect for processes without preheating of the selenium source.

High Selenium Partial Pressure at Beginning of Selenisation

For the optimised procedure of selenisation with a preheated selenium source the influence of the selenisation time is analysed in more detail (see [222]). Selenium and gallium gradients and the crystal phases have been analysed.

SIMS measurements were performed on samples selenised for 12, 25, 40, and 60 min. By monitoring the ratio of selenium to metals (SCGI) one can see how far the selenisation reaches (see figure 4.12). For a selenisation duration of 12 min the selenium does not reach the molybdenum back contact. The SCGI is below 1 for most of the absorber layer. The selenisation is not complete yet. After 25 min the precursor is completely selenised. The selenium has reached the back contact, the metals of the precursor layer have reacted with the selenium. The SCGI is 1 for the complete absorber layer. Only after 40 min a molybdenum selenide layer is formed at the back contact, this layer is observed for the 60 min samples as well and can be identified by the SCGI above 1. This selenide layer is important for the operation of the completed solar cell and its formation is studied in the following chapters.

Moreover the ratio of gallium to gallium and indium (GGI) profile changes with selenisation duration (see fig. 4.13). For short durations when the selenisation is not complete the GGI profile is not much changed compared to the precursor layers. When the selenisation process is complete the GGI profile shows the typical gallium gradient which can be found for sequential processes. For 25 min this gradient is too strong, longer selenisation durations can even out this strong gradient. With samples selenised for 90 min (taken from another series of selenisations) this can particularly clearly be seen.

XRD measurements show similar results for the selenisation processes with various selenisation times [222]. After 7 min beside copper indium alloys a CIGS phase can be found. Furthermore a peak related to $\text{Cu}(\text{In,Ga})_3\text{Se}_5$ is observable. After 25 min no critical metallic phases can be detected anymore. For this optimised selenisation procedure the same duration of 60 min results in the best efficiencies. The reason for this is presumably related to a less pronounced gallium gradient.

4.5.3 Efficiencies

For sputtered precursors the tube furnace selenisation leads to the best results as well (see fig. 4.14). The selenisation in the high vacuum chamber (see chapter 4.2.4) leads to much poorer efficiencies which are mainly caused by a lower open circuit voltage and a lower fill factor. Since the adhesion of the selenised absorbers is quite poor in addition, one possible explanation is a too strong selenisation of the molybdenum layer underneath leading to high series resistances and poor adhesion. While the HV samples do not exceed an efficiency of 5.6 % the samples selenised vacuum-free in the tube furnace reached efficiencies as high as 13.7 %. This is a very promising result for such a simple precursor deposition technique and shows the potential of the selenisation process developed here.

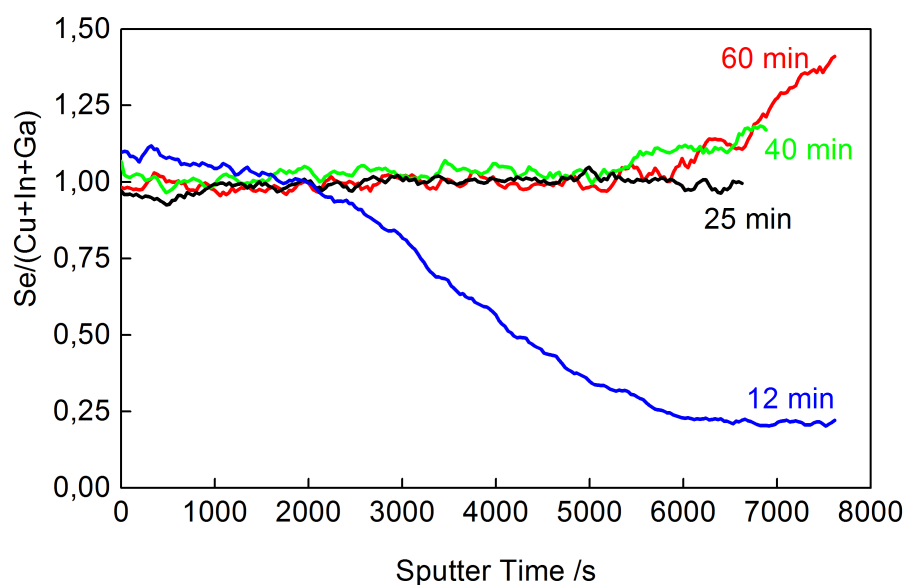


Figure 4.12: Selenium to Metals Ratio Profiles for Selenised Sputtered Precursors.

SIMS measurements show that precursors selenised for 12 min are only selenised in the top part of the precursor. After 25 min the absorber is completely formed and after 40 min the formation of a molybdenum selenide layer starts.

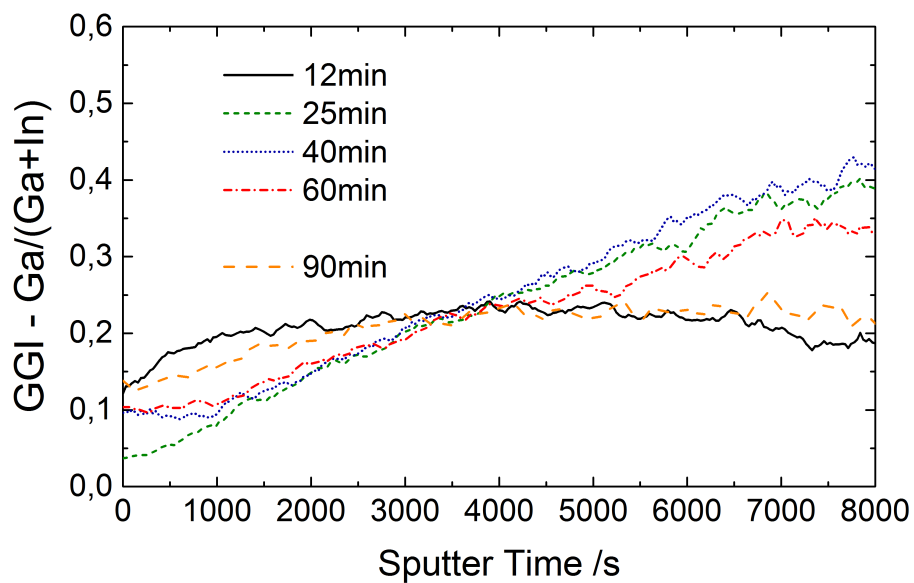


Figure 4.13: Gallium to Gallium and Indium Ratio (GGI) Profiles for Selenised Sputtered Precursors.

During SIMS measurements precursors selenised for 12 min show a GGI profile similar to the precursor layers. Complete selenised layers have the typical strong gallium gradient which gets less pronounced for longer selenisation durations.

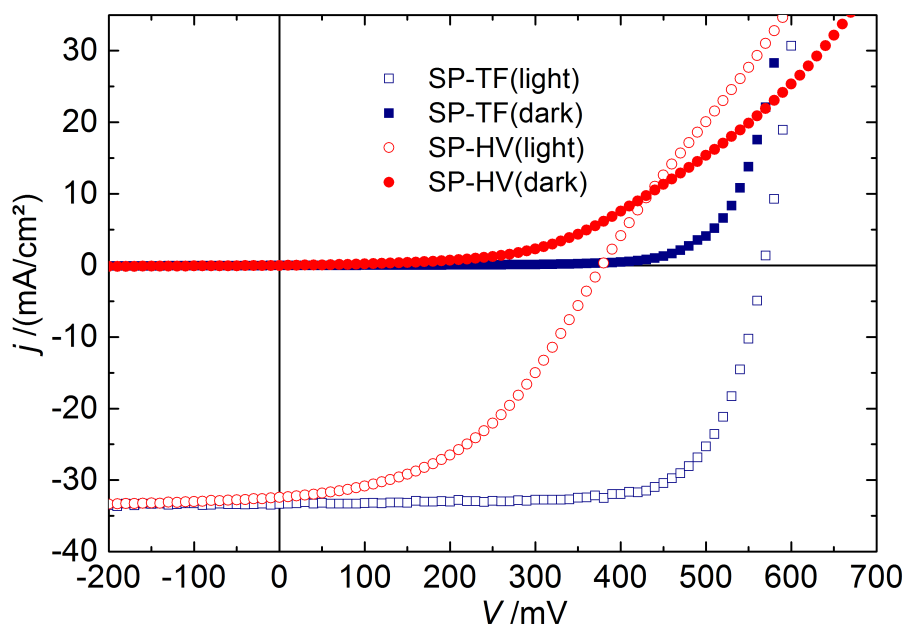


Figure 4.14: I - V - Characteristics of Sputtered Precursors — High Vacuum and Tube Furnace.

The I - V - characteristics show clearly that the selenisation process in the high vacuum chamber is not optimised yet. The tube furnace selenisation yields efficiencies up to 13.7 %.

The sputtered precursors demonstrated their ability to serve as reference samples during the selenisation process in principle. However, it is not possible to optimise the selenisation process with sputtered precursors and use this optimised process for all possible precursor layers. They show a huge potential of the process, but the detailed parameters have to be determined individually for each precursor alternative.

4.6 Conclusion

For the preparation of non-vacuum deposited precursor based solar cells a basic non-vacuum selenisation has been developed. For each type of precursors other factors are optimum. The parameters for the standard selenisation are chosen to yield optimum absorber layers made from non-vacuum precursors.

A long selenisation duration can help to homogenise the gallium gradient which tends to be too steep in sequential processes. Apart from the duration the beginning is an extremely sensitive phase during the selenisation. For functional absorber layers the selenium partial pressure during that phase is decisive. By preheating the selenium source a sufficiently high selenium

supply can be ensured at the beginning of the process.

With such optimised selenisation conditions efficiencies of 6.4 %, 3.5 %, and 13.7 % could be reached for metal salt based, nanoparticle based and sputtered precursors, respectively. The solar cell parameters for selected results can be found in table 4.2.

After understanding what influence factors are most important during selenisation we concentrate on the back contact interface as a next step. The influence of the selenisation on the back contact properties is discussed in the following chapters.

| PARAMETER SAMPLE | V_{oc} /mV | j_{sc} /(mA/cm ²) | FF /% | η /% |
|-----------------------|-----------------|------------------------------------|----------|--------------|
| MS-EC-TF (Ga) | 414 | 25.4 | 61.3 | 6.4 |
| MS-EC-TF (Ga-free) | 308 | 25.2 | 42.7 | 3.3 |
| MS-EC-HV | 437 | 21.7 | 57.7 | 5.5 |
| NP-TF | 295 | 22.8 | 52.7 | 3.5 |
| SP-TF | 568 | 33.3 | 72.4 | 13.7 |
| SP-HV | 378 | 32.4 | 45.3 | 5.6 |

Table 4.2: Solar Cell Parameters of Selected Results.

This table shows the most important solar cell parameters of the best cells for the investigated preparation routes. (MS-EC: metal salt - ethylcellulose, NP: nanoparticles, SP: sputtered, TF: tube furnace selenisation, HV: high-vacuum selenisation)

Chapter 5

Molybdenum Diselenide Formation

In the standard configuration of a chalcopyrite solar cell the back contact interface involves a molybdenum selenide (MoSe_2) layer as a crucial part. In the following chapter the formation of the MoSe_2 itself is discussed. First a short overview is given (5.1). Then the influence of the molybdenum characteristics (5.2) and the selenisation process (5.3) is discussed.

5.1 Overview

An important part of the back contact interface in CIGS solar cells in general is a molybdenum selenide layer. As soon as molybdenum is heated in a selenium atmosphere corrosion of the molybdenum layer takes place and a MoSe_2 layer is formed. MoSe_2 is important for a good contact between back contact and absorber. Even in systems which use another back contact material than molybdenum often a thin layer of MoSe_2 is inserted [250] even though for the optical characteristics of a standard molybdenum back contact the thin layer of MoSe_2 is deteriorating as the combination of molybdenum and molybdenum selenide arrange for a non-reflecting black back contact [115].

The crystal structure of the molybdenum selenide is similar to that of molybdenum sulfide [251]. Fig. 5.1 shows a schematic representation of the structure. It forms triple layers and the orientation of these layers with respect to the substrate is important for its application in chalcopyrite solar cells. More details on the interface and the molybdenum selenide itself can be found in chapter 2.4.2.

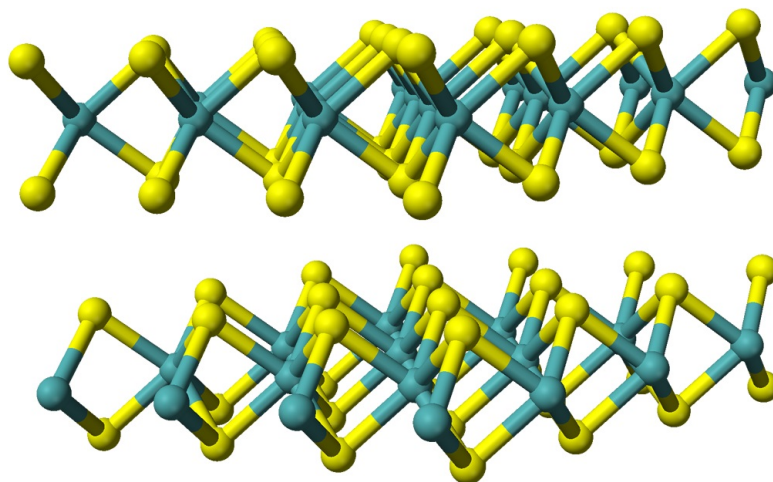


Figure 5.1: Crystal Structure of Molybdenum Selenide.

The crystal structure of molybdenum selenide is similar to that of molybdenum sulfide. It forms triple layers which can have various orientations with respect to the substrate surface.

5.1.1 Studied Parameters for Molybdenum Selenide Formation

Molybdenum Fabrication

For these experiments molybdenum covered glass substrates are fabricated by a single target but several passes. For the fabrication process the sputter power and the sputter pressure are varied. Values for the standard molybdenum process are $2.5 \mu\text{bar}$ for the pressure during sputtering and 6.1 W/cm^2 as the sputter power density. With a carrier velocity of 20 cm/min these parameters yield a layer thickness of around 500 nm molybdenum. In addition to these standard layers samples are fabricated with lower pressure ($1.0 \mu\text{bar}$) and a higher and lower sputter power density (3.0 W/cm^2 and 8.0 W/cm^2 , respectively). To obtain the same thickness for all samples the velocity of the transport carrier is adjusted to the sputtering power. One set of samples is fabricated with standard parameters and additional oxygen as process gas. This helps to understand the influence of oxygen in the molybdenum layer during selenisation.

The structure of the molybdenum film and its texture are strongly influenced by the sputter parameters, mainly the argon pressure and the energy density [252, 253]. Moreover the conductivity is determined by the sputter parameters. With a low argon pressure highly conductive films which show adhesion problems are deposited. With a higher pressure the adhesion is much better, yet the conductivity is poor [253]. Thus often the back contact is built by two (or

even more) layers — a seed layer with good adhesion and a top layer with high conductivity. Another important characteristic of the molybdenum layer is the diffusivity of sodium through the film. It seems to be determined by the sputter parameters as well [254].

Selenisation

The molybdenum films are subsequently selenised with different selenisation processes. Preliminary tests have shown that too little molybdenum selenide is formed with a substrate temperature of approximately 450 °C. Thus all selenisation processes are carried out with a substrate temperature of at least 550 °C.

Standard selenisations are accomplished in a tube furnace which is introduced in section 4.2.1 where details regarding the selenisation process can be found additionally. The investigated parameters are process pressure, the substrate temperature, and selenium source temperature. The standard pressure is 10 mbar, moreover 0.1 mbar, 1 mbar, and 100 mbar are used for these experiments. The standard substrate temperature is 550 °C, it was raised to 600 °C for some runs. The selenium source temperature was 420 °C and 480 °C for the lower substrate temperature and 450 °C for the higher one.

5.1.2 General Remarks about Formation Experiment

In general MoSe₂ was built mostly perpendicular to the substrate — [1,0,0]- and [1,1,0]-orientation. The [0,0,2]-orientation, parallel to the substrate, was hardly found. Exemplarily the selenisation with the strongest selenide formation is shown in figure 5.2. Even for this selenisation the peak at 13.6° corresponding to the [0,0,2]-orientation can not be found. However the peaks at 31.6° and 56.0° (corresponding to [1,0,0] and [1,1,0], respectively) can be clearly seen. In the right picture also a peak for molybdenum can be seen at approximately 59°, the main reflex is located at 41°. As only peaks corresponding to the perpendicular orientation can be seen, mainly these peaks are compared to discuss the influence of various fabrication parameters. The orientation of the molybdenum selenide is important for the integration of the solar cell. It is strongly influenced by the surrounding layers during its formation. Therefore it is not discussed in detail in this chapter, but in the following one (chapter 6).

5.2 Impact of Molybdenum Characteristics

As mentioned above molybdenum layers fabricated with different parameters are selenised in a tube furnace. In the following section the influence of some of these parameters on the selenide formation is discussed.

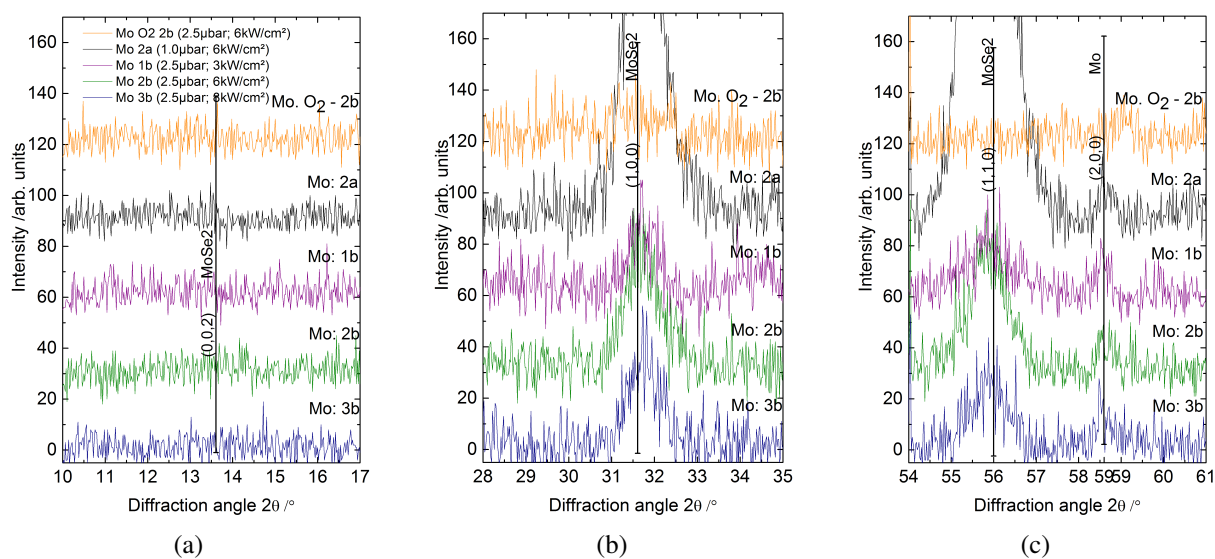


Figure 5.2: XRD Spectra of Selenised Mo Layers Sputtered with Different Parameters.

Even for the selenisation with the strongest selenide formation only MoSe₂ reflexes for the orientation perpendicular to the substrate can be seen (in (b) at 31.6° and (c) at 56.0°). No peaks can be found for the $[0,0,2]$ orientation parallel to the substrate (a) at 13.6° .

Both the thickness of the MoSe₂ layer and its orientation are important for its impact on the solar cell. Thus the influence on both of these properties has to be taken into account. In this chapter mainly the thickness is discussed.

5.2.1 Morphology

Size of Mo Grains — Sputter Power

The sputter power has an influence on the size of the molybdenum grains. In preliminary tests where the molybdenum layer thickness was varied simultaneously this grain size seemed to have an influence on the selenide formation. However, in thorough experiments this assumption could not be verified. For the specific selenisation process the sputter power during molybdenum deposition has negligible influence. Obviously the effect first observed was caused by the varying thickness of the molybdenum.

Density of Layer — Sputter Pressure

The sputter pressure has an influence on the density of the molybdenum layer. The lower the sputter pressure is the more intrinsic compressive stress is in the layer [255–258]. In addition, the layer becomes denser with lower pressure [252, 259].

The lower pressure during sputtering has a clear impact on the molybdenum selenide formation. Molybdenum layers sputtered with a lower process pressure of 1.0 μbar show a much stronger MoSe₂ formation than similarly selenised layers sputtered with the normal pressure of 2.5 μbar (see figure 5.3). The higher stress or the higher density helps the MoSe₂ formation so that it is much stronger for the lower sputter pressure. For the selenisation with lower temperatures (both selenium source and substrate temperature) it is extremely obvious. While with standard sputter parameters only a quite indistinct peak from molybdenum selenide can be observed this peak becomes very pronounced with a lower sputter pressure of only 1.0 μbar.

5.2.2 Chemical Composition

Oxygen Content — Sputter Atmosphere

Usually pure argon gas is used for the sputter atmosphere during the molybdenum deposition. To investigate the influence of oxygen in the layer, some layers have been fabricated with a 20 %-oxygen-in-argon mixture. Jankowski et al. showed, that the oxygen content is higher on top of the deposited layer compared to the bulk [260]. For a fixed oxygen to argon ratio the oxygen content in the deposited layer decreases with increasing sputter power [260], for the used sputter power we can assume a molybdenum to oxygen ratio of well above 2:1.

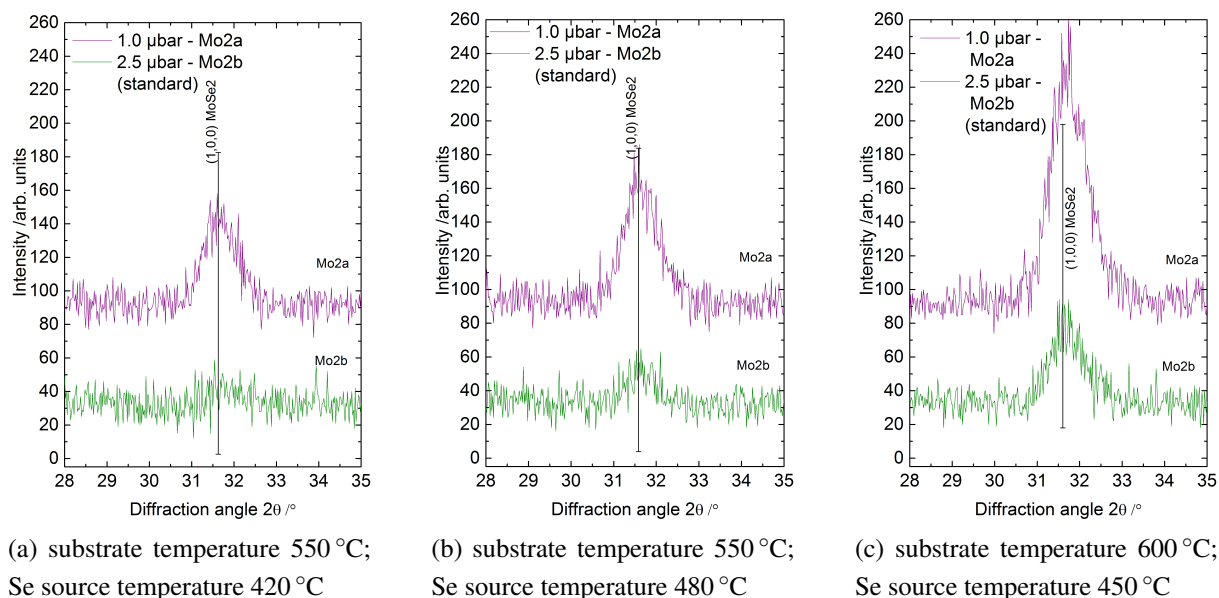


Figure 5.3: XRD Measurements for Selenised Molybdenum Layers Fabricated with Different Sputter Pressure.

Molybdenum layers fabricated with different sputter pressure were selenised under various selenisation conditions (a)-(c).

Oxygen in the molybdenum layer suppresses the selenisation of this layer quite effectively. The XRD measurements show no peaks for all selenisations (see figure 5.4). All other parameters are kept the same during the molybdenum deposition except for the 20% oxygen in the sputter gas. While the standard molybdenum shows a small peak even for the selenisation with a low selenium source temperature, the modified molybdenum layers do not show any signs of molybdenum selenide even for the higher substrate temperature where the standard molybdenum layers show a high peak corresponding to MoSe_2 .

It can be assumed that especially the surface of the molybdenum layer is passivated by an oxide layer. This oxide is not visible in XRD measurements — either because it is too thin or, more probable, it is not crystalline. In any case the oxygen can not be replaced by selenium easily during a process as used here with a very low partial pressure of selenium. Thus no molybdenum selenide formation takes place which is not desirable for the complete device.

In summary the molybdenum characteristics have a strong influence on the molybdenum selenide formation. While the sputter power has no significant influence the sputter pressure affects the selenide formation considerable. The lower the pressure during the molybdenum sputter process is the more pronounced the selenide formation becomes. With oxygen in the

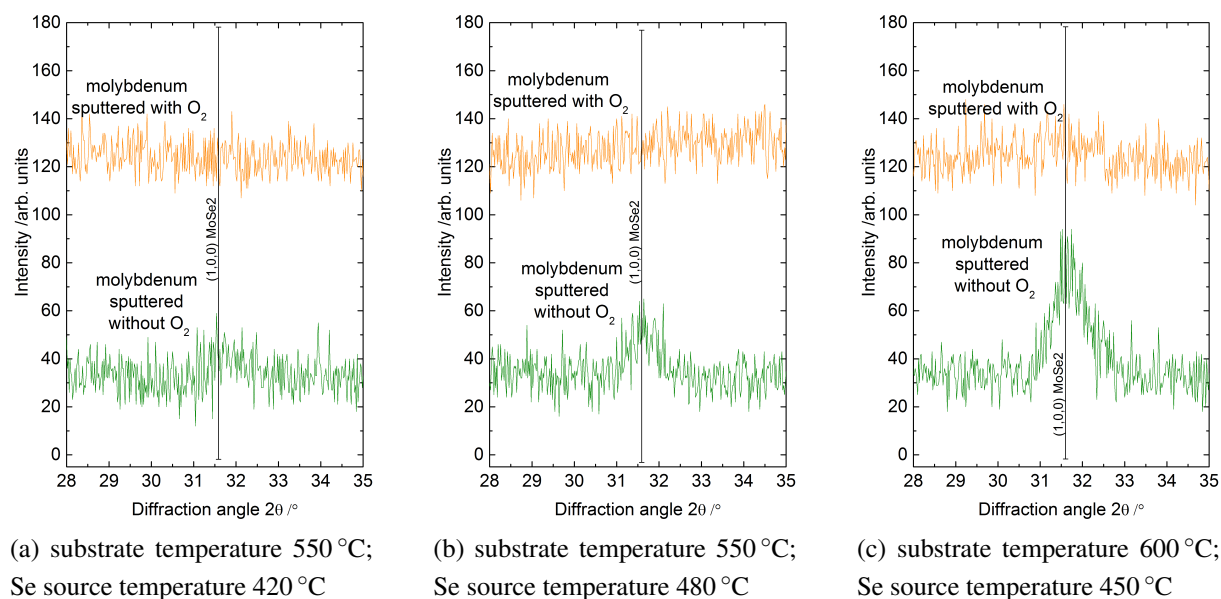


Figure 5.4: XRD Measurements for Selenised Molybdenum Layers Fabricated with Different Sputter Atmosphere.

Molybdenum layers fabricated in argon and argon/oxygen atmosphere were selenised under various selenisation conditions.

sputter process the selenide formation can actually be suppressed.

5.3 Impact of Selenisation

The specific selenisation characteristics are crucial to the molybdenum selenide formation and the properties of the resulting layers (see for example [44]). In the following chapter our selenisation process and its consequences for the selenide formation are investigated. The main parameters pressure and temperatures during selenisation (both source and substrate) are discussed.

5.3.1 Selenium Partial Pressure

The selenium partial pressure is the main factor to influence the selenide formation of molybdenum layers. It can be adjusted by tuning the pressure in the furnace and the selenium source temperature.

Pressure during Selenisation

The parameter accessible easiest during the selenisation process is the pressure in the tube furnace. Its influence is shown here.

For a very low selenisation pressure sometimes the formation of a crystalline oxide phase can be observed. This prevents a selenide formation and can be ascribed to a slight leakage of the tube furnace which is more harmful for such low process pressures, but even if the oxide formation can be prevented by most careful processing, there is hardly any selenide formation for low process pressures observed (see figure 5.5).

For higher selenisation pressures the selenide formation is quite low, too. This holds for higher substrate temperatures as well and is assumed to be related to a lower selenium partial pressure. One drawback of the here described selenisation process is the fact that selenium partial pressure and process pressure can not be adjusted completely independently and the selenium partial pressure can not be measured with the here described set-up.

In summary these measurements show that the process pressure of 10 mbar is the optimum for the selenisation. This value is used as standard pressure for all other selenisations.

Selenium Source Temperature

Temperature is the key parameter in thermodynamics. Even though the selenium source temperature can only be determined indirectly it is an important parameter for the selenisation process. Both the reactivity of selenium and the capacity of the carrier gas to take selenium in vary with temperature. Nonetheless the effect on the molybdenum selenide formation is only small for different selenium source temperatures as can be seen in figure 5.6. It might be the case that the selenium source temperature is still too low and higher temperatures are needed.

5.3.2 Substrate Temperature

Apart from the selenium partial pressure also the substrate temperature has an impact on the resulting selenide layer. It even has a much stronger influence on the selenide formation than the source temperature. In preliminary experiments we could see that a substrate temperature of 450 °C is not sufficient to build any molybdenum selenide. Thus for the main experiments 550 °C and 600 °C are used. The higher the substrate temperature is the more selenide is formed (see figure 5.6). This holds for all different molybdenum layers. Here the molybdenum fabricated with standard parameters is shown.

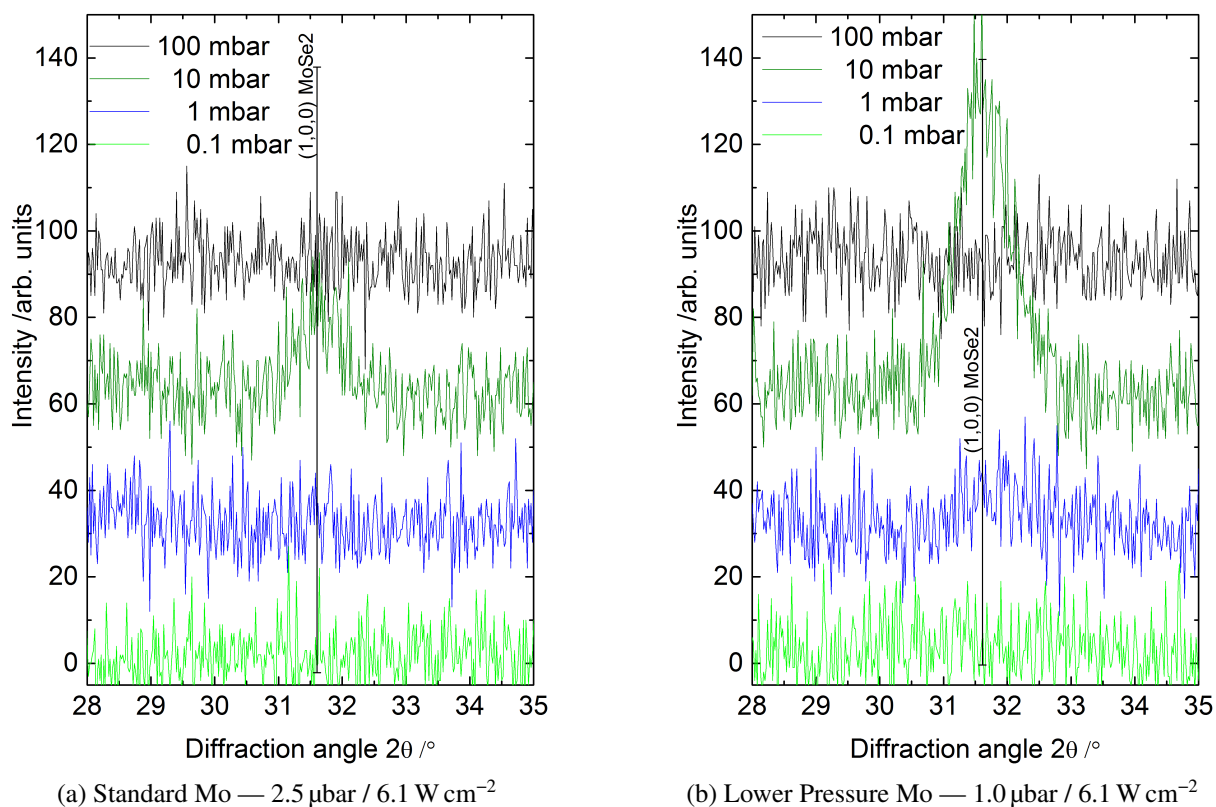


Figure 5.5: XRD Spectra for Different Selenisation Pressure and Different Sputter Pressure.

The selenisation pressure has a strong influence on the molybdenum selenide formation both for standard molybdenum (a) and for molybdenum fabricated with a lower sputter pressure (b). For 10 mbar the peak is the highest and both for higher pressure (100 mbar) and lower pressure (1 mbar/0.1 mbar) the peaks are much smaller or not detectable anymore.

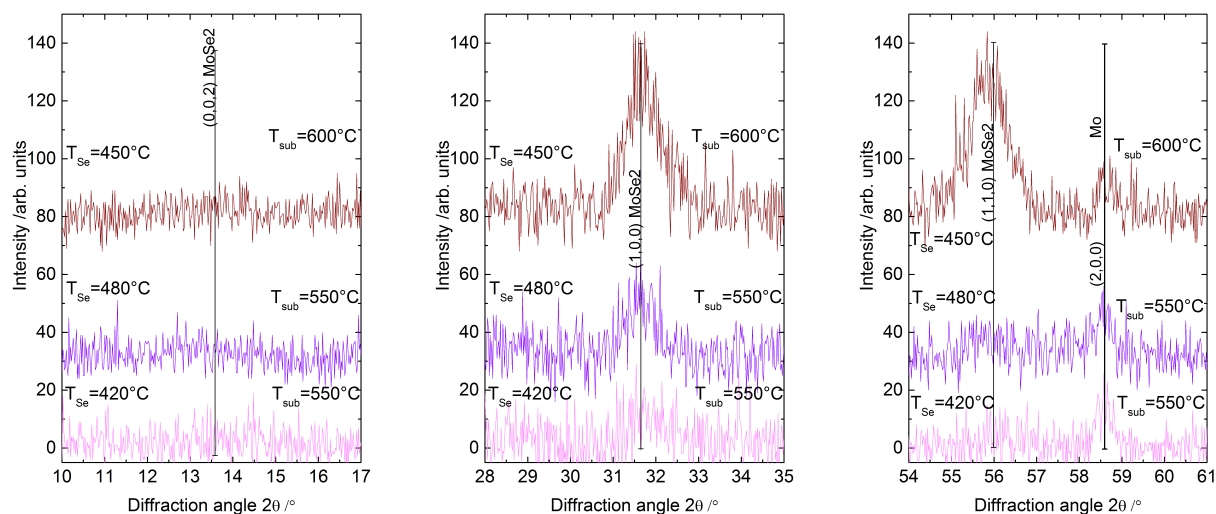


Figure 5.6: XRD Measurements for Selenised Molybdenum Layers Selenised at Different Selenisation Temperatures.

Comparing molybdenum layers selenised at different temperatures one sees that the substrate temperature has the strongest influence whereas the source temperature has only a minor effect.

5.4 Summary

In the last part of this chapter the impact of the specific selenisation conditions on the molybdenum selenide formation has been shown. For the best selenisation partial pressure a process pressure of 10 mbar has been identified as the optimum. Regarding the selenisation temperatures it could be seen that the source temperature during the process itself has only minor effect whereas the substrate temperature offers a sensitive parameter to determine the strength of the selenide formation.

For the selenisation of molybdenum layers we can sum up that both the fabrication and the selenisation parameters offer the possibility to influence the selenide formation. For the molybdenum properties the density of the layer (influenced by the pressure) and the chemical composition (oxygen content – determined by the atmosphere during sputtering) have a stronger effect than the size of the molybdenum grains (influenced by the sputter power). For the selenisation process the substrate temperature offers the most sensible parameter to influence the selenide formation.

Chapter 6

Back Contact Interface — Mo/CIGS

The formation of the important molybdenum selenide layer at the back contact interface is influenced by the adjacent layers during a sequential fabrication process. Additionally to the molybdenum fabrication and the selenisation process the precursor layers have an influence on the molybdenum selenide layer.

After a short overview (6.1) the influence of the precursors is presented (6.2). Then the selenisation and its consequences for the molybdenum selenide layers is discussed (6.3).

6.1 Overview

MoSe₂ growth is influenced not only by the molybdenum fabrication parameters and the selenisation conditions but also by other layers deposited on top of the molybdenum. For sequential processes precursor layers cover the molybdenum before it gets into contact with selenium. For the coevaporation process it is observed that MoSe₂ only develops after the first stage when indium and gallium are evaporated and the temperature is raised to a higher level. Nishiwaki et al. suggest that it does not form under Cu-rich conditions but is produced during In-/Ga-rich condition of the second stage [99]. In any case the formation and even the orientation of the MoSe₂ is influenced by possible layers covering the molybdenum [44].

6.1.1 Studied Parameters for Molybdenum Selenide Formation

Molybdenum Fabrication

Since the experiments described in chapter 5 showed that a lower sputter pressure during the fabrication of molybdenum enhances the MoSe₂ formation, the lower sputter pressure of 1.0 μbar is used as the common pressure for these experiments. Again the sputter power density is varied for some of the runs (6.1 W/cm² as the standard value and 3.0 W/cm² and 8.0 W/cm² as lower and higher power density, respectively) and the velocity of the transport carrier is adjusted to the

sputtering power to obtain the same thickness for all samples. Still the standard set of process parameters is used for a reference process (2.5 μbar and 6.1 W/cm^2).

Selenisation

The molybdenum films and the overlying precursor layers are subsequently selenised with different selenisation processes.

Standard selenisations are accomplished in a tube furnace which is introduced in section 4.2.1. The investigated parameter for these experiments is the selenisation source temperature. Due to process limitation the substrate temperature has to be at 550 °C. For uncoated molybdenum layers the variation of the source temperature has had no significant effect. For the here described processes the source temperature is raised to higher levels to study the influence on the selenide formation with covering precursor layers on top of the molybdenum.

The standard pressure is 10 mbar and the standard substrate temperature is 550 °C. The selenium source temperature was 475 °C, 500 °C and 515 °C .

For comparison reasons a selenisation run was conducted in a conventional high vacuum chamber which is introduced in section 4.2.4.

6.2 Influence of Precursor

6.2.1 Sputtered Precursors

Since the selenide formation is less intense with a precursor layer on top of the molybdenum, figure 6.1 shows the diffraction pattern for the selenisation with the strongest molybdenum selenisation. In contrast to the experiments without any precursor layer one can see a clear peak for the selenide layer orientation parallel to the substrate, that means the c-axis perpendicular to the substrate, regardless of molybdenum fabrication parameters. In literature it is clear that the orientation of molybdenum selenide depends on both the selenisation conditions and the interface type. However, often the perpendicular orientation (that means c-axis parallel) is preferred for the selenisation of bare molybdenum and the parallel orientation seems to be the preferential one for the molybdenum / CIGS interface [98, 99, 107]. In the here described process sodium comes from the glass substrate and is not further controlled. Abou-Ras et al. showed a strong influence of sodium on the strength of the selenisation of molybdenum [107]. This might explain the difference to other processes where sodium is often supplied by sodium fluoride layers.

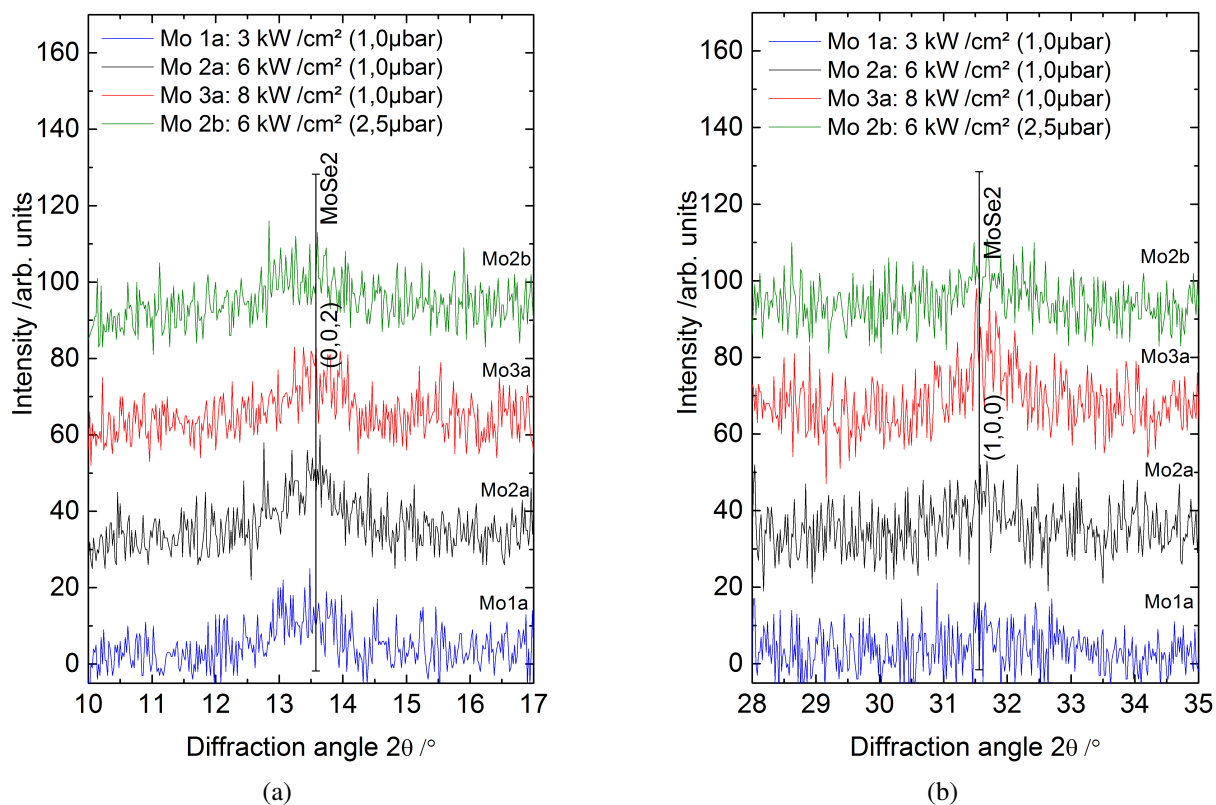


Figure 6.1: XRD Spectra of Selenized Mo under Sputtered CIG for Different Mo Sputter Parameters.

For the selenisation with the strongest MoSe₂ formation both orientations of selenide layers (parallel - around 13.6 (a) and perpendicular - around 31.6 (b)) can be seen for all various molybdenum fabrication parameters. The peak corresponding to parallel orientation is mostly more pronounced regardless of the molybdenum fabrication parameters.

For our selenisation process the parallel orientation of the selenide layers occurs only with precursor layers while the perpendicular orientation can be seen for both types of the interface. Nevertheless the adhesion of the absorber layers is not deteriorated and the electrical performance is not influenced.

6.2.2 Metal Salt Precursors

For doctor bladed precursor layers no peaks at all can be seen. Neither the peak corresponding to parallel orientation nor the one to perpendicular orientation can be seen (see figure 6.2). This holds for all various molybdenum fabrication parameters and all selenisation parameters. Obviously, the carbon layer between CIGS and molybdenum prevents the molybdenum selenide formation effectively. The carbon layer seems to provide an ohmic contact between molybdenum and absorber which the molybdenum selenide usually offers.

For the different precursors a clear difference in molybdenum selenide formation can be seen. While there is a pronounced formation for sputtered precursor layers no selenide can be seen for printed precursor layers. For these layers the carbon layer seems to act as a substitute for the selenide layer which usually is needed for a good contact.

6.3 Influence Selenisation Parameters

In order to study the influence of the selenisation process parameters on the molybdenum selenide formation both the pressure and the temperature for the selenisation process have been varied. Both selenisation setups — the tube furnace and the conventional evaporation chapter are used for these experiments. The details to these processes can be found in chapter 4.

6.3.1 Selenisation Pressure

The pressure in the evaporation chamber is 1×10^{-6} mbar. The maximum substrate temperature is about 570 °C and the selenium source has a temperature of about 350 °C (see chapter 4.2.4). With this selenium source temperature a higher partial pressure should be reached than in normal tube furnace experiments where the pressure is 10 mbar. The temperature in the tube furnace is varied in the different experiments (see following section).

As already mentioned in the previous section the samples with printed precursors showed no molybdenum selenide formation for both selenisation setups. After the selenisation in the vacuum chamber for sputtered precursors no peaks could be found corresponding to the perpendicular orientation (see figure 6.3b). Yet for some molybdenum fabrication parameters the peak

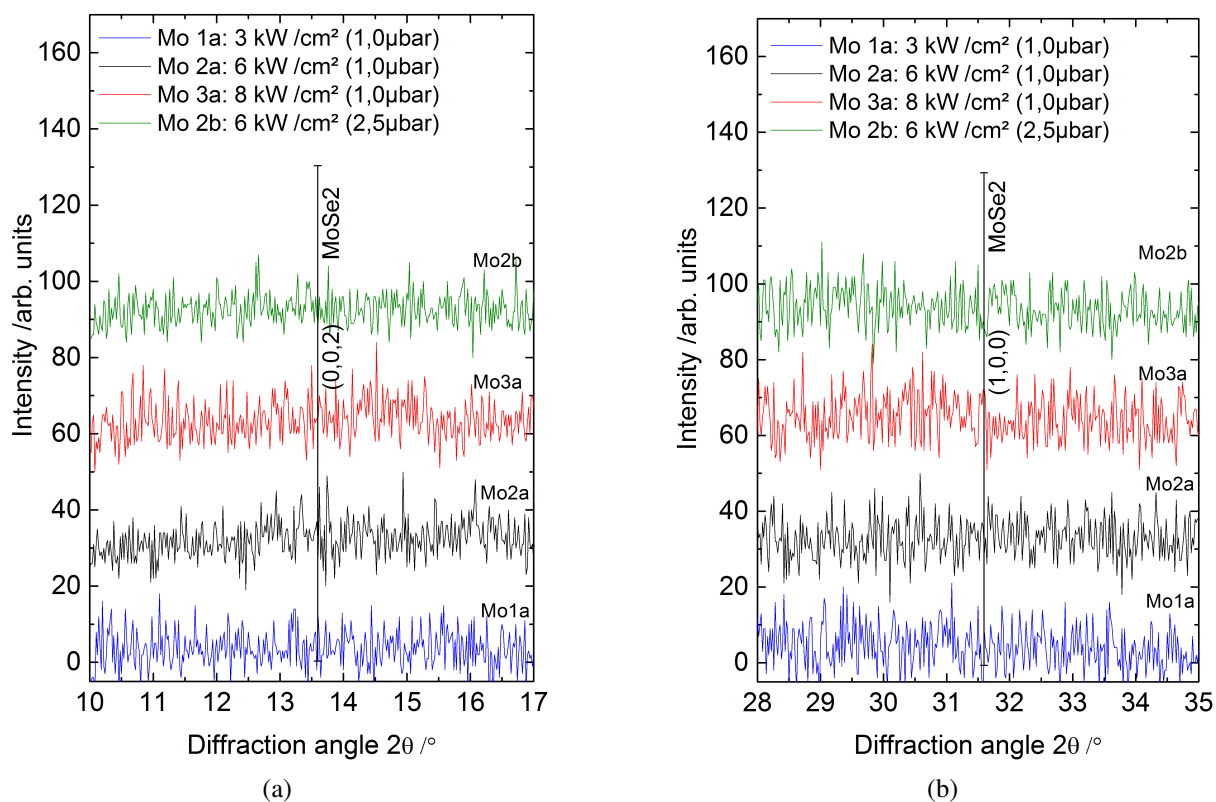


Figure 6.2: XRD Spectra of Selenized Mo under Doctor Bladed Precursor for Different Mo Sputter Parameters.

Even for the selenisation with the strongest MoSe₂ formation neither the peak corresponding to parallel orientation (a) nor the one to perpendicular orientation (b) can be seen for all various molybdenum fabrication parameters. The carbon layer between CIGS and molybdenum prevents the molybdenum selenide formation effectively.

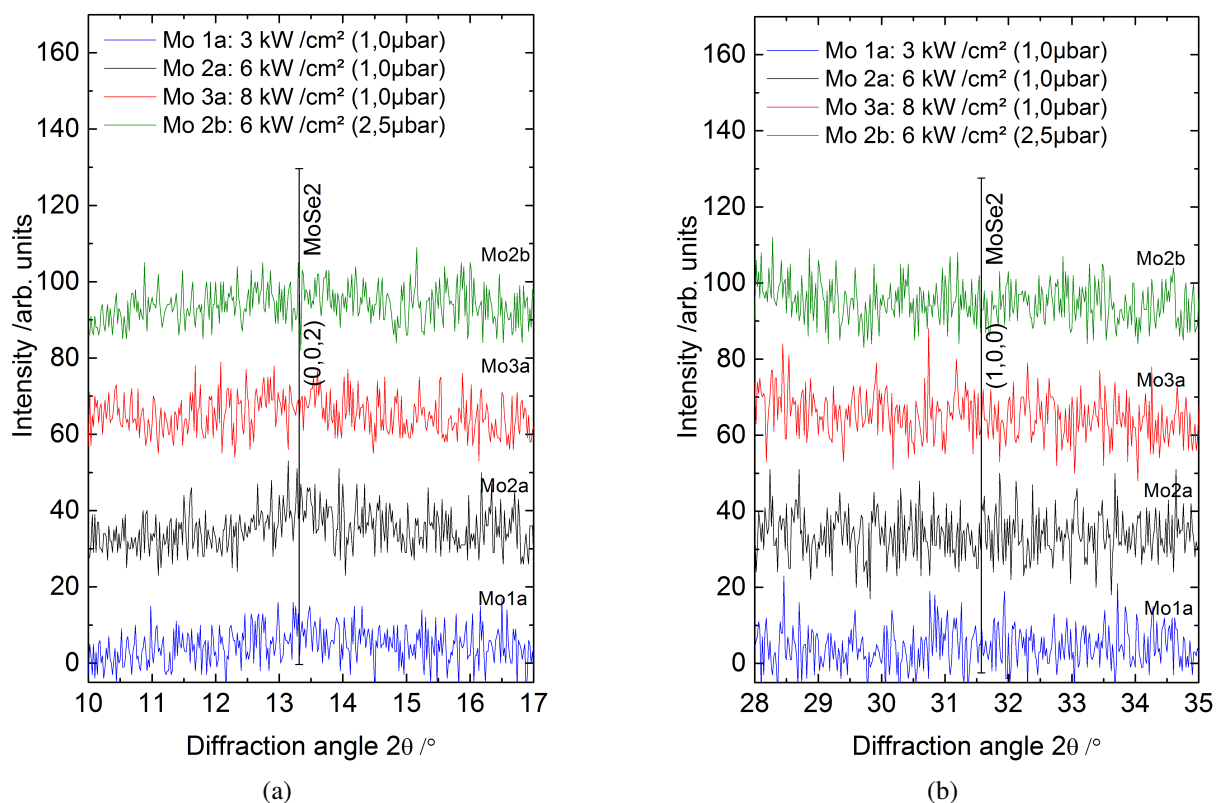


Figure 6.3: XRD Spectra of MoSe₂ — Sputtered Precursors Selenised in Vacuum.

For selenisations in vacuum only peaks corresponding to parallel orientation (a) can be seen while no peaks corresponding to perpendicular orientation (b) can be seen for all various molybdenum fabrication parameters. This may account for the poor adhesion of CIGS layers fabricated in the vacuum chamber.

corresponding to the parallel orientation can be seen (see figure 6.3a). This might explain why the adhesion is quite poor for samples selenised in the vacuum chamber.

After the selenisation in the tube furnace more molybdenum selenide can be seen in the XRD measurements. Depending on the molybdenum layer fabrication parameters and the selenisation temperature the orientation and the amount of molybdenum selenide varies. But in general it is more than for the selenisation in high vacuum.

After selenisation in the vacuum chamber both for printed and sputtered precursors hardly any peaks can be found. Maybe walls and other cold parts of the vacuum chamber decrease the selenium partial pressure at the samples too much so that it is lower than in the tube furnace. In chapter 4 we see that the efficiencies of solar cells made of sputtered precursors are lower for absorbers selenised in the vacuum chamber compared to absorbers selenised in the tube furnace. So obviously the selenisation is not optimised for this kind of precursors. Since the vacuum based selenisation is not the main focus of this thesis, no further optimisation is done for this process.

6.3.2 Selenisation Temperature

In the following section experiments with different selenium source temperatures (475 °C, 500 °C and 515 °C) are discussed. For all molybdenum fabrication parameter sets the higher selenium source temperature leads to more selenide formation as can be seen in figure 6.4. For the standard molybdenum (2.5 μbar and 6.1 W/cm²) the ratio between perpendicular and parallel orientation gets better with higher selenium source temperature. This effect is less pronounced for the samples fabricated at lower sputter pressure (1.0 μbar , see figure 6.4c and 6.4d). Here the high source temperature might lead to adhesion problems. In order to avoid these problems for processes with molybdenum layers sputtered at lower pressure a slightly lower selenium source temperature is recommended.

It can be seen that a higher selenium source temperature is preferable for the standard types of molybdenum. Especially for a good adhesion the higher temperature is important. Together with the fact that it gives a higher selenium partial pressure it seems to be optimal for the selenium source to have a high temperature during the process. For these high temperature processes it is important to have enough selenium since it evaporates much faster. Nonetheless for the molybdenum layers sputtered at lower pressure (1.0 μbar) the highest selenium source temperature gives a less favourable ratio of the two orientations of molybdenum selenide and thus a slightly lower temperature is preferable.

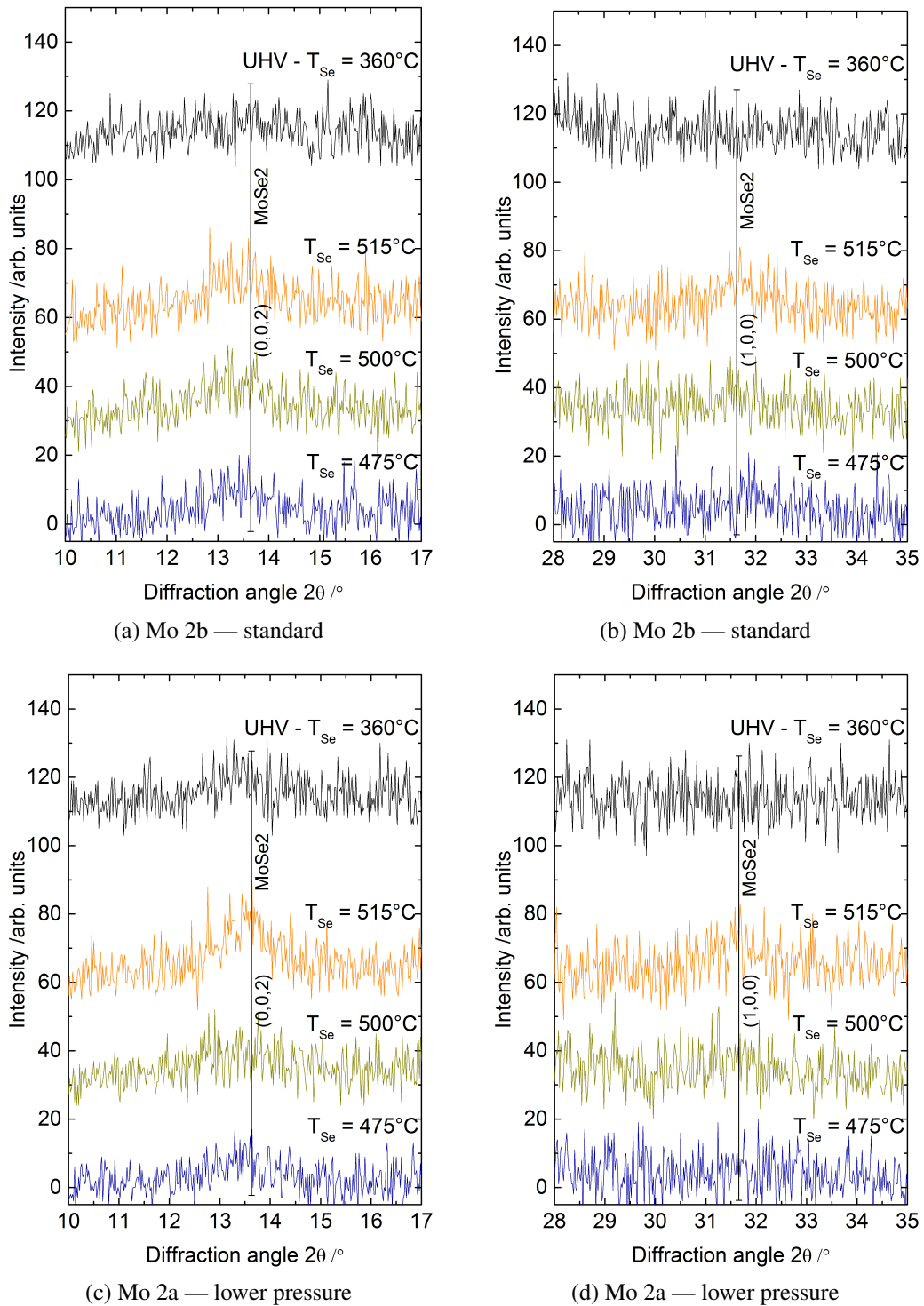


Figure 6.4: XRD Spectra of MoSe₂ — Sputtered Precursors.

In these XRD spectra the MoSe₂ peaks both for standard molybdenum and for layers sputtered at lower pressure can be seen.

6.4 Summary

In this chapter we have seen that both the formation and the orientation of the formed molybdenum selenide are dependent on the precursor layer deposition and the selenisation parameters.

For the selenisation in vacuum hardly any selenide can be found for both investigated precursor types. In the tube furnace a high selenium source temperature is best for sputtered precursors on standard molybdenum. The carbon layer of the doctor bladed metal salt samples prevents molybdenum selenide formation effectively during the selenisation in the tube furnace. Nonetheless these solar cells show acceptable efficiencies (especially when their low thickness is taken into account). The next chapter deals with this topic and studies the influence of said carbon layer.

Chapter 7

Back Contact Interface with Additional Carbon Layer — Mo/C/CIGS

In the following chapter the influence of an additional carbon layer on the back contact interface is discussed: After a short motivation why additional carbon layers are an interesting research topic (see section 7.1.1) the need for reference samples and their properties are discussed (see section 7.1.2). With the analysis of the carbon layer the introduction is concluded (see section 7.1.3). In the sections thereafter the thickness both of the additional carbon layer (see section 7.2) and of the absorbing CIGS layer (see section 7.3) are altered and results given. After identifying and discussing possible explanations for the results (see section 7.4) the chapter finishes with the presentation of some simulations to back up the conclusions drawn before (see section 7.5).

7.1 Introduction

7.1.1 Motivation

As shown in section 4.3, CIGS layers fabricated with printed precursors from metal salts and ethyl cellulose solutions are usually very thin (sometimes only ≈ 250 nm). Nonetheless they show quite high current densities and good efficiencies given such thin layer thicknesses. Efficiencies over 6 % could be achieved in-house and other groups even reached higher efficiencies up to 6.7 % [18] with layers only slightly thicker and vacuum-free methods. All this is even more surprising when thinking about the residual carbon layer between the CIGS-layer and the molybdenum back contact. Yet even compared to vacuum-based methods with similar layer thicknesses these solar cells show good efficiencies.

It has not been understood why such efficiencies could be reached with non-vacuum methods and an additional carbon layer. The influence of this carbon layer has not been studied yet,

but it was mostly thought to be detrimental for the solar cell.

In order to investigate the influence of a carbon layer on solar cells with thin CIGS-absorber layers these typical carbon layers are fabricated separately (see figure 7.1). To achieve this a

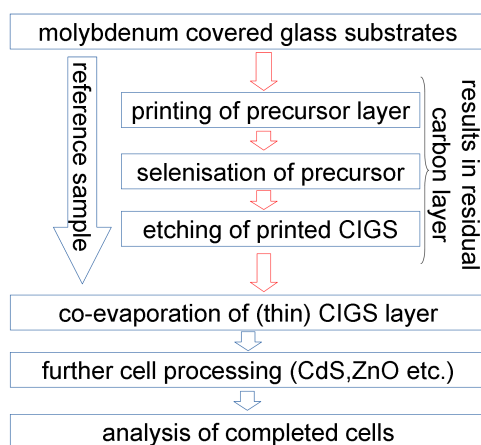


Figure 7.1: Fabrication Flow Chart of Samples with Additional Carbon Layer.

This flow chart shows the sequence of sample preparation for both the reference samples and the samples with the additional carbon layer [261].

printed CIGS-layer is fabricated by the blading of a metal salt solution with ethyl cellulose as a binder material and a subsequent selenisation step in the tube furnace. This printed CIGS-layer is then etched away with a combination of methanol and bromine leaving behind only the desired carbon layers. On these carbon layers thin CIGS-layers were evaporated with the conventional vacuum-based co-evaporation process established at ZSW.

7.1.2 Reference Samples

To study the influence of an additional carbon layer CIGS layers were fabricated by co-evaporation both directly on molybdenum and on the additional carbon layer (see previous section and figure 7.1). In each CIGS-layer evaporation process five to eight reference samples with absorbers directly on molybdenum were fabricated (see figure 7.2). Then, for the general investigation of the influence of a carbon layer on the potentially achievable efficiency, the maximum efficiency value for each substrate is determined and used for comparison. Figure 7.3 shows the average values of these maximum efficiencies per reference sample and the corresponding standard deviations.

It can clearly be seen that the efficiency of the solar cell rises with increasing absorber thickness. This finding is in accordance with studies and simulations by other groups [262–266] and can be explained by the fact that a smaller amount of light is absorbed in these layers with

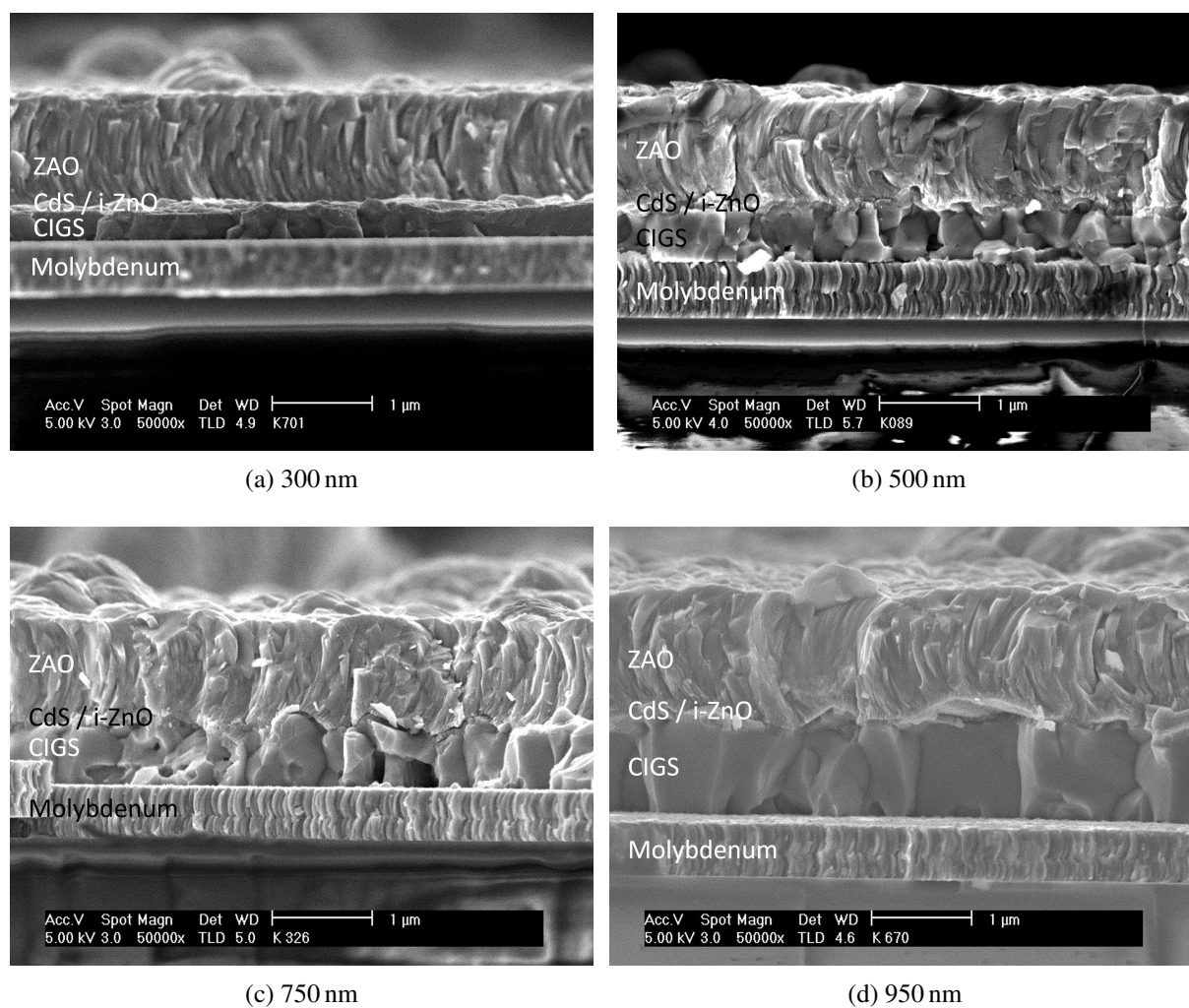


Figure 7.2: CIGS References With Various Layer Thicknesses.

SEM-images of exemplary reference samples are shown. The stated thicknesses represent an average of all reference samples fabricated in the respective batch.

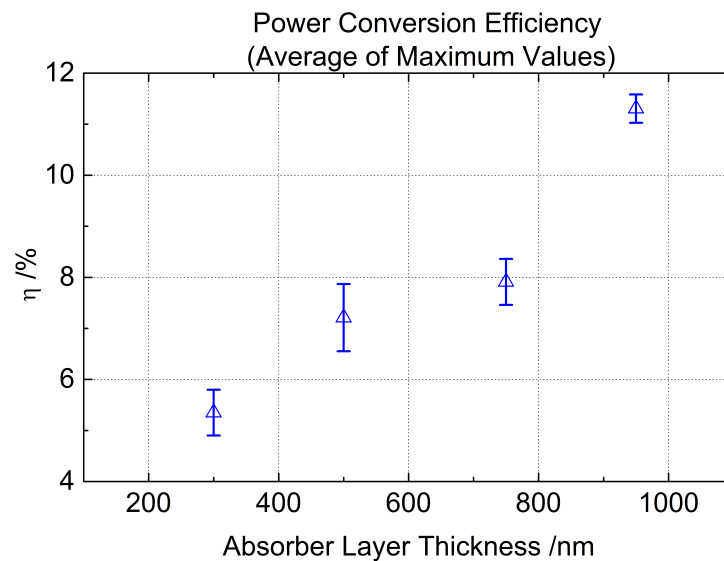


Figure 7.3: Average of Maximum Efficiencies for Each Reference Sample.

The maximum efficiency per substrate is identified. The average of these maximum values is plotted with its corresponding standard deviation over absorber layer thickness.

decreasing thickness. Less absorption lowers the short circuit current of the fabricated solar cells (see figure 7.4b). For very thin layers the interface between absorber and back contact has an increasing influence and back contact recombination plays a significant role. These recombination losses are explained in section 2.2.2. Additionally the film quality is poorer for thinner layers due to fabrication reasons (see section 2.5) and the grain size in general is smaller. All this lowers the open circuit voltage for very thin layers (see figure 7.4a).

For the best reference cells of each absorber thickness the I - V characteristics can be seen in figure 7.5. When comparing these high efficiency cells to each other it is even more obvious that V_{oc} can be about the same for a wide range of absorber thicknesses. While V_{oc} does not show a sharp drop until very thin layers the j_{sc} already drops for the thicker layers. This shows that the incomplete absorption plays an important role even for the thicker layers under examination.

So the results of these best-in-class cells are in good agreement with simulations assuming a constant carrier lifetime whereas the average values (see figure 7.4) show better agreement with simulations assuming a carrier lifetime varying with thickness [265].

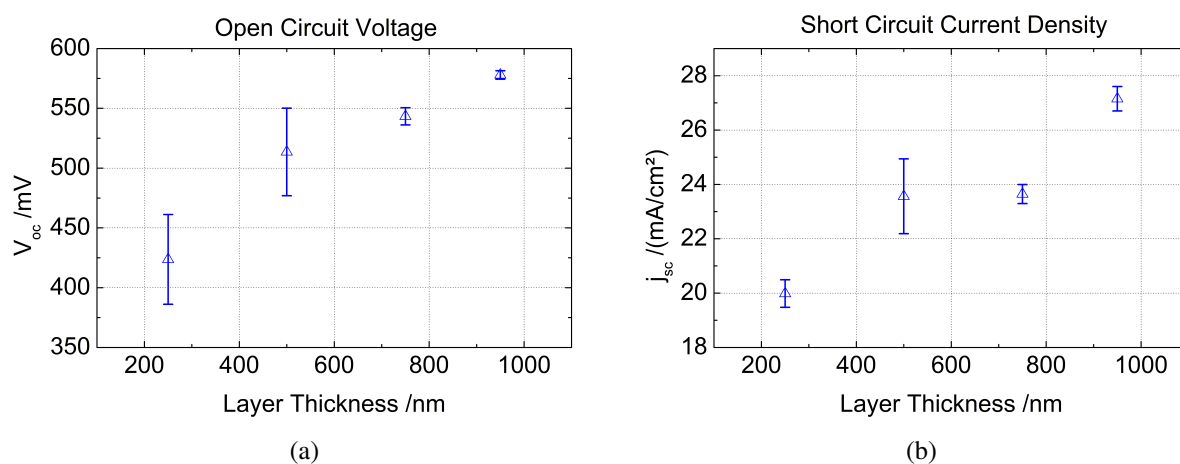


Figure 7.4: j_{sc} and V_{oc} of Reference Samples With Different CIGS Thicknesses. The average values of j_{sc} (a) and V_{oc} (b) for the most efficient cells per substrate decrease with decreasing absorber thickness.

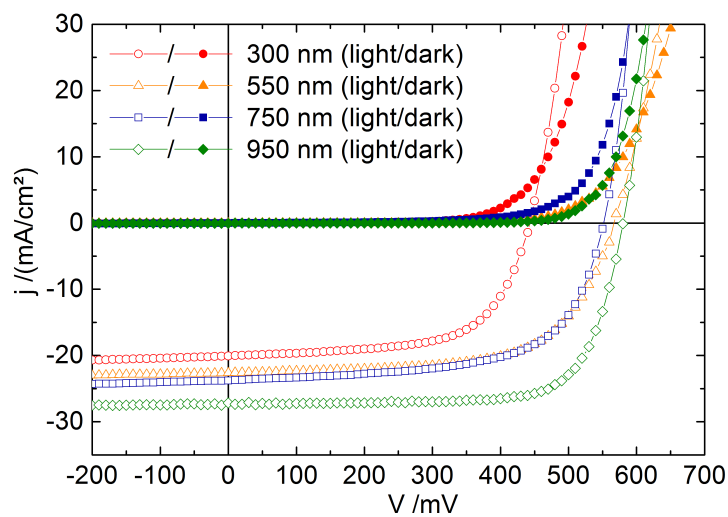


Figure 7.5: I - V Characteristics for Reference Samples. For each layer thickness I - V characteristics for the cell with best efficiency is shown. It can be clearly seen that both open circuit voltage and short circuit current density are increasing with increasing thickness.

7.1.3 Analysis of Carbon Layer

In the following the carbon layer is examined in detail before investigating its effect on the working of a complete cell. Most layers are fabricated with gallium containing precursors. As the mobility of gallium is quite low a significant portion of this gallium stays in the carbon layer during the selenisation step (see section 4.3). To facilitate the discrimination of effects based on the gallium in the carbon layer and on the carbon layer itself, both standard gallium containing and gallium-free printed CIGS-layers have been prepared.

The preparation process for the samples used for this examination is exactly the same as for the gallium-containing samples (see figure 7.1). It is stopped after the etching of the printed CIGS-layer.

The resulting layer based on *gallium-containing precursors* is smooth and does not show significant residues of the original CIGS-layer (see figure 7.6). The carbon layer is quite porous and shows flat voids. It can be assumed that these voids originate from the selenisation process where the metal ions diffuse to the top of the precursor layer to react with the selenium, since the original precursor layers are dense, amorphous layers as can be seen in chapter 3.2.1.

The layers based on *gallium-free precursors* are more uneven (see figure 7.9). The thickness of the layers varies strongly and the voids are much bigger than for standard, gallium-containing layers. Due to the strongly varying thickness of this gallium-free carbon layer the CIGS-layers on top grow quite irregular. Hence, the original intention to distinguish easily between the influence of gallium in the layer and the carbon layer itself is hindered to some extent. This is discussed in more detail in the following sections.

The chemical composition can be seen in SIMS-measurements which were carried out with and without evaporated absorbers on top. In figure 7.7 the measurements on samples with absorbers are shown. This method is very sensitive to low concentrations so even small contaminations can be detected (see chapter 3.1.1). Furthermore it can measure both oxygen and carbon, which are obviously important for the analysis of carbon layers.

The SIMS measurements show that quite a lot of gallium is left in the carbon layer. Within the carbon layer a scan over all atomic masses is carried out. No significant contamination except for bromine (from the etching process) can be seen in this scan. To guarantee that this contamination is not decisive for the properties of the carbon layer in the experiments another etching process was used for one deposition process — during one of the 250 nm processes. These samples showed similar results. Since the alternative etching is harmful for the back contact, it is not used for the majority of the experiments.

As chlorides are used for the precursor, potential contaminations with chlorine are especially

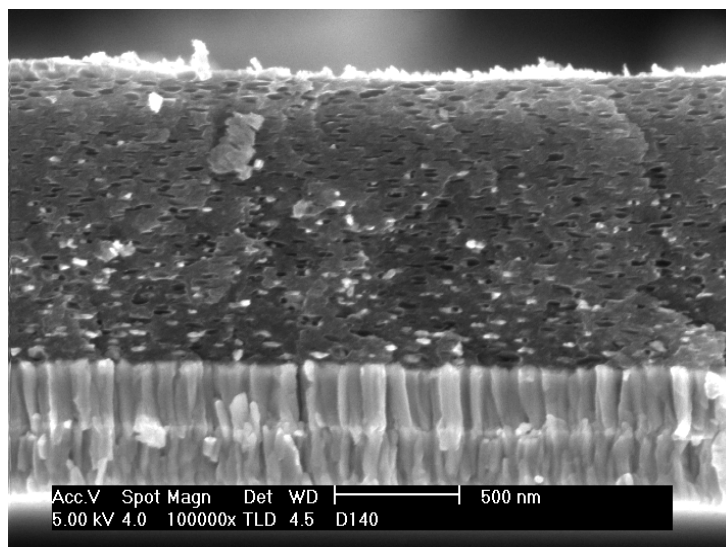


Figure 7.6: SEM Picture of Gallium-Containing Carbon Layer.

After the printing process the CIGS-layer is etched away. The residual carbon layer which can be seen in this SEM picture is used with a subsequent co-evaporated CIGS -layer to study the influence of the carbon layer. Here a standard, gallium-containing layer is shown. The smooth surface and small voids can be seen.

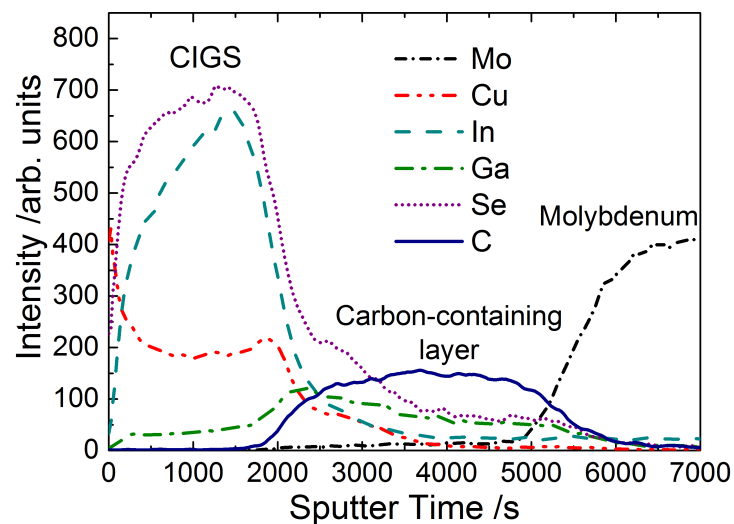


Figure 7.7: SIMS Measurement of CIGS and Carbon Layer.

Secondary ion mass spectrometry shows that gallium stays in the carbon layer while selenium only penetrates into to upper part of the carbon layer.

interesting. Only with negative SIMS-measurements these contaminations could be seen and as they penetrate the molybdenum layer completely they can not be ascribed unambiguously to the precursor. Nonetheless they are still quite low, so that the influence is assumed to be negligible.

Other back contact properties which are potentially changed for carbon layers are the reflectivity and the conductivity. The different reflectivity is obvious to the naked eye and can cause significant changes in performance especially for thin absorbers. The conductivity would require more investigation. Usually precursor layers were doctor bladed on molybdenum covered samples to avoid adhesion problems. Yet in order to measure the conductivity it is important not to have molybdenum underneath. However, even with structured molybdenum substrates it was not possible to measure the conductivity of the carbon layer. The I - V characteristics indicate, though, that the conductivity is high enough not to harm the performance significantly.

7.2 Series Resistances – Carbon Layer Thickness Variation

By varying the slit height during doctor blading the carbon layer thickness for printed absorber layers can be altered which should affect the series resistances within the complete solar cell. So after etching the CIGS-layer, various carbon layer thicknesses have been fabricated. The exact thickness of each carbon layer was determined with SEM-pictures of the completed cells: At least four points of each sample were measured — for inhomogeneous layers more — and the average values of these measurements are taken in the following. Exemplary SEM-images can be found in figure 7.8 and 7.9. The carbon layers in figure 7.8 are made with *gallium-containing precursors* and are therefore very smooth. Thus also the CIGS-layers co-evaporated on top of these layers are quite smooth and regular. In contrast the samples in figure 7.9 are fabricated with *gallium-free carbon layers*. They are extremely uneven and so is the subsequent CIGS-layer. Yet the measured efficiencies are comparable even though the highest efficiency is reached with gallium containing carbon layers.

The measurements with varying carbon layer thickness show a correlation between the carbon layer thickness and the strength of its influence (see figure 7.10, 7.11 and 7.12 [267]). Whereas the correlation between carbon layer thickness seems to be quite pronounced for 950 nm and 230 nm it is much less obvious for 550 nm.

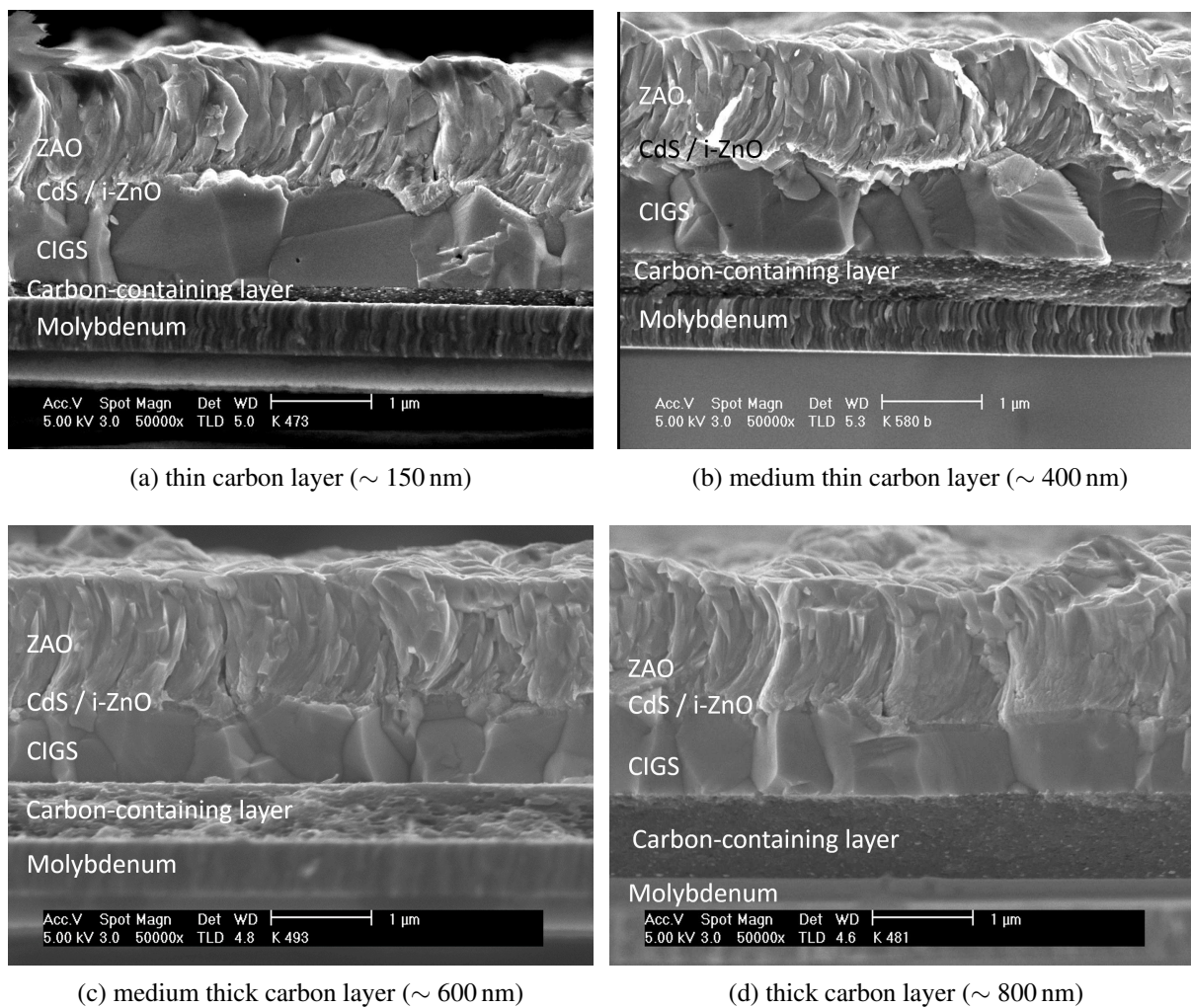
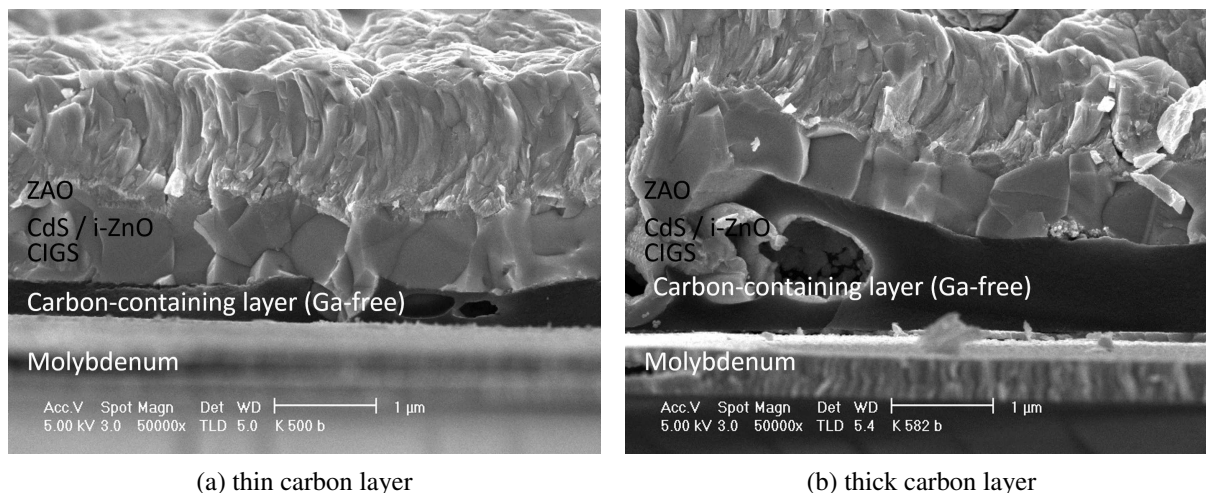


Figure 7.8: Gallium-Containing Carbon Layers with Various Thicknesses.

SEM-images of exemplary samples are shown. While the carbon layer thickness is varied the CIGS-layer thickness is the same for all samples. The smooth carbon layer surface facilitates a rather smooth CIGS growth on top of it.

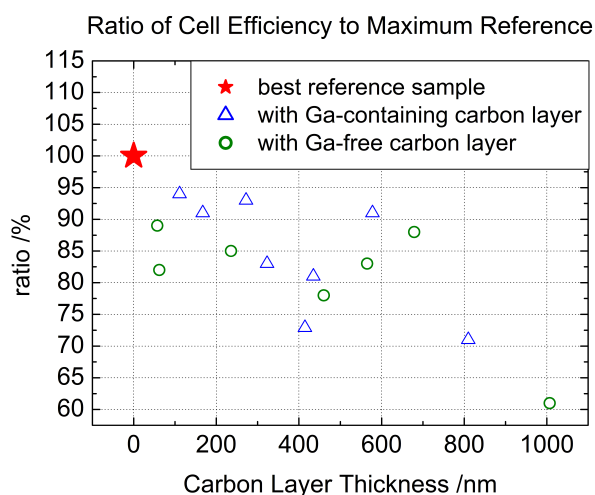


(a) thin carbon layer

(b) thick carbon layer

Figure 7.9: Gallium-Free Carbon Layers with Various Thicknesses.

SEM-images of exemplary samples are shown. While the carbon layer thickness is varied the CIGS-layer thickness is the same for all samples. The carbon layer is extremely uneven, likewise the subsequent CIGS-layer is quite uneven.

**Figure 7.10:** Cell Efficiency Normalised to Maximum Reference Efficiency for 950 nm CIGS.

The maximum cell efficiencies of all cells in the 950 nm-deposition process are normalised to the maximum reference efficiency. These values are plotted over carbon layer thickness.

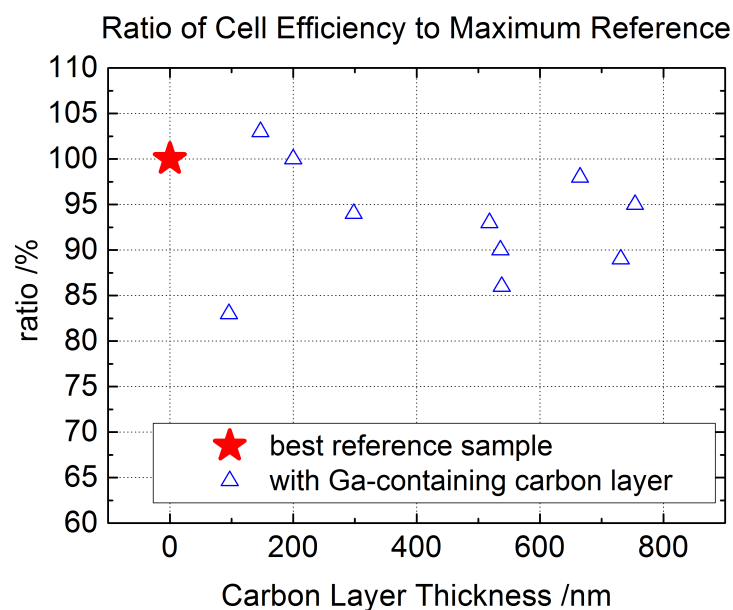


Figure 7.11: Cell Efficiency Normalised to Maximum Reference Efficiency for 550 nm CIGS.

The maximum cell efficiencies of all cells in the 500 nm-deposition process are normalised to the maximum reference efficiency. These values are plotted over carbon layer thickness.

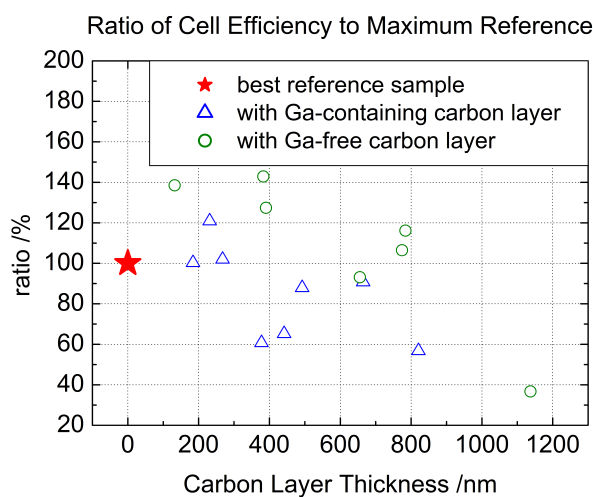


Figure 7.12: Cell Efficiency Normalised to Maximum Reference Efficiency for 230 nm CIGS.

The maximum cell efficiencies of all cells in the 230 nm-deposition process are normalised to the maximum reference efficiency. These values are plotted over carbon layer thickness.

There are several conclusions one can draw from the experiments: A positive effect of a carbon layer can only be seen for thin carbon layers. For very thick layers a quite negative effect can be seen. This holds true both for gallium-containing and gallium-free carbon layers. The fact that also gallium-free carbon layers have a similar effect as the gallium-containing ones already shows that gallium is not decisive for the beneficial effect. In figure 7.13 I - V characteristics for 950 nm thick absorbers with different carbon layer thicknesses are shown. The carbon layer is an additional series resistance which is disadvantageous for the cell's performance. For the thick carbon layer a much smaller fill factor is observed than for the corresponding cell with a thin layer confirming the higher series resistance, which explains the lower performance for these cells.

7.3 CIGS Layer Thickness Variation

CIGS layer thickness has a great influence on the performance of a solar cell. This can be seen clearly for the reference cells shown in chapter 7.1.2 — figure 7.3. Hence it is logical to vary this parameter also for the carbon layer including cells. The experiments should determine the potential of an arbitrary carbon layer, therefore the analysis of the experiments uses the highest reached efficiency per deposition process. This best-in-class approach allows the potential of the cell configuration with a carbon layer and this certain CIGS-layer thickness to be seen. The influence of possible variations in the thickness and the fabrication process in general for the carbon layers is minimised since the best-in-class cells are determined from a large range of different carbon layers. So for each thickness the ratio of the maximum efficiency of all cells with a carbon layer to the maximum efficiency of the reference cells is determined.

In one set of experiments four different thicknesses of absorbers are fabricated. The thinnest layers were supposed to be nominally as thin as the printed absorbers, that is in general 230 nm, yet in this set it was 300 nm. Additionally absorbers with a nominal thickness of 500 nm, 750 nm and 950 nm are prepared. Exemplary samples for each thickness are shown in figure 7.14.

The influence of the additional carbon layer varies strongly with absorber thickness (see figure 7.15). While it is positive for very thin layers, the effect gets less pronounced the thicker the layers are. For the thicker layers the carbon layer shows a negative effect for the maximum efficiency.

For the CIGS-layers under examination the difference in thickness is more than 10%. While reference samples show a thickness of for example 950 nm in average, the corresponding cells from the same evaporation process with an additional carbon layer measure only 820 nm. Nonetheless even for the thickest CIGS-layer the difference in efficiency is not very high and

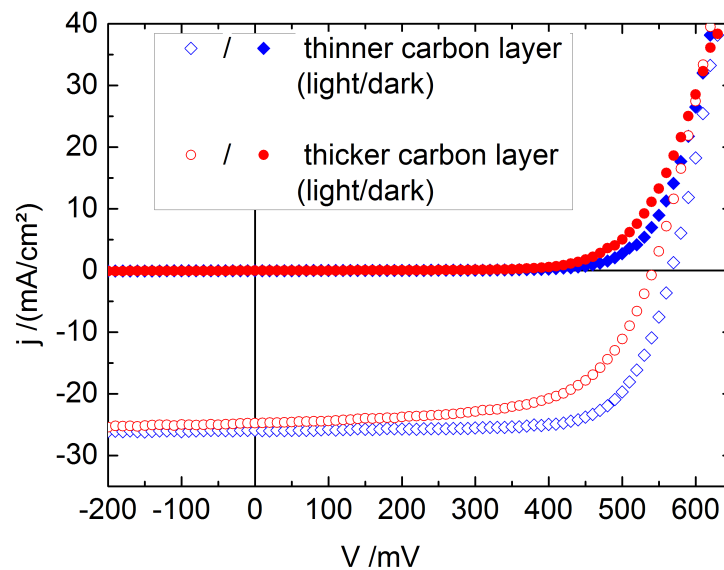


Figure 7.13: Comparison of I – V characteristics for Different Carbon Layer Thickness.

Comparing the I – V characteristics of a cell with an approximately 170 nm thin carbon layer to one with an approximately 810 nm one, a higher series resistance and a lower open circuit voltage can be found for the thicker layer.

the highest efficiency reached by a carbon layer cell still has nearly 95 % of the highest efficiency of a reference cell. Bearing this in mind one can assume that the effect would be even more positive than it seems in figure 7.15, if the absorber layer thickness was the same.

The increase in efficiency is related to both an increase in open circuit voltage and short circuit current density yet the increase in open circuit voltage is more significant. A new experiment with thinner absorber layers (230 nm) shows this fact even more striking: While the increase in j_{sc} is not very distinctive (from 19.1 mA/cm² for the best reference sample to 19.4 mA/cm² for the best cell with carbon layer), the increase in V_{oc} is very pronounced especially for these thin layers as can be seen in figure 7.16 (from 367 mV for the best reference cell to 489 mV for the best cell with carbon layer).

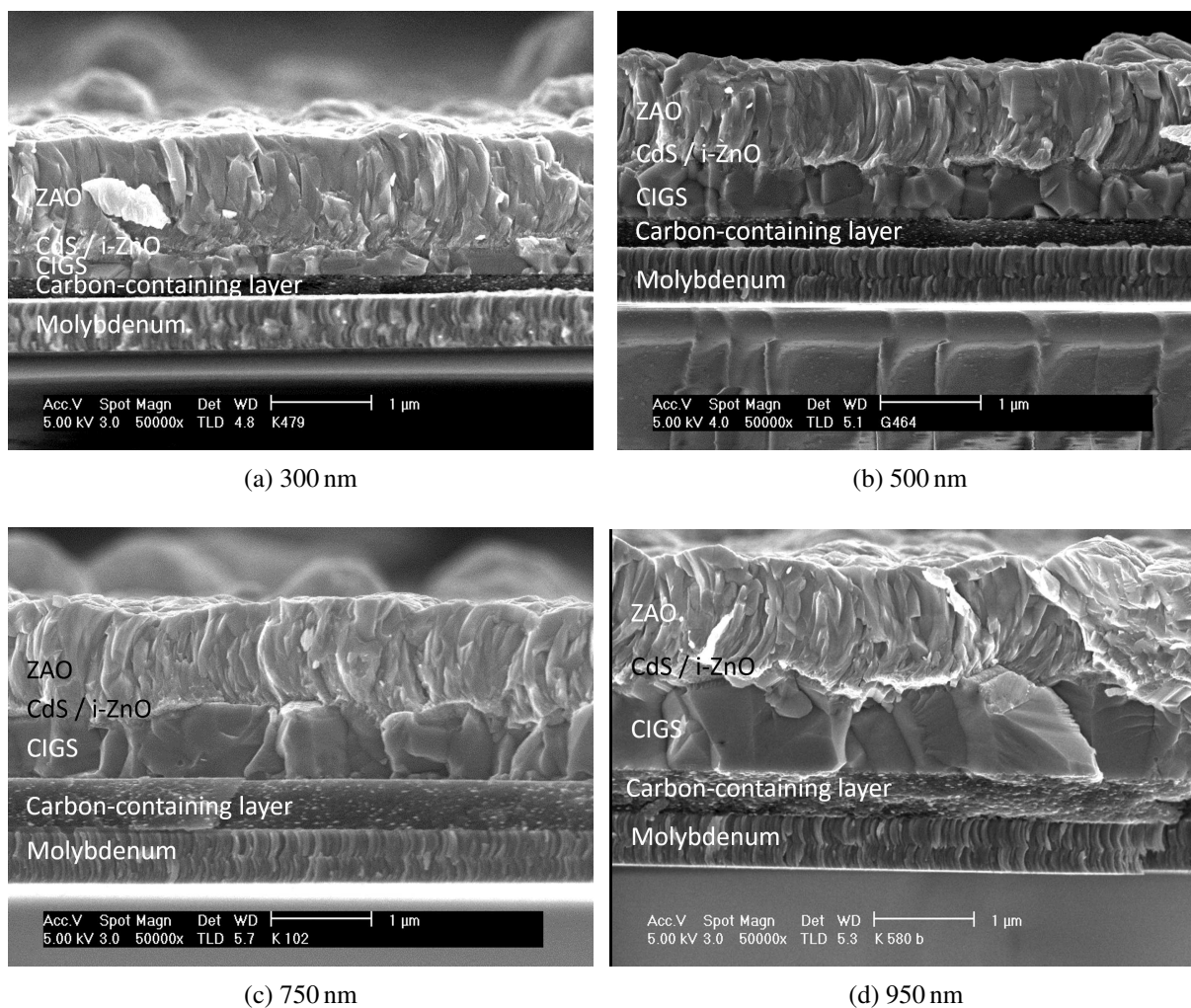


Figure 7.14: Varying CIGS Layer Thickness on Carbon Layers.

SEM-images of exemplary samples are shown. The stated thicknesses are only nominal and represent an average of the reference samples fabricated in the same batch. In general the absorber layers on carbon are thinner.

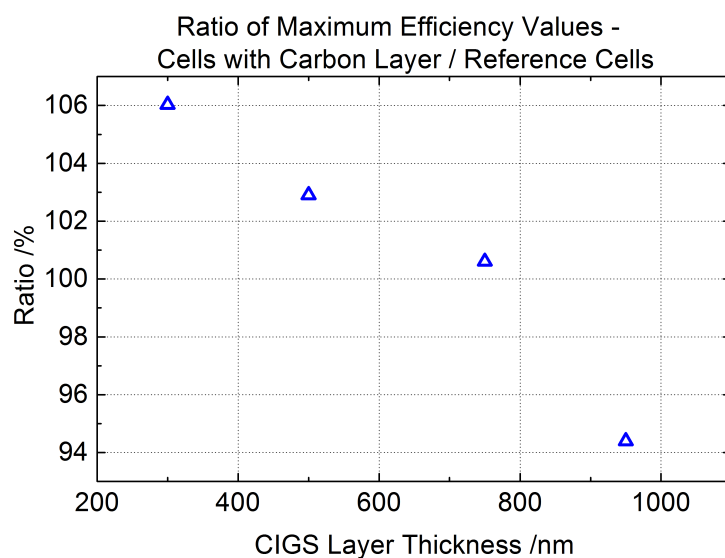


Figure 7.15: Ratio of Maximum Efficiency Values for Cells with Carbon Layer to Reference Cells.

For each thickness the ratio of the maximum efficiency of a cell with suitable (in general quite thin) carbon layer to the maximum efficiency of all reference samples is determined. For thinner CIGS-layers a positive effect can be seen which is more pronounced the thinner the layers are. For thicker layers a carbon layer shows a negative effect for the maximum efficiency.

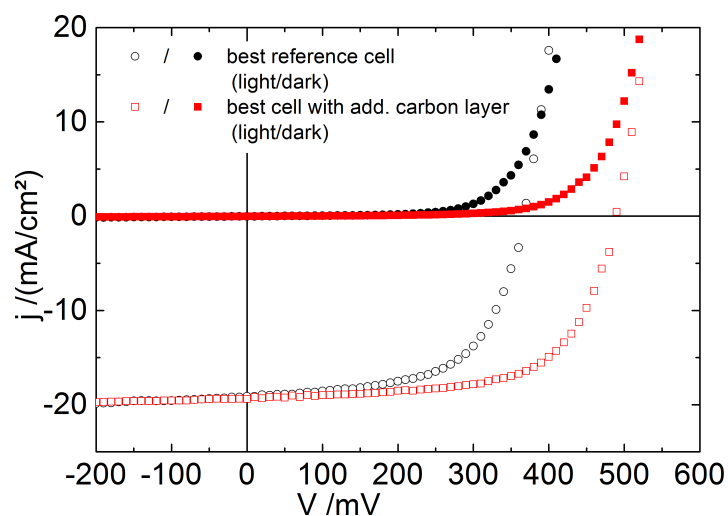


Figure 7.16: I - V Characteristics of the Best Cells for the 230 nm CIGS Deposition Run.

For 230 nm CIGS a strong increase in efficiency is seen (4.3 % for the best reference cell to 6.1 % for the best cell with carbon layer). It can be clearly seen that the open circuit voltage increases for cells with an additional carbon layer at the back contact (from 367 mV to 489 mV) while the current density hardly increases (from 19.1 mA/cm² to 19.4 mA/cm²).

7.4 Discussion

Intuitively an additional carbon layer between the absorber layer and the back contact is expected to lower the overall conversion efficiency significantly. Yet for thin absorber layers the opposite is true. The measurements are ambiguous in regard to the reason of this efficiency increase.

The carbon-containing layer under investigation also contains gallium from the precursor ink. Thus the idea suggests itself that the chemical composition of the CIGS layer is somehow altered by the gallium. Yet the experiments with gallium-free carbon layers showed clearly that this is not the case. The same effect can be observed with the gallium-free layers.

Absorbers grown by the same fabrication process have different resulting thicknesses depending on whether the absorber is deposited on a carbon layer or directly on molybdenum. This difference indicates a modified growth on carbon layers. It is not clear how this altered growth changes the properties of the resulting absorber layers. Certainly the morphology is affected and this might explain the positive effect on the efficiency of the solar cells. It is not clear what causes this altered growth and what its consequences are. Yet as the efficiency is only increased for thin CIGS layers but not for thicker layers it seems rather unlikely that a changed morphology is the main cause for this efficiency increase.

In standard CIGS solar cells the combination of MoSe_2 and Mo at the back contact creates a completely black back contact for the Cu(In,Ga)Se_2 absorber layers. A carbon layer instead of the MoSe_2 layer is a change that might enhance the reflection at the back contact. Then the light which is not absorbed within the absorber is reflected back and traverses the absorber layer again and can be absorbed during this second transition and contribute to the created current. Quantum efficiency measurements show that the current density is only slightly increased. Therefore this, too, cannot be the main effect but contribute only by a small proportion.

With several semiconducting materials involved one definitely has to look at possible changes in the electronic configuration of the back contact. For the front contact band alignment issues have often been an important topic [92, 268–270], for the back contact for a long time only minor interest has been shown [104, 271]. For the electronic configuration of the back contact interface two objectives are decisive: Holes can be inserted easily into the absorber and their recombination with electrons is avoided as effectively as possible. In both cases an additional layer at the back contact has the potential to change the situation.

In most publications the standard molybdenum back contact with its MoSe_2 layer is found to be ohmic [104, 105, 272–274]. Thus we assume that an additional carbon layer cannot be responsible for the improvement seen, especially with regard to the open circuit voltage.

As the back contact is altered the recombination at the back contact will change as well. For absorber layers thinner than the effective diffusion length the recombination at the back contact has a far greater influence on the solar cell performance. At the same time the possibilities to avoid recombination by a gallium grading are restricted. Therefore especially for very thin absorber layers this difference can have a tremendous effect [266, 275].

At the Ångström Solar Center in Uppsala the correlation of the conversion efficiency with the absorber thickness and the back contact recombination is studied — both theoretically and experimentally [276]. Likewise Touafek et al. do calculations to investigate this topic [275]. They both show with calculations and experiments that the open circuit voltage is increased significantly for lower back surface recombination velocities, as long as the absorber is thin enough. The short circuit current density is affected only slightly by a change in the recombination velocity. For the current the stronger effect by far is the one caused by a change in absorber thickness and a resulting incomplete absorption of the incident light. For very thin absorber layers the fill factor as well is influenced by the recombination velocity. All these effects combined cause a quite dramatic increase in efficiency for lower recombination velocities. No effect can be seen with thick absorbers.

It is not clear how the recombination is reduced so significantly. Vermang et al. use an interface design inspired by the back contact of high efficiency silicon solar cells [277]. Silicon solar cells have to reduce the back contact recombination to reach high efficiencies. Therefore often point contacts in otherwise passivated back surfaces are used. In principle we assume that the carbon builds a conducting layer, but if this is not true it might form a passivation layer with point-like current paths. To resolve this open question the carbon layer has to be examined more closely.

Most probably a combination of these factors is possible. A different reflexion gives slightly better short circuit current and hence already a slightly better voltage and the lowered recombination at the back contact increases the voltage significantly so that the overall efficiency for solar cells with thin absorber layers is increased with an additional carbon layer.

7.5 Simulations

In order to review our hypotheses that an altered recombination at the back contact could be the reason for the measured effect simulations were performed. For these simulations SCAPS was used. SCAPS is an acronym for "Solar Cell Capacitance Simulator" and is a programme developed at the Department of Electronics and Information Systems (ELIS) of the University of Gent [28, 278]. It allows to simulate structures with up to 7 semiconducting layers.

As an initial point for the design of the simulation model input parameters of Frisk et al. [279] were used and adopted for the here used process. The detailed input parameters can be found in the appendix A. Here only the parameters changed for the simulations are mentioned. As the additional carbon layer investigated here is assumed not to be a semiconducting layer it could not be simulated as an additional layer. Instead the parameters of the back contact itself are altered.

Unlike the semiconducting layers the back contact is represented with only a few parameters. When choosing flat band conditions only the thermionic emission / surface recombination velocity can be defined for electrons and holes. To account for the altered recombination at the back contact with the additional layer between CIGS and molybdenum back contact the velocity for electrons is varied between $1 \times 10^4 \text{ cm s}^{-1}$ and $1 \times 10^7 \text{ cm s}^{-1}$ during the simulations. $1 \times 10^7 \text{ cm s}^{-1}$ is the standard value used in many other simulations with a standard back contact and is therefore used here for the reference cells without an additional layer at the back contact.

By adopting the model to thin absorber layers (230 nm) it gives the measured values for these thin absorber layers (see fig. 7.17). This reference model is then changed at the back contact to get a model for the cells with additional layer at the back contact. It can be seen in fig. 7.17 that with this change in the recombination velocity the increase in open circuit voltage can be implemented. By direct comparison with the experimental data in fig. 7.16 it can be seen that the model can reproduce the measured curves and shift in V_{oc} very well. Thus the simulations indicate that the explanation for the observed effect of an additional layer at the back contact for thin absorber might be true.

In summary it can be stated that for thin CIGS absorber layers an additional thin carbon layer between absorber and molybdenum back contact is beneficial. Thick carbon layers at the back contact do not increase the efficiency neither for thin nor thick absorbers. For absorbers thicker than 800 nm the additional carbon layer does not increase the efficiency regardless of its thickness. The higher efficiency for thin absorber layers is mainly caused by an increased open circuit voltage. The reasons for this increase are most probably related to an altered recombination at the back contact but can not be completely determined and need further research. Understanding the mechanism of this increase can help to lower the absorber thickness of CIGS solar cells and save costs in the production process of thin film solar cells.

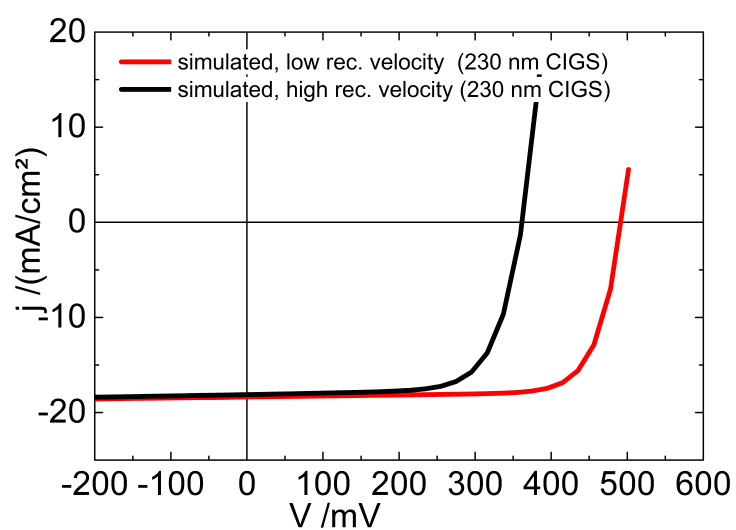


Figure 7.17: Simulated I - V Characteristics of Reference Cell and Cell with Additional Carbon Layer with 230 nm CIGS.

For 230 nm CIGS simulations show that the open circuit voltage increases for lower surface recombination velocities at the back contact.

Chapter 8

Summary and Outlook

In order to competitively generate electricity with solar cells their fabrication has to become more cost-efficient. Vacuum-free production processes offer the possibility of a significant cost reduction in the absorber fabrication. With these vacuum-free processes the cell properties are altered. As such processes have been developed during the course of this thesis a thorough investigation of the new properties is necessary. For the present thesis the impact especially on the back contact interface has been studied. In the following chapter the findings are summarised briefly and a short outlook on possible future research is given.

8.1 Summary

In order to investigate the interface properties of absorbers built with non-vacuum processes a basic non-vacuum selenisation process has been developed initially. The selenisation set-up has been designed and built up and the corresponding process has been optimised: A crucial factor for a good absorber quality is the selenium partial pressure at the beginning of the selenisation process. Thus the newly developed process included a preheating step of the selenium source which helped to ensure that enough selenium was supplied at the most sensitive phase in the beginning of the process. When the precursors were heated up with a sufficient selenium vapour pressure in the furnace, less precursor material was lost and the chemical composition of the resulting layer was more easily kept in the range for good absorbers.

The selenisation process had to be adapted individually for each precursor type to meet the different needs of the precursor layers. For all employed precursor alternatives the most suitable selenisation process was determined in this work.

As a next step the molybdenum selenide formation and the influence of the changed selenium partial pressure on it has been investigated: Both the molybdenum fabrication process and the selenisation were found to influence the MoSe_2 formation. For the molybdenum fabrication the

the density of the layer which can be adjusted by changing the sputter pressure was the most influential parameter. A higher density of the molybdenum (corresponding to a lower sputter pressure) led to more selenide formation. During the selenisation the substrate temperature was found to be one of the key factors. Higher substrate temperatures led to a stronger selenide formation. In general the selenide formation occurred for temperatures more than 450 °C.

In the following experiments it has been shown that precursor layers on top of the molybdenum layer altered the selenide formation. Both the sputtered alloy precursors and the metal salt based doctor bladed precursors have been used for these experiments.

For sputtered precursors MoSe₂ was formed during the selenisation. Both orientations of the selenide were detectable. The ratio between the less preferred parallel and the more favourable perpendicular orientation improved with higher selenium source temperature thus a higher selenium partial pressure. Especially for standard molybdenum this relation was important.

For doctor bladed precursors made from metal salts with ethylcellulose no molybdenum selenide formation has been observed. These precursors prevented the selenisation of the back contact quite effectively. During the formation of the CIGS absorber layer a carbon layer was left between absorber and back contact which seemed to protect the molybdenum. This can be important for selenisations with a higher selenium partial pressure where the molybdenum selenide formation can become too strong..

Finally the influence of this carbon layer on the solar cell properties has been investigated. The findings from this investigation were counterintuitive at first glance. For thin absorber layers an additional thin carbon layer between back contact and absorber material was beneficial. Especially very thin layers showed significantly higher open circuit voltages. Gallium was found prominently within the carbon layer but did not play a significant role as measurement with gallium-free carbon layers verify. While the reason for this positive effect could not be determined with certainty, various explanation approaches seemed suitable. Most likely a significantly lower recombination at the back contact is a key factor for the higher voltages in samples with a carbon layer at the back contact. Simulations with the Solar Cell Capacity Simulator (SCAPS) back up this assumption and show a clear increase in open circuit voltage for thin absorber layers with a lower recombination velocity at the back contact.

This effect can help to keep the conversion efficiencies of solar cells high while reducing the absorber thickness. Thus two possibilities for steps on the way towards cost-efficient solar cells have been presented. Non-vacuum processes for the absorber fabrication have been implemented and an idea how thinner absorber layers can still show relatively high conversion efficiencies has been substantiated.

8.2 Outlook

The goal for the future remains to reduce the production costs for electricity. As many parts of the cost structure for thin film solar cells are independent from the absorber layer, efficiencies are extremely important. Thus for scientific and technological progress efficiency enhancement is the main focus.

Based on the findings of this thesis several topics are to be pursued: The efficiencies of solar cells fabricated with non-vacuum methods have to be increased significantly to improve competitiveness with cells from conventional processes. For the selenisation a higher selenium partial pressure is likely to be advantageous. When transferring parameters from selenisation processes for conventionally produced precursors to processes for vacuum-free fabricated ones it has to be kept in mind that the selenisation process has to be developed for each precursor type individually. Thus only basic correlations can be adopted and additional research is necessary to further increase the efficiencies.

Additionally it is important to fully understand the mechanism of the additional carbon layer at the back contact. If it is related to the changed recombination, this might be comparable to the processes in silicon solar cells. Then the technology of silicon based solar cells can serve as a source of inspiration which suggests a passivation layer at the back contact for high efficiency solar cells. On the one hand it can be used for thin absorbers where this passivation layer can help to reach at least acceptable efficiencies while less material is used. On the other hand it can also help to further improve thin film solar cells with world record efficiencies where every possibility even for small improvements has to be investigated.

Finally all these improvements, together with many other measures, are further steps to reach the goal of sustainable energy supply through reducing the production costs for photovoltaic electricity.

Appendix A

SCAPS Input Parameter

For the simulations presented in chapter 7.5 the freely available program SCAPS (version 3.3.02) has been used. The following pages show detailed input parameters for the relevant layers. First the general structure is displayed A.1, then the CIGS layer A.2 with its defect parameters A.3 and its composition grading A.4 is shown. Finally the standard parameters for the back contact parameters are presented A.5

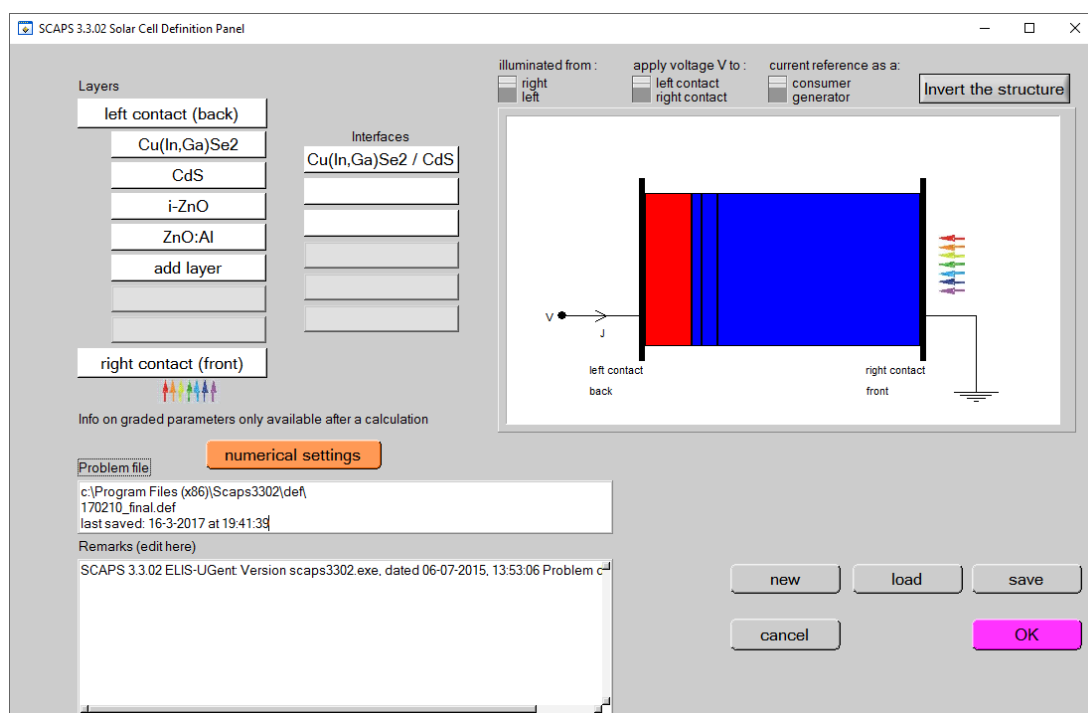


Figure A.1: Overview of the Simulated Solar Cell Structure.

The complete structure of the simulated cell can be seen: The CIGS layer has a thickness of 230 nm, the buffer layer CdS 50 nm, the i-Zno 80 nm and the Al-doped ZnO 1 μ m.

SCAPS 3.3.02 Layer Properties Panel

LAYER 1 Cu(In,Ga)Se2

thickness (μm)

Composition y at left and right side of layer

Semiconductor Property P of the pure material

| | | | |
|--|-----------|-----------|-----------|
| bandgap (eV) | 1.010 | 1.636 | parabolic |
| electron affinity (eV) | 4.500 | 3.874 | parabolic |
| dielectric permittivity (relative) | 13.600 | 13.600 | linear |
| CB effective density of states ($1/\text{cm}^3$) | 6.800E+17 | 6.800E+17 | linear |
| VB effective density of states ($1/\text{cm}^3$) | 1.500E+19 | 1.500E+19 | linear |
| electron thermal velocity (cm/s) | 3.900E+7 | 3.900E+7 | linear |
| hole thermal velocity (cm/s) | 1.400E+7 | 1.400E+7 | linear |
| electron mobility (cm^2/Vs) | 1.000E+2 | 1.000E+2 | linear |
| hole mobility (cm^2/Vs) | 1.250E+1 | 1.250E+1 | linear |
| effective mass of electrons | 9.000E-2 | 9.000E-2 | linear |
| effective mass of holes | 7.200E-1 | 7.200E-1 | linear |

Allow Tunneling

no ND grading (uniform)

shallow uniform donor density ND ($1/\text{cm}^3$)

no NA grading (uniform)

shallow uniform acceptor density NA ($1/\text{cm}^3$)

Absorption model

| | | |
|---|---|---|
| | alpha (y=0) | alpha (y=1) |
| | <input type="text" value="from model"/> | <input type="text" value="from model"/> |
| | <input type="text" value="from file"/> | <input type="text" value="from file"/> |
| absorption constant A ($1/\text{cm eV}^{1/2}$) | <input type="text" value="4.300E+4"/> | <input type="text" value="4.300E+4"/> |
| absorption constant B ($\text{eV}^{1/2}/\text{cm}$) | <input type="text" value="0.000E+0"/> | <input type="text" value="0.000E+0"/> |

Recombination model

Band to band recombination

| | | | |
|--|--|--|--------------------------------------|
| Radiative recombination coefficient (cm^3/s) | <input type="text" value="1.000E-10"/> | <input type="text" value="1.000E-10"/> | <input type="text" value="linear"/> |
| Auger electron capture coefficient (cm^6/s) | <input type="text" value="0.000E+0"/> | <input type="text" value="0.000E+0"/> | <input type="text" value="uniform"/> |
| Auger hole capture coefficient (cm^6/s) | <input type="text" value="0.000E+0"/> | <input type="text" value="0.000E+0"/> | <input type="text" value="uniform"/> |

Recombination at defects: Summary

Defect 1

charge type : donor : (+,0)

total density ($1/\text{cm}^3$): Left 1.000e+14; Right 5.000e+12

grading Nt(x): beta-function

energy distribution: single; Et = 0.00 eV above Ei

this defect only, if active: tau_n = 5.1e-01 ns, tau_p = 7.1e+03 ns

this defect only, if active: Ln = 3.6e-01 μm , Lp = 1.5e+01 μm

(no metastable configuration possible)

Figure A.2: Simulation Parameters for the CIGS Layer.

Here the general parameters for the CIGS layer are shown. The thickness is 230 nm.

SCAPS 3.3.02 Defect Properties Panel

Defect 1 of Cu(In,Ga)Se2

| | |
|--|--------------------|
| defect type | Single Donor (0/+) |
| capture cross section electrons (cm ²) | 5.000E-13 |
| capture cross section holes (cm ²) | 1.000E-16 |
| energetic distribution | Single |
| reference for defect energy level Et | Above Ei |
| energy level with respect to Reference (eV) | 0.000 |
| characteristic energy (eV) | 0.100 |

Nt grading dependent on position x: Nt (x) beta function

Nt total (1/cm3) Left (x=0) 1.000E+14 Right (x=1) 5.000E+12

Optical capture of electrons From model From file

| | |
|------------------------------------|----------|
| refractive index (n) | 3.000 |
| effective mass of electrons (rel.) | 1.000E+0 |
| effective field ratio | 1.00E+0 |
| cut off energy (eV) | 10.00 |

optical electron capture cross sections file:

Optical capture of holes From model From file

| | |
|--------------------------------|----------|
| refractive index (n) | 3.000 |
| effective mass of holes (rel.) | 1.000E+0 |
| effective field ratio | 1.00E+0 |
| cut off energy (eV) | 10.00 |

optical hole capture cross sections file:

Figure A.3: Defect Parameters Used for SCAPS Simulation of CIGS Layer.

The simulation parameters for the defect properties are shown here. The distribution of the defect follows a beta function to implement the fact that close to the back contact the film quality in general is lower.

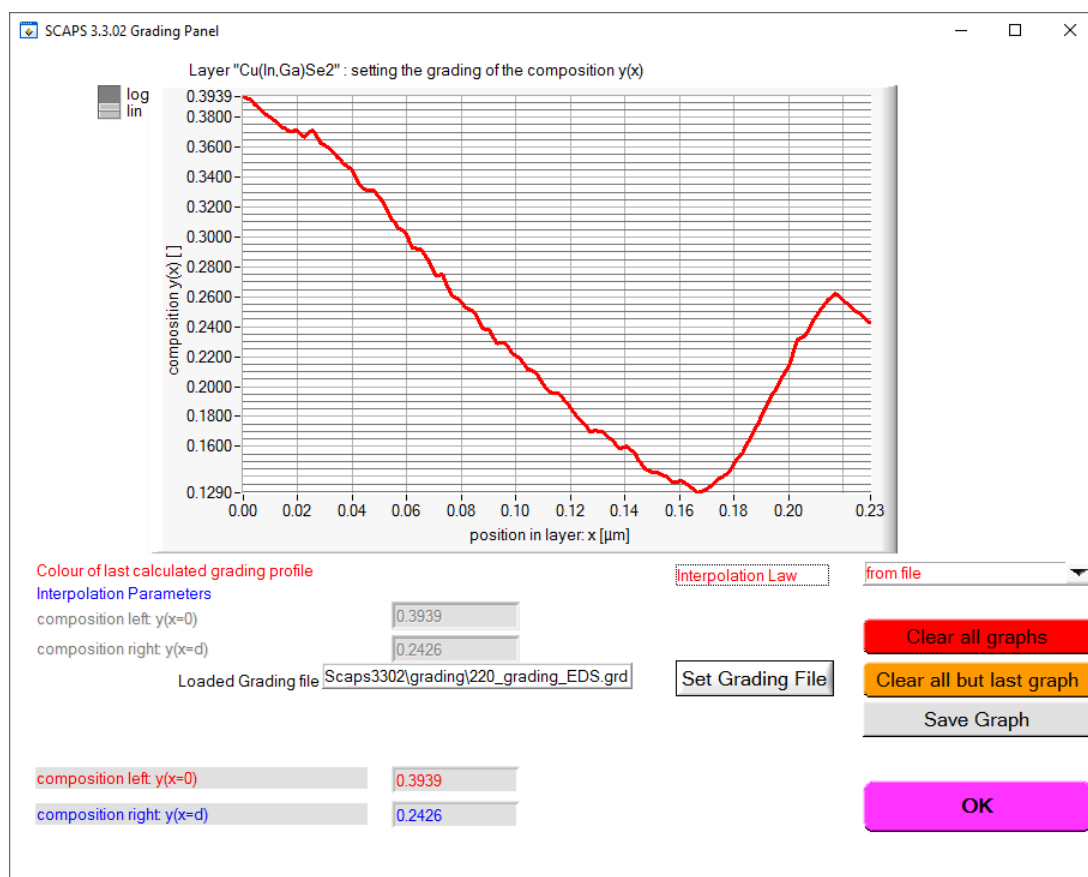


Figure A.4: Composition Grading Used for SCAPS Simulation of CIGS Layer. A quite important property of the CIGS layer is its composition grading which is displayed here.

The screenshot shows a dialog box titled "Left Contact (Back)" with a close button (X) in the top right corner. The dialog is divided into two main sections: "Electrical properties" and "Optical properties".

Electrical properties section:

- Thermionic emission / surface recombination velocity (cm/s):
 - electrons: 1.00E+7
 - holes: 1.00E+7
- Metal work function (eV): 5.0714
- or flat bands
- Majority carrier barrier height (eV):
 - relative to EF: 0.4386
 - relative to EV or EC: 0.0000
- In batch mode, recalculate Phi_m:
 - at each step
 - at first step only
- Allow contact tunneling
- Effective mass of electrons: 1.00E+0
- Effective mass of holes: 1.00E+0

Optical properties section:

- optical filter
- Filter Mode: transmission, reflection
- Filter Value: 0.000000
- Complement of Filter Value: 1.0000E+0
- From Value
- From File
- Select Filter File: [Text Field]

At the bottom of the dialog are two buttons: "OK" (highlighted in pink) and "cancel".

Figure A.5: Parameters Used for SCAPS Simulation of Back Contact.

The standard parameters for the back contact are shown here. To simulate the cells with an additional carbon layer the recombination velocity was varied.

Symbols and Abbreviations

| | |
|--------------------------|---------------------------------------|
| CGI | ratio of copper to gallium and indium |
| CIGS | Cu(In,Ga)Se_2 |
| D_n | diffusion coefficient for electrons |
| D_p | diffusion coefficient for holes |
| E_C | conduction band energy |
| EDX | energy dispersive x-ray |
| E_F | Fermi energy |
| E | electric field |
| E_g | band gap energy |
| E_{ph} | photon energy |
| E_V | valence band energy |
| FF | fill factor |
| G | generation rate |
| GGI | ratio gallium to gallium and indium |
| h | Planck's constant |
| H_2Se | hydrogen selenide |
| In_2O_3 | indium oxide |
| InSe | indium (II) selenide |
| In_2Se_3 | indium (III) selenide |
| $I-V$ | current – voltage |
| J_{sc} | short circuit current |
| j_{sc} | short circuit current density |
| J_{ph} | photo current |
| J_s | reverse bias saturation current |
| MoSe_2 | molybdenum selenide |
| η | power conversion efficiency |
| k_B | Boltzmann constant |
| μ_n | electron mobility |
| μ_p | hole mobility |

| | |
|------------------|--|
| mpp | maximum power point |
| n | electron density |
| p | hole density |
| P_{in} | incident power |
| PL | photoluminescence |
| P_{max} | maximum power |
| q | elementary charge |
| QE | quantum efficiency |
| R | recombination rate |
| R_{p} | parallel resistance |
| R_{s} | series resistance |
| RTA | rapid thermal annealing |
| SEL | stacked elemental layers |
| SEM | scanning electron microscopy |
| SIMS | secondary ion mass spectroscopy |
| SNMS | secondary neutral particle mass spectroscopy |
| T | temperature |
| V | voltage |
| V_{bi} | built-in voltage |
| V_{mpp} | voltage at maximum power point |
| V_{oc} | open circuit voltage |
| XRF | x-ray fluorescence analysis |
| XRD | x-ray diffraction |
| ZSW | Zentrum für Sonnenenergie- und Wasserstoff-Forschung |

List of Figures

| | | |
|------|--|----|
| 2.1 | Band Diagrams of p- and n-type Semiconductors | 12 |
| 2.2 | Electric Field at p-n Junction | 13 |
| 2.3 | p-n Junction | 13 |
| 2.4 | Single Diode Model | 16 |
| 2.5 | I - V Characteristics of a Typical Solar Cell | 16 |
| 2.6 | Derivation of Crystal Structure | 20 |
| 2.7 | Chalcopyrite Structure | 21 |
| 2.8 | Typical Cell Configuration | 24 |
| 2.9 | Band Diagram for Typical Cell Configuration | 24 |
| 2.10 | Overview of Fabrication Methods | 27 |
| | | |
| 3.1 | Procedure for Preparation of Metal Salt Precursors | 41 |
| 3.2 | Doctor Blading of Metal Salt Solution | 42 |
| 3.3 | SEM Image of Doctor Bladed Metal Salt Precursor | 42 |
| 3.4 | Mapped Thickness of Doctor Bladed Metal Salt Precursor | 43 |
| 3.5 | Composition of Doctor Bladed Metal Salt Precursor | 44 |
| 3.6 | Reduction Equipment | 47 |
| 3.7 | SIMS and SNMS Measurements of Nanoparticle Precursor Layers | 47 |
| 3.8 | 3D-Microscope and SEM Pictures of Sputtered Precursors — Time | 49 |
| 3.9 | Roughness of Sputtered Precursors | 51 |
| 3.10 | Mapped Thickness of Sputtered Precursor | 51 |
| 3.11 | Composition of Sputtered Precursor | 52 |
| | | |
| 4.1 | Tube Furnace by Carbolite | 56 |
| 4.2 | Schematic Selenisation Set-Up | 56 |
| 4.3 | Slide Carrier with Samples and Selenium Source | 57 |
| 4.4 | Temperature Profiles Reference Selenisation | 60 |
| 4.5 | SEM Picture of a Gallium-containing Solar cell (DB Precursor, TF Selenisation) | 61 |
| 4.6 | Characteristics of Tube Furnace Selenised DB Ga-Containing Precursor | 61 |

| | | |
|------|--|-----|
| 4.7 | Characteristics of Tube Furnace Selenised DB Ga-Free Precursor | 63 |
| 4.8 | $I-V$ - Characteristics of Different Selenisation Processes - DB | 65 |
| 4.9 | $I-V$ - Characteristics of Metall Salt Based Solar Cells | 66 |
| 4.10 | XRD and SEM of Selenised Nanoparticle Precursor Layers | 67 |
| 4.11 | $I-V$ - Characteristics of Different Selenisation Processes — SP | 69 |
| 4.12 | Se to Metals Ratio Profiles for Selenised Sputtered Precursors | 71 |
| 4.13 | Ga to Ga and In Ratio (GGI) Profiles for Selenised Sputtered Precursors | 72 |
| 4.14 | $I-V$ - Characteristics of Sputtered Precursors — HV and TF | 73 |
| | | |
| 5.1 | Crystal Structure of MoSe_2 | 78 |
| 5.2 | XRD Spectra of Selenised Mo Layers Sputtered with Different Parameters | 80 |
| 5.3 | XRD Measurements for Selenised Mo Layers — Different Sputter Pressure | 82 |
| 5.4 | XRD Measurements for Selenised Mo Layers — Different Sputter Atmosphere | 83 |
| 5.5 | XRD Spectra for Different Selenisation Pressure and Different Sputter Pressure | 85 |
| 5.6 | XRD Measurements for Selenised Mo Layers — Different Selenisation T | 86 |
| | | |
| 6.1 | XRD Spectra of Selenized Mo under Sputtered CIG | 89 |
| 6.2 | XRD Spectra of Selenized Mo under Doctor Bladed Precursor | 91 |
| 6.3 | XRD Spectra of MoSe_2 — Sputtered Precursors Selenised in Vacuum | 92 |
| 6.4 | XRD Spectra of MoSe_2 — Sputtered Precursors | 94 |
| | | |
| 7.1 | Fabrication Flow Chart of Samples with Additional Carbon Layer | 98 |
| 7.2 | CIGS References With Various Layer Thicknesses | 99 |
| 7.3 | Average of Maximum Efficiencies for Each Reference Sample | 100 |
| 7.4 | j_{sc} and V_{oc} of Reference Samples With Different CIGS Thicknesses | 101 |
| 7.5 | $I-V$ Characteristics for Reference Samples | 101 |
| 7.6 | SEM Picture of Gallium-Containing Carbon Layer | 103 |
| 7.7 | SIMS Measurement of CIGS and Carbon Layer | 103 |
| 7.8 | Gallium-Containing Carbon Layers with Various Thicknesses | 105 |
| 7.9 | Gallium-Free Carbon Layers with Various Thicknesses | 106 |
| 7.10 | Cell Efficiency Normalised to Maximum Reference Efficiency for 950 nm CIGS | 106 |
| 7.11 | Cell Efficiency Normalised to Maximum Reference Efficiency for 500 nm CIGS | 107 |
| 7.12 | Cell Efficiency Normalised to Maximum Reference Efficiency for 230 nm CIGS | 107 |
| 7.13 | Comparison of $I-V$ characteristics for Different Carbon Layer Thickness | 109 |
| 7.14 | Varying CIGS Layer Thickness on Carbon Layers | 110 |
| 7.15 | Ratio of Max. Efficiency Values for Cells with Carbon Layer to Reference Cells | 111 |
| 7.16 | $I-V$ Characteristics of the Best Cells for the 230 nm CIGS Deposition Run | 112 |
| 7.17 | Simulated $I-V$ Characteristics of Ref. Cell and Cell with Add. Carbon Layer | 116 |

| | | |
|-----|---|-----|
| A.1 | Overview of the Simulated Solar Cell Structure | 122 |
| A.2 | Simulation Parameters for the CIGS Layer | 123 |
| A.3 | Defect Parameters Used for SCAPS Simulation of CIGS Layer | 124 |
| A.4 | Composition Grading Used for SCAPS Simulation of CIGS Layer | 125 |
| A.5 | Parameters Used for SCAPS Simulation of Back Contact | 126 |

Bibliography

- [1] Nathan S. Lewis. Toward cost-effective solar energy use. *Science*, 315(5813):798–801, 2007. doi: 10.1126/science.1137014.
- [2] Philip Jackson, Roland Würz, Dimitrios Hariskos, Erwin Lotter, Wolfram Witte, and Michael Powalla. Effects of heavy alkali elements in Cu(In,Ga)Se₂ solar cells with efficiencies up to 22.6%. *Phys. Stat. Sol. (RRL)*, 10(8):583–586, 2016. ISSN 1862-6270. doi: 10.1002/pssr.201600199.
- [3] Philip Jackson, Dimitrios Hariskos, Roland Würz, Oliver Kiowski, Andreas Bauer, Theresa Magorian Friedlmeier, and Michael Powalla. Properties of Cu(In,Ga)Se₂ solar cells with new record efficiencies up to 21.7%. *Phys. Stat. Sol. (RRL)*, 9(1):28–31, 2015. ISSN 1862-6270. doi: 10.1002/pssr.201409520.
- [4] Martin A. Green, Keith Emery, Yoshihiro Hishikawa, Wilhelm Warta, Ewan D. Dunlop, Dean H. Levi, and Anita W. Y. Ho-Baillie. Solar cell efficiency tables (version 49). *Prog. Photovoltaics Res. Appl.*, 25(1):3–13, 2017. ISSN 1099-159X. doi: 10.1002/pip.2855. PIP-16-252.
- [5] B. Dimmler. CIGS and CdTe based thin film PV modules, an industrial revolution. *Conf. Rec. 38th IEEE Photovolt. Spec. Conf.*, pages 002494–002499, June 2012. ISSN 0160-8371. doi: 10.1109/PVSC.2012.6318101.
- [6] J. Palm, T. Dalibor, R. Lechner, S. Pohlner, R. Verma, R. Dietmüller, A. Heiß, H. Vogt, and F. Karg. Cd-free CIS thin film solar modules at 17% efficiency. *Proceedings 29th European Photovoltaic Solar Energy Conference*, pages 1433 – 1438, 2014. doi: 10.4229/EUPVSEC20142014-3AO.4.5.
- [7] Erik Wallin, Ulf Malm, Tobias Jarmar, Marika Edoff, Olle Lundberg, and Lars Stolt. World-record Cu(In,Ga)Se₂-based thin-film sub-module with 17.4% efficiency. *Prog. Photovoltaics Res. Appl.*, 20(7):851–854, 2012. ISSN 1099-159X. doi: 10.1002/pip.2246.

- [8] S. Hegedus. Thin film solar modules: The low cost, high throughput and versatile alternative to Si wafers. *Prog. Photovoltaics Res. Appl.*, 14(5):393, 2006. doi: 10.1002/pip.704.
- [9] Neelkanth G. Dhere. Toward GW/year of CIGS production within the next decade. *Sol. Energy Mater. Sol. Cells*, 91(15-16):1376–1382, 2007. ISSN 0927-0248. doi: 10.1016/j.solmat.2007.04.003.
- [10] S. Niki, M. Contreras, I. Repins, M. Powalla, K. Kushiya, S. Ishizuka, and K. Matsubara. CIGS absorbers and processes. *Prog. Photovoltaics Res. Appl.*, 18(6):453–466, 2010. ISSN 1099-159X. doi: 10.1002/pip.969.
- [11] S. Oktik. Low cost, non-vacuum techniques for the preparation of thin/thick films for photovoltaic applications. *Progress in Crystal Growth and Characterization*, 17(3):171–240, 1988. ISSN 0146-3535. doi: 10.1016/0146-3535(88)90006-8.
- [12] M. Kaelin, D. Rudmann, and A. N. Tiwari. Low cost processing of CIGS thin film solar cells. *Sol. Energy*, 77:749, 2004. doi: 10.1016/j.solener.2004.08.015.
- [13] Teodor Todorov and David B. Mitzi. Direct liquid coating of chalcopyrite light-absorbing layers for photovoltaic devices. *European Journal of Inorganic Chemistry*, 2010(1):17–28, 2010. doi: 10.1002/ejic.200900837.
- [14] J. Palm, V. Probst, W. Stetter, R. Toelle, S. Visbeck, H. Calwer, T. Niesen, H. Vogt, O. Hernández, M. Wendl, and F. H. Karg. CIGSSe thin film PV modules: from fundamental investigations to advanced performance and stability. *Thin Solid Films*, 451-452: 544, 2004. doi: 10.1016/j.tsf.2003.10.160.
- [15] Ken Zweibel. Issues in thin film PV manufacturing cost reduction. *Sol. Energy Mater. Sol. Cells*, 59(1-2):1–18, 1999. ISSN 0927-0248. doi: 10.1016/S0927-0248(99)00019-7.
- [16] C. J. Hibberd, E. Chassaing, W. Liu, D. B. Mitzi, D. Lincot, and A. N. Tiwari. Non-vacuum methods for formation of Cu(In,Ga)(Se,S)₂ thin film photovoltaic absorbers. *Prog. Photovoltaics Res. Appl.*, 18(6):434 – 452, 2009. doi: 10.1002/pip.914.
- [17] Frederik C. Krebs. Fabrication and processing of polymer solar cells: A review of printing and coating techniques. *Sol. Energy Mater. Sol. Cells*, 93:394–412, 2009. doi: 10.1016/j.solmat.2008.10.004.
- [18] M. Kaelin, D. Rudmann, F. Kurdesau, H. Zogg, T. Meyer, and A. N. Tiwari. Low-cost CIGS solar cells by paste coating and selenization. *Thin Solid Films*, 480-481:486, 2005. doi: 10.1016/j.tsf.2004.11.007.

- [19] Jan Ungelenk, Veronika Haug, Aina Quintilla, and Erik Ahlswede. CuInSe₂ low-cost thin-film solar cells made from commercial elemental metallic nanoparticles. *Phys. Stat. Sol. (RRL)*, 4(3-4):58–60, 2010. doi: 10.1002/pssr.200903418.
- [20] Edmon Becquerel. Memoire sur les effets électriques produits sous l'influence des rayons solaires. *C. R. Acad. Sci.*, 9:561, 1839.
- [21] William Shockley. The theory of p-n junctions in semiconductors and p-n junction transistors. *Bell Syst. Tech. J.*, 28:435, July 1949.
- [22] J. Bardeen and W. H. Brattain. Physical principles involved in transistor action. *Phys. Rev.*, 75(8):1208–1225, Apr 1949. doi: 10.1103/PhysRev.75.1208.
- [23] James Clerk Maxwell. A dynamical theory of the electromagnetic field. *Phil. Trans. R. Soc. Lond.*, 155:459–512, 1865.
- [24] J.D. Jackson. *Classical electrodynamics*. Wiley, New York, 1975. ISBN 9780471431329.
- [25] Peter Würfel. *Physik der Solarzelle*. Spektrum Akademischer Verlag, Heidelberg, 2000. ISBN 9783827405982.
- [26] U. Rau. Tunneling-enhanced recombination in Cu(In, Ga)Se₂ heterojunction solar cells. *Appl. Phys. Lett.*, 74(1):111–113, 1999. doi: 10.1063/1.122967.
- [27] Robert B. Darling. Current-voltage characteristics of Schottky barrier diodes with dynamic interfacial defect state occupancy. *IEEE Trans. Electron Devices*, 43(7):1153–1160, Jul 1996. ISSN 0018-9383. doi: 10.1109/16.502427.
- [28] A. Niemegeers, M. Burgelman, R. Herberholz, U. Rau, D. Hariskos, and H.-W. Schock. Model for electronic transport in Cu(In,Ga)Se₂ solar cells. *Prog. Photovoltaics Res. Appl.*, 6(6):407, 1998. doi: 10.1002/(SICI)1099-159X(199811/12)6:6<407::AID-PIP230>3.0.CO;2-U.
- [29] Markus Gloeckler, Caroline R. Jenkins, and James R. Sites. Explanation of light/dark superposition failure in CIGS solar cells. *Mater. Res. Soc. Symp. Proc.*, 763:B5.20 / 231, 2003. doi: 10.1557/PROC-763-B5.20.
- [30] A. R. Beattie and P. T. Landsberg. Auger effect in semiconductors. *Proc. Roy. Soc. Lond. Math. Phys. Sci.*, 249(1256):16–29, 1959. doi: 10.1098/rspa.1959.0003.
- [31] W. Shockley and W. T. Read jr. Statistics of the recombinations of holes and electrons. *Phys. Rev.*, 87(5):835–842, Sep 1952. doi: 10.1103/PhysRev.87.835.

- [32] R. N. Hall. Electron-hole recombination in germanium. *Phys. Rev.*, 87(2):387, Jul 1952. doi: 10.1103/PhysRev.87.387.
- [33] D. J. Fitzgerald and A. S. Grove. Surface recombination in semiconductors. *Surf. Sci.*, 9(2):347–369, 1968. ISSN 0039-6028. doi: 10.1016/0039-6028(68)90182-9.
- [34] Erees Queen B. Macabebe, Charles J. Sheppard, Vivian Alberts, and E. Ernest van Dyk. Effects of different selenization conditions on the device parameters of CuIn(Se,S)₂ solar cells. *Thin Solid Films*, 517(7):2380–2382, 2009. ISSN 0040-6090. doi: 10.1016/j.tsf.2008.11.010.
- [35] Barbara Werner, Włodzimierz Kołodenny, Mariusz Prorok, Andrzej Dziedzic, and Tadeusz Żdanowicz. Electrical modeling of CIGS thin-film solar cells working in natural conditions. *Sol. Energy Mater. Sol. Cells*, 515(9):2583 – 2587, 2011. ISSN 0927-0248. doi: 10.1016/j.solmat.2011.03.014.
- [36] Enrico Jarzembowski, Matthias Maiberg, Florian Obereigner, Kai Kaufmann, Stephan Krause, and Roland Scheer. Optical and electrical characterization of Cu(In,Ga)Se₂ thin film solar cells with varied absorber layer thickness. *Thin Solid Films*, 576(0):75 – 80, 2015. ISSN 0040-6090. doi: 10.1016/j.tsf.2015.01.004.
- [37] Neil W. Ashcroft and N. David Mermin. *Solid State Physics*. Cengage Learning Services, Hampshire, UK, 1976. ISBN 0030839939.
- [38] Charles Kittel. *Introduction to Solid State Physics*. John Wiley & Sons, Inc., New Jersey, 8th edition, November 2004. ISBN 047141526X.
- [39] Harry Hahn, Günter Frank, Wilhelm Klingler, Anne-Dorothee Meyer, and Georg Störger. Untersuchungen über ternäre Chalkogenide. V. Über einige ternäre Chalkogenide mit Chalkopyritstruktur. *Zeitschrift für anorganische und allgemeine Chemie*, 271(3-4):153–170, 1953. doi: 10.1002/zaac.19532710307.
- [40] Uwe Rau. Electronic properties of Cu(In,Ga)Se₂ thin-film solar cells – an update. *Adv. Solid State Phys.*, 44:27, 2004. doi: 10.1007/b95888.
- [41] T. Goedecke, T. Haalboom, and F. Ernst. Phase equilibria of Cu-In-Se. I. Stable states and nonequilibrium states of the In₂Se₃-Cu₂Se subsystem. *Zeitschrift fuer Metallkunde*, 91(8):622–634, 2000.
- [42] T. Goedecke, T. Haalboom, and F. Ernst. Phase equilibria of Cu-In-Se. II. The In-In₂Se₃-Cu₂Se-Cu subsystem. *Zeitschrift fuer Metallkunde*, 91(8):635–650, 2000.

- [43] T. Goedecke, T. Haalboom, and F. Ernst. Phase equilibria of Cu-In-Se. III. The In_2Se_3 -Se-Cu₂Se subsystem. *Zeitschrift fuer Metallkunde*, 91(8):651–662, 2000.
- [44] Roland Scheer and Hans-Werner Schock. *Chalcogenide Photovoltaics: Physics, Technologies, and Thin Film Devices*. Wiley-VCH, Weinheim, 2011.
- [45] R. Herberholz, U. Rau, H. W. Schock, T. Haalboom, T. Gödecke, F. Ernst, C. Beilharz, K. W. Benz, and D. Cahen. Phase segregation, Cu migration and junction formation in Cu(In, Ga)Se₂. *The European Physical Journal Applied Physics*, 6:131–139, 5 1999. ISSN 1286-0050. doi: 10.1051/epjap:1999162.
- [46] G. Hanna, T. Glatzel, S. Sadewasser, N. Ott, H. P. Strunk, U. Rau, and J. H. Werner. Texture and electronic activity of grain boundaries in Cu(In,Ga)Se₂ thin films. *Appl. Phys. A*, 82:1, 2006. doi: 10.1007/s00339-005-3411-1.
- [47] Martin A. Green, Keith Emery, Yoshihiro Hishikawa, Wilhelm Warta, and Ewan D. Dunlop. Solar cell efficiency tables (version 45). *Prog. Photovoltaics Res. Appl.*, 23(1):1–9, 2015. ISSN 1099-159X. doi: 10.1002/pip.2573.
- [48] Michael Powalla, Philip Jackson, Dimitri Hariskos, Stefan Paetel, Wolfram Witte, Roland Würz, Erwin Lotter, Richard Menner, and Wiltraud Wischmann. CIGS thin-film solar cells with an improved efficiency of 20.8 %. *29th European Photovoltaic Solar Energy Conference*, 3AO.4.2, 2014.
- [49] Adrian Chirilă, Stephan Buecheler, Fabian Pianezzi, Patrick Blösch, Christina Gretener, Alexander R. Uhl, Carolin Fella, Lukas Kranz, Julian Perrenoud, Sieghard Seyrling, Rajneesh Verma, Shiro Nishiwaki, Yaroslav E. Romanyuk, Gerhard Bilger, and Ayodhya N. Tiwari. Highly efficient Cu(In,Ga)Se₂ solar cells grown on flexible polymer films. *Nature Materials*, 10(11):857–861, November 2011. ISSN 1476-1122. doi: 10.1038/nmat3122.
- [50] Ingrid Repins, Miguel A. Contreras, Brian Egaas, Clay DeHart, John Scharf, Craig L. Perkins, Bobby To, and Rommel Noufi. Short communication: Accelerated publication 19.9%-efficient ZnO/CdS/CuInGaSe₂ solar cell with 81.2% fill factor. *Prog. Photovoltaics Res. Appl.*, 16:235, 2008. doi: 10.1002/pip.822.
- [51] C. H. Champness, H. Du, and I. Shih. Measurements on monocrystalline CuInSe₂ cells. *Conf. Rec. 31st IEEE Photovolt. Spec. Conf.*, pages 402–405, 2005. doi: 10.1109/PVSC.2005.1488154.
- [52] Susanne Siebentritt, Tobias Eisenbarth, Angus Rockett, Jürgen Albert, Peter Schubert-Bischoff, and Martha Ch. Lux-Steiner. Epitaxially grown single grain boundaries in

- chalcopyrites. *J. Phys.: Condens. Matter*, 19(1):016004, 2007. doi: 10.1088/0953-8984/19/1/016004.
- [53] Clas Persson and Alex Zunger. Anomalous grain boundary physics in polycrystalline CuInSe_2 : The existence of a hole barrier. *Phys. Rev. Lett.*, 91(26):266401, 2003. doi: 10.1103/PhysRevLett.91.266401.
- [54] C. Lei, C. M. Li, A. Rockett, and I. M. Robertson. Grain boundary compositions in Cu(InGa)Se_2 . *J. Appl. Phys.*, 101(2):024909, 2007. doi: 10.1063/1.2426962.
- [55] Chun-Ming Li, Chang-Hui Lei, Ian M. Robertson, and Angus Rockett. Microstructural and microchemical analysis of chalcopyrite Cu(In,Ga)Se_2 films. *Mater. Res. Soc. Symp. Proc.*, 763:B4.2 / 169, 2003. doi: 10.1557/PROC-763-B4.2.
- [56] C.-S. Jiang, R. Noufi, J. A. AbuShama, K. Ramanathan, H. R. Moutinho, J. Pankow, and M. M. Al-Jassim. Local built-in potential on grain boundary of Cu(In,Ga)Se_2 thin films. *Appl. Phys. Lett.*, 84(18):3477, 2004. doi: 10.1063/1.1737796.
- [57] Manuel J. Romero, Kannan Ramanathan, Miguel A. Contreras, Mowafak M. Al-Jassim, Rommel Noufi, and Peter Sheldon. Cathodoluminescence of Cu(In,Ga)Se_2 thin films used in high-efficiency solar cells. *Appl. Phys. Lett.*, 83(23):4770, 2003. doi: 10.1063/1.1631083.
- [58] Uwe Rau, Kurt Taretto, and Susanne Siebentritt. Grain boundaries in Cu(In,Ga)(Se,S)_2 thin-film solar cells. *Appl. Phys. A*, 96(1):221–234, July 2009. doi: 10.1007/s00339-008-4978-0.
- [59] D. Wolf. Atomic-level geometry of crystalline interfaces. In Dieter Wolf and Sidney Yip, editors, *Materials interfaces – atomic-level structure and properties*, chapter 1, page 1. Chapman & Hall, London, 1992.
- [60] M. G. Norton and C. B. Carter. Grain and interface boundaries in ceramics and ceramics composites. In Dieter Wolf and Sidney Yip, editors, *Materials interfaces – atomic-level structure and properties*, chapter 4, page 151. Chapman & Hall, London, 1992.
- [61] D. Abou-Ras, M. A. Contreras, R. Noufi, and H.-W. Schock. Impact of the Se evaporation rate on the microstructure and texture of Cu(In,Ga)Se_2 thin films for solar cells. *Thin Solid Films*, 517(7):2218–2221, 2009. ISSN 0040-6090. doi: 10.1016/j.tsf.2008.10.133.
- [62] D. Abou-Ras, S. Schorr, and H. W. Schock. Grain-size distributions and grain boundaries of chalcopyrite-type thin films. *J. Appl. Cryst.*, 40(5):841–848, Oct 2007. doi: 10.1107/S0021889807032220.

- [63] Susanne Siebentritt, Sascha Sadewasser, Mark Wimmer, Caspar Leendertz, Tobias Eisenbarth, and Martha Ch. Lux-Steiner. Evidence for a neutral grain-boundary barrier in chalcopyrites. *Phys. Rev. Lett.*, 97(14):146601, Oct 2006. doi: 10.1103/PhysRevLett.97.146601.
- [64] Yanfa Yan, C.-S. Jiang, R. Noufi, Su-Huai Wei, H. R. Moutinho, and M. M. Al-Jassim. Electrically benign behavior of grain boundaries in polycrystalline CuInSe₂ films. *Phys. Rev. Lett.*, 99(23):235504, Dec 2007. doi: 10.1103/PhysRevLett.99.235504.
- [65] Yanfa Yan, K. M. Jones, C. S. Jiang, X. Z. Wu, R. Noufi, and M. M. Al-Jassim. Understanding the defect physics in polycrystalline photovoltaic materials. *Physica B*, 401-402: 25–32, 2007. ISSN 0921-4526. doi: 10.1016/j.physb.2007.08.106.
- [66] David Cahen and Rommel Noufi. Defect chemical explanation for the effect of air anneal on CdS/CuInSe₂ solar cell performance. *Appl. Phys. Lett.*, 54(6):558–560, 1989. doi: 10.1063/1.100930.
- [67] Leeor Kronik, David Cahen, and Hans Werner Schock. Effects of sodium on polycrystalline Cu(In,Ga)Se₂ and its solar cell performance. *Adv. Mater.*, 10:31–36, 1998. doi: 10.1002/(SICI)1521-4095(199801)10:1<31::AID-ADMA31>3.0.CO;2-3.
- [68] Leeor Kronik, Uwe Rau, Jean-François Guillemoles, Dieter Braunger, Hans-Werner Schock, and David Cahen. Interface redox engineering of Cu(In,Ga)Se₂ - based solar cells: oxygen, sodium, and chemical bath effects. *Thin Solid Films*, 361-362:353–359, 2000. ISSN 0040-6090. doi: 10.1016/S0040-6090(99)00768-3.
- [69] A. Rockett. The effect of Na in polycrystalline and epitaxial single-crystal CuIn_{1-x}Ga_xSe₂. *Thin Solid Films*, 480-481:2–7, 2005. ISSN 0040-6090. doi: 10.1016/j.tsf.2004.11.038.
- [70] Clas Persson and Alex Zunger. Compositionally induced valence-band offset at the grain boundary of polycrystalline chalcopyrites creates a hole barrier. *Appl. Phys. Lett.*, 87(21):211904, 2005. doi: 10.1063/1.2132537.
- [71] M. J. Hetzer, Y. M. Strzhemechny, M. Gao, M. A. Contreras, A. Zunger, and L. J. Brillson. Direct observation of copper depletion and potential changes at copper indium gallium diselenide grain boundaries. *Appl. Phys. Lett.*, 86(16):162105, 2005. doi: 10.1063/1.1906331.
- [72] Yanfa Yan, R. Noufi, and M. M. Al-Jassim. Grain-boundary physics in polycrystalline CuInSe₂ revisited: Experiment and theory. *Phys. Rev. Lett.*, 96(20):205501, 2006. doi: 10.1103/PhysRevLett.96.205501.

- [73] K. Taretto and U. Rau. Numerical simulation of carrier collection and recombination at grain boundaries in Cu(In,Ga)Se₂ solar cells. *J. Appl. Phys.*, 103(9):094523, 2008. doi: 10.1063/1.2917293.
- [74] A. Romeo, M. Terheggen, D. Abou-Ras, D. L. Bätzner, F.-J. Haug, M. Kaelin, D. Rudmann, and A. N. Tiwari. Development of thin-film Cu(In,Ga)Se₂ and CdTe solar cells. *Prog. Photovoltaics Res. Appl.*, 12:93, 2004. doi: 10.1002/pip.527.
- [75] Franz-Josef Haug. *Development of Cu(In,Ga)Se₂ Superstrate Thin Film Solar Cells*. PhD thesis, Eidgenössische Technische Hochschule Zürich, 2001.
- [76] N. G. Dhere. Present status and future prospects of CIGSS thin film solar cells. *Sol. Energy Mater. Sol. Cells*, 90(15):2181, 2006. doi: 10.1016/j.solmat.2006.02.018.
- [77] K. Orgassa, H. W. Schock, and J. H. Werner. Alternative back contact materials for thin film Cu(In,Ga)Se₂ solar cells. *Thin Solid Films*, 431-432:387–391, 2003. ISSN 0040-6090. doi: 10.1016/S0040-6090(03)00257-8.
- [78] L. Assmann, J. C. Bernède, A. Drici, C. Amory, E. Halgand, and M. Morsli. Study of the Mo thin films and Mo/CIGS interface properties. *Appl. Surf. Sci.*, 246(1-3):159–166, 2005. ISSN 0169-4332. doi: 10.1016/j.apsusc.2004.11.020.
- [79] Mary D. Archer and Robert Hill, editors. *Clean electricity from photovoltaics*, volume 1 of *Series on photoconversion of solar energy*. Imperial College Press, London, 2001. ISBN 1-86094-161-3.
- [80] R. Menner and H. W. Schock. Loss analysis and modelling for high efficiency CuInSe₂ based solar cells. *Proceedings 11th European Photovoltaic Solar Energy Conference*, 1: 834, 1992.
- [81] Lawrence L. Kazmerski, Richard B. Cooper, Francis R. White, and Aubrey J. Merrill. Auger analysis of CdS–CuInSe₂ thin-film solar cells. *IEEE Trans. Electron Devices*, 24(4):496–498, Apr 1977. ISSN 0018-9383. doi: 10.1109/T-ED.1977.18766.
- [82] L. L. Kazmerski, O. Jamjoum, P. J. Ireland, R. A. Mickelsen, and W. S. Chen. Formation, growth, and stability of the CdS/CuInSe₂ interface. *J. Vac. Sci. Technol.*, 21(2):486–490, 1982. doi: 10.1116/1.571744.
- [83] A. Klein, F. Säuberlich, B. Späth, T. Schulmeyer, and D. Kraft. Non-stoichiometry and electronic properties of interfaces. *J. Mater. Sci.*, 42(6):1890–1900, March 2007. doi: 10.1007/s10853-006-1322-y.

- [84] Takashi Minemoto, Yasuhiro Hashimoto, Takuya Satoh, Takayuki Negami, and Hideyuki Takakura. Variable light soaking effect of Cu(In,Ga)Se₂ solar cells with conduction band offset control of window/Cu(In,Ga)Se₂ layers. *Mater. Res. Soc. Symp. Proc.*, 1012:Y07–03, 2007. doi: 10.1557/PROC-1012-Y07-03.
- [85] N. Naghavi, S. Spiering, M. Powalla, B. Cavana, and D. Lincot. High-efficiency copper indium gallium diselenide (CIGS) solar cells with indium sulfide buffer layers deposited by atomic layer chemical vapor deposition (ALCVD). *Prog. Photovoltaics Res. Appl.*, 11:437, 2003. doi: 10.1002/pip.508.
- [86] D. Hariskos, S. Spiering, and M. Powalla. Buffer layers in Cu(In,Ga)Se₂ solar cells and modules. *Thin Solid Films*, 480-481:99–109, June 2005. doi: 10.1016/j.tsf.2004.11.118.
- [87] Vignesh Gowrishankar, Christine K. Luscombe, Michael D. McGehee, and Jean M.J. Fréchet. High-efficiency, Cd-free copper-indium-gallium-diselenide/polymer hybrid solar cells. *Sol. Energy Mater. Sol. Cells*, 91(9):807–812, May 2007. ISSN 0927-0248. doi: 10.1016/j.solmat.2007.01.012.
- [88] C. Hubert, N. Naghavi, A. Etcheberry, O. Roussel, D. Hariskos, M. Powalla, O. Kerrec, and D. Lincot. A better understanding of the growth mechanism of Zn(S,O,OH) chemical bath deposited buffer layers for high efficiency Cu(In,Ga)(S,Se)₂ solar cells. *Phys. Stat. Sol. (a)*, 205(10):2335–2339, 2008. doi: 10.1002/pssa.200879446.
- [89] D. Hariskos, B. Fuchs, R. Menner, N. Naghavi, C. Hubert, D. Lincot, and M. Powalla. The Zn(S,O,OH)/ZnMgO buffer in thin-film Cu(In,Ga)(Se,S)₂-based solar cells part II: Magnetron sputtering of the ZnMgO buffer layer for in-line co-evaporated Cu(In,Ga)Se₂ solar cells. *Prog. Photovoltaics Res. Appl.*, 17(7):479–488, 2009. doi: 10.1002/pip.897.
- [90] C. Hubert, N. Naghavi, O. Roussel, A. Etcheberry, D. Hariskos, R. Menner, M. Powalla, O. Kerrec, and D. Lincot. The Zn(S,O,OH)/ZnMgO buffer in thin film Cu(In,Ga)(S,Se)₂-based solar cells part I: Fast chemical bath deposition of Zn(S,O,OH) buffer layers for industrial application on co-evaporated Cu(In,Ga)Se₂ and electrodeposited CuIn(S,Se)₂ solar cells. *Prog. Photovoltaics Res. Appl.*, 17(7):470–478, 2009. doi: 10.1002/pip.898.
- [91] S. Spiering, L. Bürkert, D. Hariskos, M. Powalla, B. Dimmler, C. Giesen, and M. Heuken. MOCVD indium sulphide for application as a buffer layer in CIGS solar cells. *Thin Solid Films*, 517(7):2328–2331, 2009. ISSN 0040-6090. doi: 10.1016/j.tsf.2008.11.004.
- [92] Tokio Nakada, Masashi Hongo, and Eiji Hayashi. Band offset of high efficiency CBD-ZnS/CIGS thin film solar cells. *Thin Solid Films*, 431-432:242–248, 2003. ISSN 0040-6090. doi: 10.1016/S0040-6090(03)00265-7.

- [93] M. Igalson and C. Platzer-Björkman. The influence of buffer layer on the transient behavior of thin film chalcopyrite devices. *Sol. Energy Mater. Sol. Cells*, 84(1-4):93–103, 2004. ISSN 0927-0248. doi: 10.1016/j.solmat.2004.02.038.
- [94] C. Platzer-Björkman, T. Törndahl, D. Abou-Ras, J. Malmström, J. Kessler, and L. Stolt. Zn(O,S) buffer layers by atomic layer deposition in Cu(In,Ga)Se₂ based thin film solar cells: Band alignment and sulfur gradient. *J. Appl. Phys.*, 100(4):044506, 2006. doi: 10.1063/1.2222067.
- [95] T. M. Friedlmeier, P. Jackson, A. Bauer, D. Hariskos, O. Kiowski, R. Würz, and M. Powalla. Improved photocurrent in Cu(In,Ga)Se₂ solar cells: From 20.8 % to 21.7 % efficiency with CdS buffer and 21.0 % Cd-free. *IEEE Journal of Photovoltaics*, 5(5): 1487–1491, Sept 2015. ISSN 2156-3381. doi: 10.1109/JPHOTOV.2015.2458039.
- [96] Solar Frontier. Solar frontier achieves world record thin-film solar cell efficiency: 22.3 %. Press Release, December 2015. URL <http://www.solar-frontier.com/eng/news/pdf/2015/1208.pdf>.
- [97] R. Takei, H. Tanino, S. Chichibu, and H. Nakanishi. Depth profiles of spatially-resolved Raman spectra of a CuInSe₂-based thin-film solar cell. *J. Appl. Phys.*, 79(5):2793–2795, 1996. doi: 10.1063/1.361095.
- [98] Takahiro Wada, Naoki Kohara, Takayuki Negami, and Mikihiro Nishitani. Chemical and structural characterization of Cu(In,Ga)Se₂/Mo interface in Cu(In,Ga)Se₂ solar cells. *Jpn. J. Appl. Phys.*, 35(Part 2, No. 10A):L1253–L1256, 1996. doi: 10.1143/JJAP.35.L1253.
- [99] Shiro Nishiwaki, Naoki Kohara, Takayuki Negami, and Takahiro Wada. MoSe₂ layer formation at Cu(In,Ga)Se₂/Mo interfaces in high efficiency Cu(In_{1-x}Ga_x)Se₂ solar cells. *Jpn. J. Appl. Phys.*, 37(Part 2, No. 1A/B):L71–L73, 1998. doi: 10.1143/JJAP.37.L71.
- [100] Jean-Francois Guillemoles, Leeor Kronik, David Cahen, Uwe Rau, Axel Jananek, and Hans-Werner Schock. Stability issues of Cu(In,Ga)Se₂-based solar cells. *J. Phys. Chem. B*, 104:4849, 2000. doi: 10.1021/jp993143k.
- [101] Hiroki Sato, Toshio Hama, Esko Niemi, Yukimi Ichikawa, and Hiroshi Sakai. Formation of CuIn(Ga)Se₂ thin films by selenization and application to solar cells. *Jpn. J. Appl. Phys.*, 32S3:50–53, 1993. doi: 10.1143/JJAPS.32S3.50.
- [102] P. E. Russell, O. Jamjoom, R. K. Ahrenkiel, L. L. Kazmerski, R. A. Mickelsen, and W. S. Chen. Properties of the Mo-CuInSe₂ interface. *Appl. Phys. Lett.*, 40(11):995–997, 1982. doi: 10.1063/1.92955.

- [103] R. J. Matson, O. Jamjoum, A. D. Buonaquisti, P. E. Russell, L. L. Kazmerski, P. Sheldon, and R. K. Ahrenkiel. Metal contacts to CuInSe₂. *Sol. Cells*, 11(3):301–305, 1984. ISSN 0379-6787. doi: 10.1016/0379-6787(84)90019-X.
- [104] W. N. Shafarman and J. E. Phillips. Direct current-voltage measurements of the Mo/CuInSe₂ contact on operating solar cells. *Conf. Rec. 25th IEEE Photovolt. Spec. Conf.*, 1:917–919, May 1996. doi: 10.1109/PVSC.1996.564278.
- [105] T. Wada, N. Kohara, S. Nishiwaki, and T. Negami. Characterization of the Cu(In,Ga)Se₂/Mo interface in CIGS solar cells. *Thin Solid Films*, 387(1-2):118–122, 2001. ISSN 0040-6090. doi: 10.1016/S0040-6090(00)01846-0.
- [106] R. Würz, D. Fuertes Marron, A. Meeder, A. Rumberg, S. M. Babu, Th. Schedel-Niedrig, U. Bloeck, P. Schubert-Bischoff, and M. Ch. Lux-Steiner. Formation of an interfacial MoSe₂ layer in CVD grown CuGaSe₂ based thin film solar cells. *Thin Solid Films*, 431: 398, 2003. doi: 10.1016/S0040-6090(03)00261-X.
- [107] Daniel Abou-Ras, Debashis Mukherji, Gernot Kostorz, David Brémaud, Marc Kälin, Dominik Rudmann, Max Döbeli, and Ayodhya N. Tiwari. Dependence of the MoSe₂ formation on the Mo orientation and the Na concentration for Cu(In,Ga)Se₂ thin-film solar cells. *Mater. Res. Soc. Symp. Proc.*, 865:F8.1.1, 2005. doi: 10.1557/PROC-865-F8.1.
- [108] L. Weinhardt, M. Blum, M. Bär, C. Heske, O. Fuchs, E. Umbach, J. D. Denlinger, K. Ramanathan, and R. Noufi. Chemical properties of the Cu(In,Ga)Se₂/Mo/glass interfaces in thin film solar cells. *Thin Solid Films*, 515(15):6119–6122, 2007. ISSN 0040-6090. doi: 10.1016/j.tsf.2006.12.109.
- [109] D. Fuertes Marron, A. Meeder, S. Sadewasser, R. Wurz, C. A. Kaufmann, Th. Glatzel, Th. Schedel-Niedrig, and M. Ch. Lux-Steiner. Lift-off process and rear-side characterization of CuGaSe₂ chalcopyrite thin films and solar cells. *J. Appl. Phys.*, 97(9):094915, 2005. doi: 10.1063/1.1891274.
- [110] Liina Kaupmees, Mare Altosaar, Olga Volobujeva, and Paul Barvinschi. Study of Mo selenisation process on different Mo substrates. *Mater. Res. Soc. Symp. Proc.*, 1165: M08–01, 2009. doi: 10.1557/PROC-1165-M08-01.
- [111] Hans Werner Schock and Uwe Rau. The role of structural properties and defects for the performance of Cu-chalcopyrite-based thin-film solar cells. *Physica B*, 308-310:1081 – 1085, 2001. ISSN 0921-4526. doi: 10.1016/S0921-4526(01)00863-8.

- [112] J. A. Wilson and A. D. Yoffe. The transition metal dichalcogenides discussion and interpretation of the observed optical, electrical and structural properties. *Adv. Phys.*, 18(73): 193–335, 1969. doi: 10.1080/00018736900101307.
- [113] W. Jaegermann and H. Tributsch. Interfacial properties of semiconducting transition metal chalcogenides. *Progress in Surface Science*, 29(1-2):1–167, 1988. ISSN 0079-6816. doi: 10.1016/0079-6816(88)90015-9.
- [114] Kay Orgassa. *Coherent optical analysis of the ZnO/Cd/CIGS thin film solar cell*. PhD thesis, Universität Stuttgart, 2004.
- [115] F. Erfurth, Z. Jehl, M. Bouttemy, N. Dahan, P. Tran-Van, I. Gerard, A. Etcheberry, J.-J. Greffet, M. Powalla, G. Voorwinden, D. Lincot, J.F. Guillemoles, and N. Naghavi. Mo/Cu(In,Ga)Se₂ back interface chemical and optical properties for ultrathin CIGSe solar cells. *Appl. Surf. Sci.*, 258(7):3058–3061, 2011. ISSN 0169-4332. doi: 10.1016/j.apsusc.2011.11.037.
- [116] Sutichai Chaisitsak, Akira Yamada, and Makoto Konagai. Preferred orientation control of Cu(In_{1-x}Ga_x)Se₂ ($x \approx 0.28$) thin films and its influence on solar cell characteristics. *Jpn. J. Appl. Phys.*, 41(Part 1, No. 2A):507–513, 2002. doi: 10.1143/JJAP.41.507.
- [117] Martin A. Green, Keith Emery, Yoshihiro Hishikawa, Wilhelm Warta, and Ewan D. Dunlop. Solar cell efficiency tables (version 42). *Progress in Photovoltaics: Research and Applications*, 21(5):827–837, 2013. ISSN 1099-159X. doi: 10.1002/pip.2404.
- [118] Philip Jackson, Dimitrios Hariskos, Erwin Lotter, Stefan Paetel, Roland Würz, Richard Menner, Wiltraud Wischmann, and Michael Powalla. New world record efficiency for Cu(In,Ga)Se₂ thin-film solar cells beyond 20%. *Prog. Photovoltaics Res. Appl.*, 19: 894–897, 2011. ISSN 1099-159X. doi: 10.1002/pip.1078.
- [119] Kannan Ramanathan, Miguel A. Contreras, Craig L. Perkins, Sally Asher, Falah S. Haseen, James Keane, David Young, Manuel Romero, Wyatt Metzger, Rommel Noufi, James Ward, and Anna Duda. Properties of 19.2% efficiency ZnO/CdS/CuInGaSe₂ thin-film solar cells. *Prog. Photovoltaics Res. Appl.*, 11(4):225, 2003. doi: 10.1002/pip.494.
- [120] Philip Jackson, Roland Würz, Uwe Rau, Julian Mattheis, Matthias Kurth, Thomas Schlötzer, Gerhard Bilger, and Jürgen H. Werner. High quality baseline for high efficiency, Cu(In_{1-x}Ga_x)Se₂ solar cells. *Prog. Photovoltaics Res. Appl.*, 15(6):507–519, 2007. doi: 10.1002/pip.757.

- [121] M. Powalla, G. Voorwinden, D. Hariskos, P. Jackson, and R. Kniese. Highly efficient CIS solar cells and modules made by the co-evaporation process. *Thin Solid Films*, 517(7):2111–2114, 2009. ISSN 0040-6090. doi: 10.1016/j.tsf.2008.10.126.
- [122] Andrew M. Gabor, John R. Tuttle, David S. Albin, Miguel A. Contreras, Rommel Noufi, and Allen M. Hermann. High-efficiency $\text{CuIn}_x\text{Ga}_{1-x}\text{Se}_2$ solar cells made from $(\text{In}_x\text{Ga}_{1-x})_2\text{Se}_3$ precursor films. *Appl. Phys. Lett.*, 65(2):198–200, 1994. doi: 10.1063/1.112670.
- [123] John R. Tuttle, Miguel Contreras, Andrew Tennant, David Albin, and Rommel Noufi. High efficiency thin-film $\text{Cu}(\text{In,Ga})\text{Se}_2$ -based photovoltaic devices: progress towards a universal approach to absorber fabrication. *Conf. Rec. 23rd IEEE Photovolt. Spec. Conf.*, pages 415–421, May 1993. doi: 10.1109/PVSC.1993.347146.
- [124] Wen S. Chen, J. M. Stewart, W. E. Devaney, R. A. Mickelsen, and B. J. Stanbery. Thin film CuInGaSe_2 cell development. *Conf. Rec. 23rd IEEE Photovolt. Spec. Conf.*, pages 422–425, May 1993. doi: 10.1109/PVSC.1993.347145.
- [125] Jonas Hedström, Hakan Ohlsen, Marika Bodegard, Angela Kylner, Lars Stolt, Dimitri Hariskos, Martin Ruckh, and Hans-Werner Schock. $\text{ZnO}/\text{CdS}/\text{Cu}(\text{In,Ga})\text{Se}_2$ thin film solar cells with improved performance. *Conf. Rec. 23rd IEEE Photovolt. Spec. Conf.*, pages 364–371, May 1993. doi: 10.1109/PVSC.1993.347154.
- [126] M. Powalla and B. Dimmler. Process development of high performance CIGS modules for mass production. *Thin Solid Films*, 387(1-2):251, 2001. doi: 10.1016/S0040-6090(00)01708-9.
- [127] M. Powalla, M. Cemernjak, J. Eberhardt, F. Kessler, R. Kniese, H.-D. Mohring, and B. Dimmler. Large-area CIGS modules: Pilot line production and new developments. *Sol. Energy Mater. Sol. Cells*, 90(18-19):3158, 2006. doi: 10.1016/j.solmat.2006.06.052.
- [128] M. Marudachalam, H. Hichri, R. Klenk, R. W. Birkmire, W. N. Shafarman, and J. M. Schultz. Preparation of homogeneous $\text{Cu}(\text{InGa})\text{Se}_2$ films by selenization of metal precursors in H_2Se atmosphere. *Appl. Phys. Lett.*, 67(26):3978–3980, 1995. doi: 10.1063/1.114424.
- [129] K. T. Ramakrishna Reddy, I. Forbes, R. W. Miles, M. J. Carter, and P. K. Dutta. Growth of high-quality CuInSe_2 films by selenising sputtered Cu-In bilayers using a closed graphite box. *Mater. Lett.*, 37(1-2):57, 1998. doi: 10.1016/S0167-577X(98)00066-4.

- [130] D. Bhattacharyya, I. Forbes, F. O. Adurodija, and M. Carter. Formation of CuInSe_2 by the selenization of sputtered Cu/In layers. *J. Mater. Sci.*, 32:1889–1894, April 1997. doi: 10.1023/A:1018517209661.
- [131] F. O. Adurodija, J. Song, K. H. Yoon, S. K. Kim, S. D. Kim, S. H. Kwon, and B. T. Ahn. Preparation of CuInSe_2 thin films by selenization of co-sputtered Cu–In precursors. *J. Mater. Sci. - Mater. Electron.*, 9(5):361–366, October 1998. doi: 10.1023/A:1008936210166.
- [132] G. S. Chen, J. C. Yang, Y. C. Chan, L. C. Yang, and Welson Huang. Another route to fabricate single-phase chalcogenides by post-selenization of cu–in–ga precursors sputter deposited from a single ternary target. *Sol. Energy Mater. Sol. Cells*, 93:1351–1355, 2009. doi: 10.1016/j.solmat.2009.02.014.
- [133] Raquel Caballero, Cecilia Guillén, and Rocío Bayón. Alloying and selenization of Cu–In stacked layers evaporated onto large areas. *Mater. Res. Soc. Symp. Proc.*, 668:H8.2, 2001. doi: 10.1016/j.solmat.2004.05.019.
- [134] C. Guillén and J. Herrero. Structure, morphology and photoelectrochemical activity of CuInSe_2 thin films as determined by the characteristics of evaporated metallic precursors. *Sol. Energy Mater. Sol. Cells*, 73(2):141–149, 2002. ISSN 0927-0248. doi: 10.1016/S0927-0248(01)00119-2.
- [135] J. Bekker, V. Alberts, and M. J. Witcomb. Influence of selenization techniques on the reaction kinetics of chalcopyrite thin films. *Thin Solid Films*, 387:40–43, May 2001. doi: 10.1016/S0040-6090(01)00797-0.
- [136] Satoshi Yamanaka, Brian E. McCandless, and Robert W. Birkmire. Reaction chemistry of CuInSe_2 formation by selenization using elemental Se. *Conf. Rec. 23rd IEEE Photovolt. Spec. Conf.*, pages 607–612, 1993. doi: 10.1109/PVSC.1993.347024.
- [137] Katsumi Kushiya, Akira Shimizu, Koki Saito, Akira Yamada, and Makoto Konagai. Development of high-efficiency $\text{CuIn}_x\text{Ga}_{1-x}\text{Se}_2$ thin-film solar cells by selenization with elemental Se vapor in vacuum. *Photovoltaic Energy Conversion, Conference Record of the 24th IEEE Photovoltaic Specialists Conference - 1994 IEEE 1st World Conference on*, 1:87, May 1994. doi: 10.1109/WCPEC.1994.519814.
- [138] F. B. Dejene and V. Alberts. Structural and optical properties of homogeneous Cu(In,Ga)Se_2 thin films prepared by thermal reaction of InSe/Cu/GaSe alloys with elemental Se vapour. *J. Phys. D: Appl. Phys.*, 38(1):22–25, 2005. doi: 10.1088/0022-3727/38/1/005.

- [139] Wei Li, Yun Sun, Wei Liu, and Lin Zhou. Fabrication of Cu(In,Ga)Se₂ thin films solar cell by selenization process with Se vapor. *Sol. Energy*, 80:191, 2006. doi: 10.1016/j.solener.2005.07.011.
- [140] V. Alberts. Comparison of material properties of CuInSe₂ films produced by reaction of metallic alloys to H₂Se/Ar and elemental Se vapour. *Jpn. J. Appl. Phys.*, 41(Part 1, No. 2A):518–523, 2002. doi: 10.1143/JJAP.41.518.
- [141] M. Sugiyama, F.B. Dejene, A. Kinoshita, M. Fukaya, Y. Maru, T. Nakagawa, H. Nakanishi, V. Alberts, and S. F. Chichibu. The use of diethylselenide as a less-hazardous source in CuInGaSe₂ photoabsorbing alloy formation by selenization of metal precursors premixed with Se. *J. Cryst. Growth*, 294:214–217, September 2006. doi: 10.1016/j.jcrysgro.2006.05.062.
- [142] V. Alberts, M. Chenene, O. Schenker, and E. Bucher. Preparation of CuInSe₂ thin films by rapid thermal processing of Se-containing precursors. *J. Mater. Sci. - Mater. Electron.*, 11:285, 2000. doi: 10.1023/A:1008921114215.
- [143] V. Probst, W. Stetter, W. Riedl, H. Vogt, M. Wendl, H. Calwer, S. Zweigart, K.-D. Ufert, B. Freienstein, H. Cerva, and F. H. Karg. Rapid CIS-process for high efficiency PV-modules: development towards large area processing. *Thin Solid Films*, 387(1-2):262, 2001. doi: 10.1016/S0040-6090(00)01800-9.
- [144] Jörg Palm, Volker Probst, and Franz H. Karg. Second generation CIS solar modules. *Sol. Energy*, 77(6):757–765, 2004. ISSN 0038-092X. doi: 10.1016/j.solener.2004.05.011.
- [145] Xuege Wang, Sheng S. Li, W. K. Kim, S. Yoon, V. Craciun, J. M. Howard, S. Easwaran, O. Manasreh, O. D. Crisalle, and T. J. Anderson. Investigation of rapid thermal annealing on Cu(In,Ga)Se₂ films and solar cells. *Sol. Energy Mater. Sol. Cells*, 90(17):2855, 2006. doi: 10.1016/j.solmat.2006.04.011.
- [146] A. Hölzing, R. Schurr, H. Yoo, R.A. Wibowo, R. Lechner, J. Palm, S. Jost, and R. Hock. Real-time investigations on the formation of Cu(In,Ga)(S,Se)₂ while annealing Cu–In–Ga precursors with different sulphur-selenium mixtures. *Thin Solid Films*, 535(0):112 – 117, 2013. ISSN 0040-6090. doi: 10.1016/j.tsf.2012.11.059.
- [147] Astrid Hölzing. *Untersuchung des Kristallisationsmechanismus von Cu(In,Ga)(S,Se)₂ Dünnschichtsolarzellenmaterialien durch in-situ Röntgenbeugung während der Reaktion von Metallschichten mit Schwefel und Selen*. PhD thesis, Universität Erlangen, 2013.
- [148] Yuri Goushi, Hideki Hakuma, Katsuya Tabuchi, Shunsuke Kijima, and Katsumi Kushiya. Fabrication of pentanary Cu(InGa)(SeS)₂ absorbers by selenization and sulfurization.

- Sol. Energy Mater. Sol. Cells*, 93(8):1318–1320, 2009. ISSN 0927-0248. doi: 10.1016/j.solmat.2009.02.004.
- [149] Udai P. Singh. Surface sulfurization studies of thin film Cu(InGa)Se₂ solar cells. *Vacuum*, 83(11):1344–1349, 2009. ISSN 0042-207X. doi: 10.1016/j.vacuum.2009.04.035.
- [150] Yoshinori Nagoya, Katsumi Kushiya, Muneyori Tachiyuki, and Osamu Yamase. Role of incorporated sulfur into the surface of Cu(InGa)Se₂ thin-film absorber. *Sol. Energy Mater. Sol. Cells*, 67(1-4):247–253, 2001. ISSN 0927-0248. doi: 10.1016/S0927-0248(00)00288-9.
- [151] Yoshiaki Tanaka, Norimasa Akema, Takahiro Morishita, Daisuke Okumura, and Katsumi Kushiya. Improvement of V_{oc} upward of 600 mV / cell with CIGS-based absorber prepared by selenization / sulfurization. *Proceedings 17th European Photovoltaic Solar Energy Conference*, pages 989–994, 2001.
- [152] Katsumi Kushiya. Progress in large-area Cu(InGa)Se₂-based thin-film modules with the efficiency of over 13 %. *Photovoltaic Energy Conversion, 2003. Proceedings of 3rd World Conference on*, 1:319–324, May 2003. doi: 10.1109/WCPEC.2003.1305285.
- [153] V. Probst, J. Palm, S. Visbeck, T. Niesen, R. Tölle, A. Lerchenberger, M. Wendl, H. Vogt, H. Calwer, W. Stetter, and F. Karg. New developments in Cu(In,Ga)(S,Se)₂ thin film modules formed by rapid thermal processing of stacked elemental layers. *Sol. Energy Mater. Sol. Cells*, 90(18-19):3115, 2006. doi: 10.1016/j.solmat.2006.06.031.
- [154] H. Sugimoto. High efficiency and large volume production of CIS-based modules. *Photovoltaic Specialist Conference (PVSC), 2014 IEEE 40th*, pages 2767–2770, June 2014. doi: 10.1109/PVSC.2014.6925503.
- [155] R. N. Bhattacharya. Solution growth and electrodeposited CuInSe₂ thin films. *J. Electrochem. Soc.*, 130(10):2040–2042, 1983. doi: 10.1149/1.2119516.
- [156] B. M. Basol, M. Pinarbasi, S. Aksu, J. Wang, Y. Matus, T. Johnson Y. Han, M. Narasimhan, and B. Metin. Electroplating based CIGS technology for roll-to-roll manufacturing. *Proceedings 23rd European Photovoltaic Solar Energy Conference*, 1: 2137, 2008. doi: 10.4229/23rdEUPVSEC2008-3DO.4.5.
- [157] R. N. Bhattacharya, J. F. Hiltner, W. Batchelor, M. A. Contreras, R. N. Noufi, and J. R. Sites. 15.4 % CuIn_{1-x}Ga_xSe₂-based photovoltaic cells from solution-based precursor films. *Thin Solid Films*, 361-362:396, 2000. doi: 10.1016/S0040-6090(99)00809-3.

- [158] Daniel Lincot. Electrodeposition of semiconductors. *Thin Solid Films*, 487:40, 2005. doi: 10.1016/j.tsf.2005.01.032.
- [159] D. Lincot, J. F. Guillemoles, S. Taunier, D. Guimard, J. Sicx-Kurdi, A. Chaumont, O. Roussel, O. Ramdani, C. Hubert, J. P. Fauvarque, N. Bodereau, L. Parissi, P. Panheleux, P. Fanouillere, N. Naghavi, P. P. Grand, M. Benfarah, P. Mogensen, and O. Kerrec. Chalcopyrite thin film solar cells by electrodeposition. *Sol. Energy*, 77(6):725, 2004. doi: 10.1016/j.solener.2004.05.024.
- [160] Francisco J. Garcia and Maharaj S. Tomar. A screen printed CdS/CuInSe₂ solar cell. *Jpn. J. Appl. Phys.*, 22-1:535, 1983. doi: 10.7567/JJAPS.22S1.535.
- [161] A. Vervaet, M. Burgelman, I. Clemminck, and M. Casteleyn. Screen printing of CIS films for CIS-CdS solar cells. *Proceedings 10th European Photovoltaic Solar Energy Conference*, 1:900, 1990.
- [162] Marc-Roland Kaelin. *Low-cost Cu(In,Ga)Se₂ absorbers from nanosized precursor materials for thin-film solar cells*. PhD thesis, Eidgenössische Technische Hochschule Zürich, 2005.
- [163] M. Kaelin, H. Zogg, A. N. Tiwari, O. Wilhelm, S. E. Pratsinis, T. Meyer, and A. Meyer. Electro sprayed and selenized Cu/In metal particle films. *Thin Solid Films*, 457:391, 2004. doi: 10.1016/S0040-6090(03)01033-2.
- [164] M. Kaelin, D. Rudmann, F. Kurdesau, T. Meyer, H. Zogg, and A. N. Tiwari. CIS and CIGS layers from selenized nanoparticle precursors. *Thin Solid Films*, 431-432:58, 2003. doi: 10.1016/S0040-6090(03)00194-9.
- [165] R. Kaigawa, T. Uesugi, T. Yoshida, S. Merdes, and R. Klenk. Instantaneous preparation of CuInSe₂ films from elemental In, Cu, Se particles precursor films in a non-vacuum process. *Thin Solid Films*, 517(7):2184–2186, 2009. ISSN 0040-6090. doi: 10.1016/j.tsf.2008.10.084.
- [166] T. Arita, N. Suyama, Y. Kita, S. Kitamura, T. Hibino, H. Takada, K. Omura, N. Ueno, and M. Murozono. CuInSe₂ films prepared by screen-printing and sintering method. *Conf. Rec. 20th IEEE Photovolt. Spec. Conf.*, 2:1650, 1988. doi: 10.1109/PVSC.1988.105992.
- [167] Matthew G. Panthani, Vahid Akhavan, Brian Goodfellow, Johanna P. Schmidtke, Lawrence Dunn, Ananth Dodabalapur, Paul F. Barbara, and Brian A. Korgel. Synthesis of CuInS₂, CuInSe₂, and Cu(In_xGa_{1-x})Se₂ (CIGS) nanocrystal inks for printable photovoltaics. *J. Am. Chem. Soc.*, 130(49):16770–16777, 2008. doi: 10.1021/ja805845q.

- [168] SeJin Ahn and KiHyun Kim and KyungHoon Yoon. Cu(In,Ga)Se₂ thin film solar cells from nanoparticle precursors. *Curr. Appl. Phys.*, 8(6):766–769, October 2008. doi: 10.1016/j.cap.2007.04.037.
- [169] Douglas L. Schulz, Calvin J. Curtis, Alan Cram, Jeffrey L. Alleman, Alice Mason, Richard J. Matson, John D. Perkins, and David S. Ginley. CIGS films via nanoparticle spray deposition: Attempts at densifying a porous precursor. *Conf. Rec. 26th IEEE Photovolt. Spec. Conf.*, pages 483–486, 1997. ISSN 0160-8371. doi: 10.1109/PVSC.1997.654133.
- [170] C. Suryanarayana, E. Ivanov, R. Noufi, M. A. Contreras, and J. J. Moore. Phase selection in a mechanically alloyed Cu-In-Ga-Se powder mixture. *J. Mater. Res.*, 14:377–383, February 1999. doi: 10.1557/JMR.1999.0055.
- [171] Takahiro Wada and Hiroki Kinoshita. Rapid exothermic synthesis of chalcopyrite-type CuInSe₂. *J. Phys. Chem. Solids*, 66(11):1987, 2005. doi: 10.1016/j.jpcs.2005.09.082.
- [172] Chung Ping Liu and Chuan Lung Chuang. Fabrication of CIGS nanoparticle-ink using ball milling technology for applied in CIGS thin films solar cell. *Powder Technology*, 229(0):78 – 83, 2012. ISSN 0032-5910. doi: 10.1016/j.powtec.2012.06.011.
- [173] Emre Yassitepe, William N. Shafarman, and S. Ismat Shah. Microstructure and phase evolution in single phase CuInSe₂ particles synthesized using elemental precursors. *J. Solid State Chem.*, 213:198 – 203, 2014. ISSN 0022-4596. doi: 10.1016/j.jssc.2014.02.023.
- [174] Hui Liu, Zhengguo Jin, Weidong Wang, Yueqiu Wang, and Haiyan Du. Well-dispersed, size-tunable chalcopyrite CuInSe₂ nanocrystals and its ink-coated thin films by polyhydric solution chemical process. *Mater. Lett.*, 81:173 – 176, 2012. ISSN 0167-577X. doi: 10.1016/j.matlet.2012.05.007.
- [175] Hui Liu, Zhengguo Jin, Jian Wang, Jianping Ao, and Guangmin Li. Well-dispersed CuInSe₂ nanoplates and nanoplates-ink-coated thin films for photovoltaic application by a triethylene glycol based solution process. *Mater. Lett.*, 94:1 – 4, 2013. ISSN 0167-577X. doi: 10.1016/j.matlet.2012.12.046.
- [176] Armin E. Zaghi, Marie Buffière, Guy Brammertz, Nick Lenaers, Marc Meuris, Jef Poortmans, and Jef Vleugels. Selenization of printed Cu–In–Se alloy nanopowder layers for fabrication of CuInSe₂ thin film solar cells. *Thin Solid Films*, 582:18–22, 2014. ISSN 0040-6090. doi: 10.1016/j.tsf.2014.10.038.

- [177] Armin E. Zaghi, Marie Buffière, Jaseok Koo, Guy Brammertz, Maria Batuk, Christophe Verbist, Joke Hadermann, Woo Kyoung Kim, Marc Meuris, Jef Poortmans, and Jef Vleugels. Effect of selenium content of CuInSe_x alloy nanopowder precursors on recrystallization of printed CuInSe₂ absorber layers during selenization heat treatment. *Thin Solid Films*, 582:11–17, 2014. ISSN 0040-6090. doi: 10.1016/j.tsf.2014.10.003.
- [178] Qijie Guo, Grayson M. Ford, Hugh W. Hillhouse, and Rakesh Agrawal. Sulfide nanocrystal inks for dense Cu(In_{1-x}Ga_x)(S_{1-y}Se_y)₂ absorber films and their photovoltaic performance. *Nano Lett.*, 9(8):3060–3065, August 2009. ISSN 1530-6984. doi: 10.1021/nl901538w.
- [179] P. Niyamakom, A. Quintilla, K. Kohler, M. Cemernjak, E. Ahlswede, and S. Roggan. Scalable synthesis of CuInS₂ nanocrystal inks for photovoltaic applications. *J. Mater. Chem. A*, 3:4470–4476, 2015. doi: 10.1039/C4TA05696E.
- [180] Christian Kind, Claus Feldmann, Aina Quintilla, and Erik Ahlswede. Citrate-capped Cu₁₁In₉ nanoparticles and its use for thin-film manufacturing of CIS solar cells. *Chem. Mater.*, 23(23):5269–5274, 2011. doi: 10.1021/cm2024668.
- [181] G. Norsworthy, C. R. Leidholm, A. Halani, V. K. Kapur, R. Roe, B. M. Basol, and R. Matson. CIS film growth by metallic ink coating and selenization. *Sol. Energy Mater. Sol. Cells*, 60(2):127, 2000. doi: 10.1016/S0927-0248(99)00075-6.
- [182] Bülent M. Basol. Low cost techniques for the preparation of Cu(In,Ga)(Se,S)₂ absorber layers. *Thin Solid Films*, 361-362:514, 2000. doi: 10.1016/S0040-6090(99)00823-8.
- [183] B. M. Basol, V. K. Kapur, G. Norsworthy, A. Halani, C. R. Leidholm, and R. Roe. Efficient CuInSe₂ solar cells fabricated by a novel ink coating approach. *Electrochemical and Solid-State Letters*, 1(6):252–254, 1998. doi: 10.1149/1.1390703.
- [184] Douglas L. Schulz, Calvin J. Curtis, Rebecca A. Flitton, Holm Wiesner, James Keane, Richard J. Matson, Kim M. Jones, Philip A. Parilla, Rommel Noufi, and David S. Ginley. Cu-In-Ga-Se nanoparticle colloids as spray deposition precursors for Cu(In,Ga)Se₂ solar cell materials. *J. Electron. Mater.*, 27(5):433, 1998. doi: 10.1007/s11664-998-0173-5.
- [185] Chris Eberspacher, Karen Pauls, and Jack Serra. Nonvacuum techniques for fabricating thin-film CIGS. *Conf. Rec. 28th IEEE Photovolt. Spec. Conf.*, 1:517, 2000. doi: 10.1109/PVSC.2000.915885.
- [186] Chris Eberspacher, Chris Fredric, Karen Pauls, and Jack Serra. Thin-film CIS alloy PV materials fabricated using non-vacuum, particles-based techniques. *Thin Solid Films*, 387:18, 2001. doi: 10.1016/S0040-6090(00)01729-6.

- [187] Vijay K. Kapur, Matthew Fisher, and Robin Roe. Nanoparticle oxides precursor inks for thin film copper indium gallium selenide (CIGS) solar cells. *Mater. Res. Soc. Symp. Proc.*, 668:H2.6, 2001. doi: 10.1557/PROC-668-H2.6.
- [188] Vijay K. Kapur, Ashish Bansal, Phucan Le, and Omar I. Asensio. Non-vacuum processing of $\text{CuIn}_{1-x}\text{Ga}_x\text{Se}_2$ solar cells on rigid and flexible substrates using nanoparticle precursor inks. *Thin Solid Films*, 431-432:53, 2003. doi: 10.1016/S0040-6090(03)00253-0.
- [189] Vijay Kapur, Ashish Bansal, Brian Gergen, and Phucan Le. Commercialization of ‘ink based’ CIGS solar cells / modules. *Proceedings of the International Photovoltaic Science and Engineering Conference*, 17:60–A11–05, 2007.
- [190] Seokhyun Yoon, Taehun Yoon, Kyoung-Soo Lee, Seokhee Yoon, Jeong Min Ha, and Seungbum Choe. Nanoparticle-based approach for the formation of CIS solar cells. *Sol. Energy Mater. Sol. Cells*, 93(6-7):783–788, 2009. ISSN 0927-0248. doi: 10.1016/j.solmat.2008.09.061.
- [191] Hailong Dong, Aina Quintilla, Marco Cemernjak, Radian Popescu, Dagmar Gerthsen, Erik Ahlswede, and Claus Feldmann. Colloidally stable selenium@ copper selenide core@shell nanoparticles as selenium source for manufacturing of copper–indium–selenide solar cells. *Journal of Colloid and Interface Science*, 415:103 – 110, 2014. ISSN 0021-9797. doi: 10.1016/j.jcis.2013.10.001.
- [192] Gregory Brown, Peter Stone, Jacob Woodruff, Ben Cardozo, and David Jackrel. Device characteristics of a 17.1 % efficient solar cell deposited by a non-vacuum printing method on flexible foil. *Conf. Rec. 38th IEEE Photovolt. Spec. Conf.*, 2012. doi: 10.1109/PVSC.2012.6318265.
- [193] Nanosolar. Ultra-low-cost solar electricity cells – an overview. Technical report, Nanosolar, 2009.
- [194] H. C. Hamaker. The London–van der Waals attraction between spherical particles. *Physica*, 4(10):1058–1072, 1937. ISSN 0031-8914. doi: 10.1016/S0031-8914(37)80203-7.
- [195] B. Derjaguin and L. Landau. Theory of the stability of strongly charged lyophobic sols and of the adhesion of strongly charged particles in solutions of electrolytes. *Progress in Surface Science*, 43(1-4):30–59, 1993. ISSN 0079-6816. doi: 10.1016/0079-6816(93)90013-L.
- [196] E. J. W. Verwey and J. Th. G. Overbeek. *Theory of the Stability of Lyophobic Colloids*. Dover Publications, Dover, July 1999. ISBN 0486409295.

- [197] Justin J. Nairn, Pamela J. Shapiro, Brendan Twamley, Tyler Pounds, Ray von Wandruszka, T. Rick Fletcher, Mark Williams, Chongmin Wang, and M. Grant Norton. Preparation of ultrafine chalcopyrite nanoparticles via the photochemical decomposition of molecular single-source precursors. *Nano Lett.*, 6:1218, 2006. doi: 10.1021/nl060661f.
- [198] Chris Eberspacher, Karen Pauls, and Jack Serra. Non-vacuum processing of CIGS solar cells. *Conf. Rec. 29th IEEE Photovolt. Spec. Conf.*, 1:684, May 2002. doi: 10.1109/PVSC.2002.1190657.
- [199] S. Merdes, L. Bechiri, Z. Hadjoub, M. Sano, and S. Ando. Influence of selenization temperature on the properties of CuInSe₂ thin films prepared by spin coating technique. *Phys. Stat. Sol. (c)*, 3(8):2535, 2006. doi: 10.1002/pssc.200669562.
- [200] Wakgari Hirpo, Sandeep Dhingra, Anthony C. Sutorik, and Mercuri G. Kanatzidis. Synthesis of mixed copper-indium chalcogenolates. Single-source precursors for the photovoltaic materials CuInQ₂, (Q = S, Se). *J. Am. Chem. Soc.*, 115(4):1597, 1993. doi: 10.1021/ja00057a067.
- [201] Jerry D. HARRIX, Kulbinder K. Banger, David A. Scheiman, Mark A. Smith, Michael H.-C. Jin, and Aloysius F. Hepp. Characterization of CuInS₂ films prepared by atmospheric pressure spray chemical vapor deposition. *Mater. Sci. Eng., B*, 98:150, 2003. doi: 10.1016/S0921-5107(03)00041-2.
- [202] David B. Mitzi, Min Yuan, Wei Liu, Andrew J. Kellock, S. Jay Chey, Alex Schrott, and Vaughn Deline. Solution processing of CIGS absorber layers using a hydrazine-based approach. *Conf. Rec. 33rd IEEE Photovolt. Spec. Conf.*, 1:1–5, May 2008. ISSN 0160-8371. doi: 10.1109/PVSC.2008.4922730.
- [203] David B. Mitzi, Min Yuan, Wei Liu, Andrew J. Kellock, S. Jay Chey, Vaughn Deline, and Alex G. Schrott. A high-efficiency solution-deposited thin-film photovoltaic device. *Adv. Mater.*, 20(19):3657–3662, 2008. doi: 10.1002/adma.200800555.
- [204] David B. Mitzi, Min Yuan, Wei Liu, Andrew J. Kellock, S. Jay Chey, Lynne Gignac, and Alex G. Schrott. Hydrazine-based deposition route for device-quality CIGS films. *Thin Solid Films*, 517(7):2158–2162, 2009. ISSN 0040-6090. doi: 10.1016/j.tsf.2008.10.079.
- [205] Teodor K. Todorov, Oki Gunawan, Tayfun Gokmen, and David B. Mitzi. Solution-processed Cu(In,Ga)(S,Se)₂ absorber yielding a 15.2 % efficient solar cell. *Prog. Photovoltaics Res. Appl.*, 21(1):82–87, 2013. ISSN 1099-159X. doi: 10.1002/pip.1253.

- [206] Calvin J. Curtis, Alexander Miedaner, Marinus Franciscus Antonius Van Hest, and David S. Ginley. Precursors for formation of copper selenide, indium selenide, copper indium diselenide, and/or copper indium gallium diselenide films, 2009. URL <http://www.freepatentsonline.com/y2009/0280624.html>.
- [207] SeJin Ahn, ChaeWoong Kim, JaeHo Yun, MinSik Kim, JeongChul Lee, and KyungHoon Yoon. Effects of selenization conditions on the properties of CIS layer prepared by non-vacuum coating of low cost precursor solution. *Proceedings 22nd European Photovoltaic Solar Energy Conference*, 1:2320, 2007.
- [208] Jong Won Park, Young Woo Choi, Eunjoo Lee, Oh Shim Joo, Sungho Yoon, and Byoung Koun Min. Synthesis of CIGS absorber layers via paste coating. *J. Cryst. Growth*, 311:2621–2625, 2009. doi: 10.1016/j.jcrysgro.2009.02.038.
- [209] Ulrich Berner and Markus Widenmeyer. Solution-based processing of Cu(In,Ga)Se₂ absorber layers for 11 % efficiency solar cells via a metallic intermediate. *Prog. Photovoltaics Res. Appl.*, 23(10):1260–1266, 2014. ISSN 1099-159X. doi: 10.1002/pip.2546.
- [210] Sho Shirakata, Tomonori Murakami, Tetsuya Kariya, and Shigehiro Isomura. Preparation of CuInSe₂ thin films by chemical spray pyrolysis. *Jpn. J. Appl. Phys.*, 35:191, 1996. doi: 10.1143/JJAP.35.191.
- [211] Sho Shirakata, Yoshiaki Kannaka, Harufumi Hasegawa, Tetsuya Kariya, and Shigehiro Isomura. Properties of Cu(In,Ga)Se₂ thin films prepared by chemical spray pyrolysis. *Jpn. J. Appl. Phys.*, 38:4997, 1999. doi: 10.1143/JJAP.38.4997.
- [212] K. T. Ramakrishna Reddy and R. W. Miles. Surface characterization of sprayed CuGa_xIn_{1-x}Se₂ layers. *J. Mater. Sci. - Mater. Electron.*, 14(9):529, 2003. doi: 10.1023/A:1024581232009.
- [213] S. Duchemin, J. Bougnot, A. El Ghzizal, and K. Belghit. Studies on the improvement of sprayed CdS–CuInSe₂ solar cells. *Proceedings 9th European Photovoltaic Solar Energy Conference*, 1:476–479, 1989.
- [214] Christian Camus. *Spray ILGAR Growth and Raman Spectroscopy of CuInS₂ Thin Films*. PhD thesis, Freie Universität Berlin, 2008.
- [215] Christian-Herbert Fischer, Hans-Jürgen Muffler, Marcus Bär, Timo Kropp, Antje Schönmann, Sebastian Fiechter, Ghassan Barbar, and Martha Christina Lux-Steiner. Spray-ion layer gas reaction (ILGAR) – a novel low-cost process for the deposition of chalcopyrite layers up to the micrometer range for photovoltaic applications. *J. Phys. Chem. B*, 107: 7516, 2003. doi: 10.1021/jp034911h.

- [216] C. Camus, D. Abou-Ras, N. A. Allsop, S. E. Gledhill, T. Koehler, J. Rappich, I. Lauer-mann, M. C. Lux-Steiner, and C.-H. Fischer. Formation of CuInS₂ carbon multilayers in the spray ILGAR process. *Phys. Stat. Sol. (a)*, 207(1):129–131, 2010. ISSN 1862-6319. doi: 10.1002/pssa.200925374.
- [217] V. Nadenau, U. Rau, A. Jasenek, and H. W. Schock. Electronic properties of CuGaSe₂-based heterojunction solar cells. Part I. Transport analysis. *J. Appl. Phys.*, 87:584, 2000. doi: 10.1063/1.371903.
- [218] A. Wittkopp, M. Haschke, and A. Eicke. Schichtanalytik mit der Röntgenfluoreszenz. *Metall*, 54:662–666, Nov 2000.
- [219] C. Cremer and T. Cremer. Considerations on a laser-scanning-microscope with high resolution and depth of field. *Microsc Acta*, 81(1):31–44, Sep. 1978. ISSN 0044-376X.
- [220] Jan Ungelenk. Kostengünstige Herstellungsmethoden von CIGS-Solarzellen mit partikelbasierten Drucktechniken. Master’s thesis, Universität Kassel, 2009.
- [221] M. Schlott, A. Kastner, M. Schultheis, C. Simons, C. Stegmann, and M.-L. Goyallon. Sputtering targets and thin film properties for thin film photovoltaic cells. *Proceedings 24th European Photovoltaic Solar Energy Conference*, 3DO.6.6:2473 – 2477, 2009. doi: 10.4229/24thEUPVSEC2009-3DO.6.6.
- [222] Veronika Haug, Ines Klugius, Theresa M. Friedlmeier, Aina Quintilla, and Erik Ahlswede. Cu(In,Ga)Se₂ thin-film solar cells based on a simple sputtered alloy precursor and a low-cost selenization step. *J. Photon. Energy*, 1:018002, 2011. doi: 10.1117/1.3659500.
- [223] Akinori Katsui and Tsunekazu Iwata. In-situ observation of CuInSe₂ formation process using high-temperature X-ray diffraction analysis. *Thin Solid Films*, 347(1-2):151, 1999. doi: 10.1016/S0040-6090(98)01747-7.
- [224] E. Rudigier, J. Djordjevic, C. von Klopmann, B. Barcones, A. Perez-Rodriguez, and R. Scheer. Real-time study of phase transformations in Cu-In chalcogenide thin films using in situ Raman spectroscopy and XRD. *J. Phys. Chem. Solids*, 66(11):1954, 2005. doi: 10.1016/j.jpcs.2005.09.096.
- [225] Patrick Berwian. *Experimentelle Untersuchung und Modellierung der Bildungskinetik von CuInSe₂-basierten Halbleiter-Dünnschichten für die Solarzellenherstellung*. PhD thesis, Friedrich-Alexander-Universität Erlangen-Nürnberg, 2005.

- [226] W. K. Kim, E. A. Payzant, S. Yoon, and T. J. Anderson. In situ investigation on selenization kinetics of Cu-In precursor using time-resolved, high temperature X-ray diffraction. *J. Cryst. Growth*, 294:231–235, September 2006. doi: 10.1016/j.jcrysgro.2006.05.066.
- [227] Ralf Steudel and Eva-Maria Strauß. Homocyclic selenium molecules and related cations. In H.J. Emeleus and A.G. Sharpe, editors, *Advances in Inorganic Chemistry*, volume 28 of *Advances in Inorganic Chemistry*, pages 135 – 166. Academic Press, 1984. doi: 10.1016/S0898-8838(08)60207-X.
- [228] D. A. Cammack, K. Shahzad, and T. Marshall. Low-temperature growth of ZnSe by molecular beam epitaxy using cracked selenium. *Appl. Phys. Lett.*, 56(9):845–847, 1990. doi: 10.1063/1.102680.
- [229] A.F. Holleman, E. Wiberg, and N. Wiberg. *Lehrbuch der anorganischen Chemie*. Gruyter, 1995. ISBN 9783110126419.
- [230] M. Ganchev, J. Kois, M. Kaelin, S. Bereznev, E. Tzvetkova, O. Volobujeva, N. Stratieva, and A. Tiwari. Preparation of Cu(In,Ga)Se₂ layers by selenization of electrodeposited Cu–In–Ga precursors. *Thin Solid Films*, 511-512:325, 2006. doi: 10.1016/j.tsf.2005.11.076.
- [231] F.B. Dejene. Material and device properties of Cu(In,Ga)Se₂ absorber films prepared by thermal reaction of InSe/Cu/GaSe alloys to elemental Se vapor. *Curr. Appl. Phys.*, 10(1): 36–40, 2010. ISSN 1567-1739. doi: 10.1016/j.cap.2009.04.008.
- [232] J. López-García and C. Guillén. CuIn_{1-x}Al_xSe₂ thin films obtained by selenization of evaporated metallic precursor layers. *Thin Solid Films*, 517(7):2240–2243, 2009. ISSN 0040-6090. doi: 10.1016/j.tsf.2008.10.095.
- [233] F. Karg, V. Probst, H. Harms, J. Rimmasch, W. Riedl, J. Kotschy, J. Holz, R. Treichler, O. Eibl, A. Mitwalsky, and A. Kiendl. Novel rapid-thermal-processing for CIS thin-film solar cells. *Conf. Rec. 23rd IEEE Photovolt. Spec. Conf.*, 1:441, 1993. doi: 10.1109/PVSC.1993.347141.
- [234] F. O. Adurodija, M. J. Carter, B. Ghosh, and R. Hill. Reaction mechanism and structural studies of CuInSe₂ fabricated by the stacked elemental layer (SEL) technique. *Proceedings 12th European Photovoltaic Solar Energy Conference*, 1:621, 1994.
- [235] H. Cheng, J. M. DePuydt, M. A. Haase, and J. E. Potts. Molecular-beam epitaxy growth of ZnSe using a cracked selenium source. *J. Vac. Sci. Technol., B*, 8(2):181–186, March 1990. doi: 10.1116/1.584850.

- [236] Masahiro Kawamura, Toshiyuki Fujita, Akira Yamada, and Makoto Konagai. Cu(In,Ga)Se₂ thin-film solar cells grown with cracked selenium. *J. Cryst. Growth*, 311(3):753–756, 2009. ISSN 0022-0248. doi: 10.1016/j.jcrysgro.2008.09.091.
- [237] Shogo Ishizuka, Hajime Shibata, Akimasa Yamada, Paul Fons, Keiichiro Sakurai, Koji Matsubara, and Shigeru Niki. Growth of polycrystalline Cu(In,Ga)Se₂ thin films using a radio frequency-cracked Se-radical beam source and application for photovoltaic devices. *Appl. Phys. Lett.*, 91:041902–3, July 2007. doi: 10.1063/1.2766669.
- [238] Shogo Ishizuka, Akimasa Yamada, Hajime Shibata, Paul Fons, Keiichiro Sakurai, Koji Matsubara, and Shigeru Niki. Large grain Cu(In,Ga)Se₂ thin film growth using a Se-radical beam source. *Sol. Energy Mater. Sol. Cells*, 93(6-7):792–796, 2009. ISSN 0927-0248. doi: 10.1016/j.solmat.2008.09.043.
- [239] S. Kosaraju, I. Repins, and C. A. Wolden. Development of plasma-assisted processing for selenization and sulfurization of absorber layers. *Mater. Res. Soc. Symp. Proc.*, 763: B8.19, 2003. doi: 10.1557/PROC-763-B8.19.
- [240] V. Alberts. A comparison of the material and device properties of homogeneous and compositional-graded Cu(In,Ga)(Se,S)₂ chalcopyrite thin films. *Semicond. Sci. Technol.*, 22(6):585–592, 2007. doi: 10.1088/0268-1242/22/6/001.
- [241] V. M. Fthenakis and P. D. Moskowitz. Photovoltaics: environmental, health and safety issues and perspectives. *Prog. Photovoltaics Res. Appl.*, 8(1):27–38, 2000. ISSN 1099-159X. doi: 10.1002/(SICI)1099-159X(200001/02)8:1<27::AID-PIP296>3.0.CO;2-8.
- [242] M. Sugiyama, A. Umezawa, T. Yasuniwa, A. Miyama, H. Nakanishi, and S. F. Chichibu. Growth of single-phase Cu(In,Al)Se₂ photoabsorbing films by selenization using diethylselenide. *Thin Solid Films*, 517(7):2175–2177, 2009. ISSN 0040-6090. doi: 10.1016/j.tsf.2008.10.083.
- [243] Shashank Mishra, Erwann Jeanneau, and Stéphane Daniele. Dimethyl selenide complexes of copper, gallium and indium halides as potential precursors for selenium-containing chalcopyrite semiconducting materials. *Polyhedron*, 29(1):500 – 506, 2010. ISSN 0277-5387. doi: 10.1016/j.poly.2009.06.047.
- [244] Masahiro Tahashi, Kenji Iinuma, Hideo Goto, Kenji Yoshino, Makoto Takahashi, and Toshiyuki Ido. Growth of Cu(In,Ga)Se₂ films selenized using dimethylselenium. *Materials Transactions*, 53(6):1169, 2012. doi: 10.2320/matertrans.M2011355.
- [245] Sheng-Yu Hsiao, Pei-Ching Yang, Ho-Ching Ni, Kuo-Yi Yen, Chien-Hua Chiu, Pei-Shin Lin, Hung-Jung Chen, Cheng-Han Wu, Shih-Chang Liang, Guo-Yu Ni, Far-Wen Jih,

- Cheng-Der Chiang, and Jyh-Rong Gong. Characteristics of Cu(In,Ga)Se₂ films prepared by atmospheric pressure selenization of Cu-In-Ga precursors using di-tert-butylselenide as Se source. *Journal of The Electrochemical Society*, 159(4):H378–H383, 2012. doi: 10.1149/2.021204jes.
- [246] Mehmet Eray Erkan, Shenbin D. Wu, Chun-Young Lee, Min-Young Kim, Donggun Lim, Kyungkon Kim, and Michael H.-C. Jin. Chalcopyrite thin films and solar cells prepared by using selenoamide as a selenium source. *Thin Solid Films*, 574(0):207 – 215, 2015. ISSN 0040-6090. doi: 10.1016/j.tsf.2014.12.017.
- [247] T. Yamamoto, M. Nakamura, J. Ishizuki, T. Deguchi, S. Ando, H. Nakanishi, and S. Chichibu. Use of diethylselenide as a less-hazardous source for preparation of CuInSe₂ thin films by selenization of metal precursors. *Journal of Physics and Chemistry of Solids*, 64(9–10):1855 – 1858, 2003. ISSN 0022-3697. doi: 10.1016/S0022-3697(03)00146-X.
- [248] A.H. Jahagirdar, N.G. Dhere, S.S. Kulkarni, A.A. Kadam, J.S. Shirolkar, H. Moutinho, and B. To. Preparation and properties of CIGS and CIGSS thin films using DESe as a selenium source and H₂S as sulfur source. *Photovoltaic Specialists Conference, 2005. Conference Record of the Thirty-first IEEE*, 1:414 – 417, 2005. ISSN 0160-8371. doi: 10.1109/PVSC.2005.1488157.
- [249] Tomoaki Sato, Yoshifumi Kawasaki, Mutsumi Sugiyama, and Shigefusa F. Chichibu. Morphological and structural changes in Cu(In,Ga)Se₂ thin films by selenization using diethylselenide. *Jpn. J. Appl. Phys.*, 50(5):05FB05, 2011. doi: 10.1143/JJAP.50.05FB05.
- [250] P.J. Rostan, J. Mattheis, G. Bilger, U. Rau, and J.H. Werner. Formation of transparent and ohmic ZnO:Al/MoSe₂ contacts for bifacial Cu(In,Ga)Se₂ solar cells and tandem structures. *Thin Solid Films*, 480–481(0):67 – 70, 2005. ISSN 0040-6090. doi: 10.1016/j.tsf.2004.11.001.
- [251] K. D. Bronsema, J. L. De Boer, and F. Jellinek. On the structure of molybdenum diselenide and disulfide. *Zeitschrift für anorganische und allgemeine Chemie*, 540(9-10): 15–17, 1986. ISSN 1521-3749. doi: 10.1002/zaac.19865400904.
- [252] F. Klabunde, M. Löhmann, J. Bläsing, and T. Drüsedau. The influence of argon pressure on the structure of sputtered molybdenum: From porous amorphous to a new type of highly textured film. *J. Appl. Phys.*, 80(11):6266–6273, 1996. doi: 10.1063/1.363702.
- [253] R. Menner, E. Groß, A. Eicke, H. Dittrich, J. Springer, B. Dimmler, U. Rühle, M. Kaiser, T. Friedlmeier, and H. W. Schock. Investigations on sputter-deposited molybdenum back

- contacts for Cu(In, Ga)Se₂ solar cells. *Proceedings 13th European Photovoltaic Solar Energy Conference*, 1:2067–2071, 1995.
- [254] Ju-heon Yoon, Sunghun Cho, Tae-yeon Seong, and Jeung-hyun Jeong. Optical diagnosis of the microstructure of Mo back contact for CIGS solar cell. *ECS Meeting Abstracts*, 902(9):763–763, 2009.
- [255] C. T. Wu. Intrinsic stress of magnetron-sputtered niobium films. *Thin Solid Films*, 64(1): 103–110, 1979. ISSN 0040-6090. doi: 10.1016/0040-6090(79)90549-2.
- [256] H. Windischmann. An intrinsic stress scaling law for polycrystalline thin films prepared by ion beam sputtering. *J. Appl. Phys.*, 62(5):1800–1807, 1987. doi: 10.1063/1.339560.
- [257] John A. Thornton and David W. Hoffman. Internal stresses in titanium, nickel, molybdenum, and tantalum films deposited by cylindrical magnetron sputtering. *J. Vac. Sci. Technol.*, 14(1):164–168, 1977. doi: 10.1116/1.569113.
- [258] Y. G. Shen. Effect of deposition conditions on mechanical stresses and microstructure of sputter-deposited molybdenum and reactively sputter-deposited molybdenum nitride films. *Mater. Sci. Eng., A*, 359(1-2):158–167, 2003. ISSN 0921-5093. doi: 10.1016/S0921-5093(03)00336-8.
- [259] Tilo P. Drüsedau, F. Klabunde, P. Veit, and Th. Hempel. Investigations on microstructure, surface topography, and growth process of sputtered molybdenum showing texture turnover. *Phys. Stat. Sol. (a)*, 161(1):167–184, 1997. doi: 10.1002/1521-396X(199705)161:1<167::AID-PSSA167>3.0.CO;2-N.
- [260] A. F. Jankowski and L. R. Schrawyer. Reactive sputtering of molybdenum. *Thin Solid Films*, 193-194(Part 1):61–71, 1990. ISSN 0040-6090. doi: 10.1016/S0040-6090(05)80012-4.
- [261] Veronika Haug, Aina Quintilla, and Erik Ahlswede. CIGS solar cells with very thin absorber layers. *Conf. Rec. 34th IEEE Photovolt. Spec. Conf.*, pages 000763–000765, 2009. doi: 10.1109/PVSC.2009.5411171.
- [262] W. N. Shafarman, R. W. Birkmire, S. Marsillac, M. Marudachalam, N. Orbey, and T. W. F. Russell. Effect of reduced deposition temperature, time, and thickness on Cu(InGa)Se₂ films and devices. *Conf. Rec. 26th IEEE Photovolt. Spec. Conf.*, 1:331–334, Sep-3 Oct 1997. ISSN 0160-8371. doi: 10.1109/PVSC.1997.654095.

- [263] Takayuki Negami, Shiro Nishiwaki, Yasuhiro Hashimoto, Naoki Kohara, and Takahiro Wada. Effect of absorber thickness on performance of Cu(In,Ga)Se₂ solar cells. *Photovoltaic Energy Conversion, Conference Record of the 1998 IEEE 2nd World Conference on*, 1:1181–1184, 1998.
- [264] Olle Lundberg, Marika Bodegård, Jonas Malmström, and Lars Stolt. Influence of the Cu(In,Ga)Se₂ thickness and Ga grading on solar cell performance. *Prog. Photovoltaics Res. Appl.*, 11(2):77, 2003. doi: 10.1002/pip.462.
- [265] Markus Gloeckler and James R. Sites. Potential of submicrometer thickness Cu(In,Ga)Se₂ solar cells. *J. Appl. Phys.*, 98(10):103703, 2005. doi: 10.1063/1.2128054.
- [266] J. Pettersson, T. Torndahl, C. Platzer-Bjorkman, A. Hultqvist, and M. Edoff. The influence of absorber thickness on Cu(In,Ga)Se₂ solar cells with different buffer layers. *Photovoltaics, IEEE Journal of*, 3(4):1376–1382, Oct 2013. ISSN 2156-3381. doi: 10.1109/JPHOTOV.2013.2276030.
- [267] Veronika Haug, Aina Quintilla, Ines Klugius, and Erik Ahlswede. Influence of an additional carbon layer at the back contact-absorber interface in Cu(In,Ga)Se₂ thin film solar cells. *Thin Solid Films*, 519(21):7464 – 7467, 2011. doi: 10.1016/j.tsf.2010.12.140.
- [268] L. Kronik, L. Burstein, M. Leibovitch, Yoram Shapira, D. Gal, E. Moons, J. Beier, G. Hodes, David Cahen, D. Hariskos, R. Klenk, and H.W. Schock. Band diagram of the polycrystalline CdS/Cu(In,Ga)Se₂ heterojunction. *Appl. Phys. Lett.*, 67(10):1405–1407, 1995. doi: 10.1063/1.114508.
- [269] M. Morkel, L. Weinhardt, B. Lohmüller, C. Heske, E. Umbach, W. Riedl, S. Zweigart, and F. Karg. Flat conduction-band alignment at the CdS/CuInSe₂ thin-film solar-cell heterojunction. *Appl. Phys. Lett.*, 79(27):4482–4484, 2001. doi: 10.1063/1.1428408.
- [270] S. Sharbati and J.R. Sites. Impact of the band offset for n-Zn(O,S)/p-Cu(In,Ga)Se₂ solar cells. *Photovoltaics, IEEE Journal of*, 4(2):697–702, March 2014. ISSN 2156-3381. doi: 10.1109/JPHOTOV.2014.2298093.
- [271] R. Scheer. Towards an electronic model for CuInGaSe₂ solar cells. *Thin Solid Films*, 519(21):7472 – 7475, 2011. ISSN 0040-6090. doi: 10.1016/j.tsf.2011.01.092.
- [272] S. Nishiwaki, N. Kohara, T. Negami, M. Nishitani, and T. Wada. Characterization of Cu(In,Ga)Se₂/Mo interface in CIGS solar cells. *Mater. Res. Soc. Symp. Proc.*, 485:139, 1998. doi: 10.1557/PROC-485-139.

- [273] Naoki Kohara, Shiro Nishiwaki, Yasuhiro Hashimoto, Takayuki Negami, and Takahiro Wada. Electrical properties of the Cu(In,Ga)Se₂/MoSe₂/Mo structure. *Sol. Energy Mater. Sol. Cells*, 67(1-4):209–215, 2001. ISSN 0927-0248. doi: 10.1016/S0927-0248(00)00283-X.
- [274] D. Abou-Ras, G. Kostorz, D. Bremaud, M. Kälin, F. V. Kurdesau, A.N. Tiwari, and M. Döbeli. Formation and characterisation of MoSe₂ for Cu(In,Ga)Se₂ based solar cells. *Thin Solid Films*, 480-481:433–438, 2005. ISSN 0040-6090. doi: 10.1016/j.tsf.2004.11.098.
- [275] Naima Touafek and R. Mahamadi. Back surface recombination effect on the ultra-thin CIGS solar cells by SCAPS. *International Journal of Renewable Energy Research*, 4(4): 958–964, 2014.
- [276] Bart Vermang, Viktor Fjällström, Jonas Pettersson, Pedro Salomé, and Marika Edoff. Development of rear surface passivated Cu(In,Ga)Se₂ thin film solar cells with nano-sized local rear point contacts. *Sol. Energy Mater. Sol. Cells*, 117:505 – 511, 2013. ISSN 0927-0248. doi: 10.1016/j.solmat.2013.07.025.
- [277] Bart Vermang, Jörn Timo Wätjen, Viktor Fjällström, Fredrik Rostvall, Marika Edoff, Ratan Kotipalli, Frederic Henry, and Denis Flandre. Employing Si solar cell technology to increase efficiency of ultra-thin Cu(In,Ga)Se₂ solar cells. *Prog. Photovoltaics Res. Appl.*, 22(10):1023–1029, 2014. ISSN 1099-159X. doi: 10.1002/pip.2527.
- [278] M. Burgelman, P. Nollet, and S. Degraeve. Modelling polycrystalline semiconductor solar cells. *Thin Solid Films*, 361-362:527–532, 2000. ISSN 0040-6090. doi: 10.1016/S0040-6090(99)00825-1.
- [279] C Frisk, C Platzer-Björkman, J Olsson, P Szaniawski, J T Wätjen, V Fjällström, P Salomé, and M Edoff. Optimizing Ga-profiles for highly efficient Cu(In,Ga)Se₂ thin film solar cells in simple and complex defect models. *J. Phys. D: Appl. Phys.*, 47(48):485104, 2014. doi: 10.1088/0022-3727/47/48/485104.

Publications

Journal Papers

- Christian Karnutsch, Christian Gärtner, Veronika Haug, Uli Lemmer, Tony Farrell, Benjamin S. Nehls, Uli Scherf, Jing Wang, Thomas Weimann, George Heliotis, Christof Pflumm, John C. deMello, and Donal D. C. Bradley. Low threshold blue conjugated polymer lasers with first- and second-order distributed feedback. *Appl. Phys. Lett.*, 89(20):201108, 2006. doi: 10.1063/1.2390644
- Christian Karnutsch, Christof Pflumm, George Heliotis, John C. deMello, Donal D. C. Bradley, Jing Wang, Thomas Weimann, Veronika Haug, Christian Gärtner, and Uli Lemmer. Improved organic semiconductor lasers based on a mixed-order distributed feedback resonator design. *Appl. Phys. Lett.*, 90(13):131104, 2007. doi: 10.1063/1.2717518
- Jan Ungelenk, Veronika Haug, Aina Quintilla, and Erik Ahlswede. CuInSe₂ low-cost thin-film solar cells made from commercial elemental metallic nanoparticles. *Phys. Stat. Sol. (RRL)*, 4(3-4):58–60, 2010. doi: 10.1002/pssr.200903418
- Veronika Haug, Aina Quintilla, Ines Klugius, and Erik Ahlswede. Influence of an additional carbon layer at the back contact-absorber interface in Cu(In,Ga)Se₂ thin film solar cells. *Thin Solid Films*, 519(21):7464 – 7467, 2011. doi: 10.1016/j.tsf.2010.12.140
- Veronika Haug, Ines Klugius, Theresa M. Friedlmeier, Aina Quintilla, and Erik Ahlswede. Cu(In,Ga)Se₂ thin-film solar cells based on a simple sputtered alloy precursor and a low-cost selenization step. *J. Photon. Energy*, 1:018002, 2011. doi: 10.1117/1.3659500
- Björn J. Mueller, Christian Zimmermann, Veronika Haug, Frank Hergert, Thomas Koehler, Siegmund Zweigart, and Ulrich Herr. Influence of different sulfur to selenium ratios on the structural and electronic properties of Cu(In,Ga)(S,Se)₂ thin films and solar cells formed by the stacked elemental layer process. *J. Appl. Phys.*, 116(17):174503, 2014. doi: 10.1063/1.4900991

- Björn J. Mueller, Markus Mock, Veronika Haug, Frank Hergert, Thomas Koehler, Siegmund Zweigart, and Ulrich Herr. Ex- and in-situ investigations of sulfur diffusion into Cu(In,Ga)Se₂ thin films. *Thin Solid Films*, 582:284 – 289, 2015. doi: 10.1016/j.tsf.2014.10.044
- Björn J. Mueller, Arthur Fotler, Veronika Haug, Frank Hergert, Siegmund Zweigart, and Ulrich Herr. Influence of Mo–N as diffusion barrier in Mo back contacts for Cu(In,Ga)Se₂ solar cells. *Thin Solid Films*, 612:186 – 193, 2016. doi: 10.1016/j.tsf.2016.06.009
- Björn J. Mueller, Borirak Opananont, Veronika Haug, Frank Hergert, Siegmund Zweigart, and Ulrich Herr. Influence of selenium amount on the structural and electronic properties of Cu(In,Ga)Se₂ thin films and solar cells formed by the stacked elemental layer process. *Thin Solid Films*, 608:62 – 70, 2016. doi: 10.1016/j.tsf.2016.04.015
- Björn J. Mueller, Thomas Demes, Patrick C. Lill, Veronika Haug, Frank Hergert, Siegmund Zweigart, and Ulrich Herr. Temperature dependency of the Ga/In distribution in Cu(In,Ga)Se₂ absorbers in high temperature processes. *J. Cryst. Growth*, 442:31 – 40, 2016. doi: 10.1016/j.jcrysgro.2016.02.030

Conference Contributions

Oral Presentations

- Christian Karnutsch, Veronika Haug, Christian Gaertner, Uli Lemmer, Tony Farrell, Benjamin S. Nehls, Uli Scherf, Jing Wang, Thomas Weimann, George Heliotis, Christof Pflumm, John deMello, and Donal D. Bradley. Low threshold blue conjugated polymer DFB lasers. In *Conference on Lasers and Electro-Optics/Quantum Electronics and Laser Science Conference and Photonic Applications Systems Technologies. (CLEO/QELS)*, 2006
- Veronika Haug, Aina Quintilla, Ines Klugius, and Erik Ahlswede. Influence of an additional carbon layer at the back contact-absorber interface in Cu(In,Ga)Se₂ thin film solar cells. In *EMRS Spring Meeting 2010 Symposium M: Thin Film Chalcogenide Photovoltaic Materials, Strasbourg, France, May 2010*
- Zhenhao Zhang, Veronika Haug, Ines Klugius, Manuel Reinhard, Aina Quintilla, Theresa Magorian Friedlmeier, Erik Ahlswede, Alexander Colsmann, Michael Powalla, and Uli Lemmer. Impact of the reduction of the selenization duration in a sequential process on the properties of Cu(In,Ga)Se₂ thin-film solar cells. In *EMRS Bilateral Energy Conference, Nice, France, May 2011*

- Björn J. Mueller, Borirak Opanont, Veronika Haug, Siegmund Zweigart, and Ulrich Herr. Influence of selenium and sulfur amount on the structural and electronic properties of Cu(In,Ga)(Se,S)₂ thin films and solar cells. In *E-MRS Spring Meeting 2013, Strasbourg, France*, May 2013

Poster Presentations

- Christian Gärtner, Christof Pflumm, Christian Karnutsch, Veronika Haug, and Uli Lemmer. Numerical study of annihilation processes in electrically pumped organic semiconductor laser diodes. In *SPIE, Organic Light Emitting Materials and Devices X, San Diego, CA, USA*, 2006
- Christian Karnutsch, Veronika Haug, Christian Gärtner, Uli Lemmer, Christof Pflumm, George Heliotis, John C. deMello, Donal D.C. Bradley, Jing Wang, and Thomas Weimann. Low-threshold blue vertically emitting polyfluorene DFB lasers employing first-order feedback. In *SPIE, Organic Light Emitting Materials and Devices X, San Diego, CA, USA*, 2006
- Veronika Haug, Aina Quintilla, and Erik Ahlswede. CIGS solar cells with very thin absorber layers. In *34th IEEE Photovoltaic Specialists Conference, Philadelphia, PA, USA*, June 2009
- Aina Quintilla, Jan Ungelenk, Veronika Haug, and Erik Ahlswede. Non-vacuum fabrication of CuInSe₂ (CIS) thin-film solar cells from nanoparticles. In *EUROMAT 2009, European Congress and Exhibition on Advanced Materials and Processes, Glasgow, UK*, September 2009
- Ines Klugius, Aina Quintilla, Veronika Haug, and Erik Ahlswede. High efficiencies of CIGS solar cells with non-vacuum selenisation of precursors sputtered from a single ternary target using elemental selenium. In *EMRS Spring Meeting 2010 Symposium M: Thin Film Chalcogenide Photovoltaic Materials, Strasbourg, France*, May 2010
- Aina Quintilla, Ines Klugius, Veronika Haug, and Erik Ahlswede. Comparing stabilizers for solution processed CuInSe₂ thin-film solar cells with nanoparticle-based precursors. In *EMRS Spring Meeting 2010 Symposium M: Thin Film Chalcogenide Photovoltaic Materials, Strasbourg, France*, May 2010
- Ines Klugius, Cathrin Gemmel, Aina Quintilla, Veronika Haug, and Erik Ahlswede. CIS low-cost thin-film solar cells made from elemental metallic nanoparticles: Comparison of selenization parameters. In *35th IEEE Photovoltaic Specialists Conference, Honolulu, HI, USA*, June 2010

Proceedings

- Christian Karnutsch, Veronika Haug, Christian Gaertner, Uli Lemmer, Tony Farrell, Benjamin S. Nehls, Uli Scherf, Jing Wang, Thomas Weimann, George Heliotis, Christof Pflumm, John deMello, and Donal D. Bradley. Low threshold blue conjugated polymer DFB lasers. In *Conference on Lasers and Electro-Optics/Quantum Electronics and Laser Science Conference and Photonic Applications Systems Technologies*, page CFJ3. Optical Society of America, 2006. doi: 10.1109/CLEO.2006.4627622
- Christian Gärtner, Christof Pflumm, Christian Karnutsch, Veronika Haug, and Uli Lemmer. Numerical study of annihilation processes in electrically pumped organic semiconductor laser diodes. In *Proc. SPIE, Organic Light Emitting Materials and Devices X*, volume 6333, pages 63331J–63331J–12, 2006. doi: 10.1117/12.680370
- Veronika Haug, Aina Quintilla, and Erik Ahlswede. CIGS solar cells with very thin absorber layers. *Conf. Rec. 34th IEEE Photovolt. Spec. Conf.*, pages 000763–000765, 2009. doi: 10.1109/PVSC.2009.5411171
- Ines Klugius, Cathrin Gemmel, Aina Quintilla, Veronika Haug, and Erik Ahlswede. CIS low-cost thin-film solar cells made from elemental metallic nanoparticles: Comparison of selenization parameters. *Conf. Rec. 35th IEEE Photovolt. Spec. Conf.*, pages 003446–003449, June 2010. doi: 10.1109/PVSC.2010.5614648

Acknowledgements

As for all PhD theses it is also true for this one here — it was only possible thanks to the support of many people. I am sure I miss some of them nonetheless I want to take the opportunity to express my gratitude here to the following:

First and foremost I thank Prof. Dr. Heinz Kalt for accepting me as an (external) PhD student and being supervisor and the first examiner of this thesis. Thank you for all the support and your interest in my work.

Furthermore I want to thank Prof. Dr.-Ing Michael Powalla for offering me the opportunity to conduct the experimental work for this thesis at ZSW as one of the leading institutes in CIGS research in the world and for agreeing to being the second examiner for this thesis.

I want to express my sincere thanks to Dr. Erik Ahlswede who was my supervisor during my time at ZSW, always ready to discuss my research, questions, results... and who always was and still is a passionate researcher with countless ideas which enriched this thesis very much.

Many thanks are given to the numerous colleagues at ZSW preparing all other layers surrounding the absorber which are needed for a complete solar cell (Mo: Wolfram Hempel, Frank Nauerz, CdS: Daniela Müller, Tania Wohnhaas, Christine Böhmerle, Stefanie Spiering, Annika Schmoll, Dimitrios Hariskos ZnO: Andreas Nowitzky, Richard Menner), conducting measurements (SIMS — Axel Eicke) and helping with measurements (QE — Wolfram Witte, XRD — Stefanie Spiering, SEM — Daniela Müller and Theresa Magorian Friedlmeier).

For the preparation of the CIGS-layers in chapter 7 (evaporated absorbers) I want to thank the co-evaporation team, especially Wolfgang Dittus and Stefan Paetel. The idea to look more deeply into the topic of the additional carbon layer resulted for the most part from the curious questions of Philip Jackson who wondered several times why the efficiencies of these thin printed absorber layers were still so high — thank you for asking this question.

I am also thankful for the great atmosphere at the NEMA-group — special thanks to Ines and

Aina who were a support for the CIGS-topic avidly received and appreciated by me, Jonas who was a wonderful office mate (special thanks for all the chocolate during my last months at ZSW) and Tina who among other things shared uncountable lunch times with me.

Also all the other ZSW colleagues created a nice atmosphere and I am thankful for the support and that I could be a part of this great team.

Additionally I had the honour to be supervisor to various students — thank you Tanja Romahn, Jan Ungelenk and Christian Slupina for supporting our research and helping me to grow.

For proof reading I want to thank Julia Budde, Daniela Diessel and of course Erik Ahlswede — all the mistakes still in the text are my fault yet there would be much more had it not been for you.

To the Karlsruhe School of Optics and Photonics (KSOP) I am indebted for financial support (2 years of scholarship and 3 years of support for material costs and travel expenses), especially Prof. Dr. Uli Lemmer for suggesting me to apply for the scholarship before I started my thesis. I am also thankful for all the non-financial support of KSOP — the complementary courses, the contact to other PhD students, and last but not least the chance to gain insight into industrial research.

Now I am part of such an industrial research team and even though my colleagues at BOSCH corporate research did not directly contribute to this thesis I would like to thank them here: Thank you for all the motivation, your interest in my work, for encouraging me during the last years not only when I had doubts if I can handle a challenging research job, a family with small kids and a dissertation at the same time - you definitely contributed so much more to this thesis than you imagine!

The same is true for numerous friends and my (extended) family: I feel blessed to have you in my life — thanks for your support, your motivation, your understanding, your love!

My kids also did not contribute directly to this thesis — yet your patience especially in the last months was essential for finally finishing it and I am thankful beyond words for having you in my life – you reminded me of what is really important in life and taught me more than I could ever imagine, you make me proud of being your mum.

Last but definitely not least: Thank you Tobias — for your support, your love, your care for our growing family, your patience. Thanks for being there for me and believing in me. It means everything to me.

Curriculum Vitae

Personal Data

Name: Annegret Veronika Haug
Date of Birth: May 29th, 1981
City of Birth: Stuttgart

Education

2006: Diplom in Physics
2005-2006: “Diplomarbeit” (German equivalent of a Master thesis - 12 months)
topic: Ladungsträgerdynamik in hochangeregten organischen Leuchtdioden –
Dynamics of charge carriers in highly excited organic light emitting diodes
2004-2005: Master of Quantum Physics (60 ECTS) at KTH
2003-2004: “Hauptstudium Physik” at KIT
2001-2003: “Grundstudium Physik” at KIT
2000: Abitur ASG Crailsheim

Professional Experience

2012-today: research engineer Robert Bosch GmbH (Corporate Research and Advanced Engineering)
2007-2010: research assistant ZSW (Center for Solar Energy and Hydrogen Research)
2005-2006: student assistant LTI (Light Technology Institute)
lab work related to optoelectronic organic devices
2003-2004: student assistant IWE (Institute of Materials for Electrical and Electronic Engineering)
preparation and characterisation of raw materials, single layers and complete fuel cells
2000-2001: voluntary year of social service at a children’s home